



Technische Universität München

Department of Chemistry and Catalysis Research Center
Chair of Technical Electrochemistry

Design and Understanding of an All-Solid-State Battery Cell for Automotive Applications

Nathalie Riphaus

Vollständiger Abdruck der von der Fakultät für Chemie der
Technischen Universität München zur Erlangung des akademischen Grades eines

Doktors der Naturwissenschaften (Dr. rer. nat.)

genehmigten Dissertation.

Vorsitzender: Prof. Dr.-Ing. Kai-Olaf Hinrichsen

Prüfer der Dissertation: 1. Prof. Dr. Hubert A. Gasteiger
2. Prof. Dr. Tom Nilges

Diese Dissertation wurde am 26.04.2019 bei der Technischen Universität München eingereicht und durch die Fakultät für Chemie am 16.05.2019 angenommen.

Acknowledgement

First of all, I would like to thank Prof. Dr. Hubert A. Gasteiger for enabling me to become part of his group and conduct my PhD studies at the Chair of Technical Electrochemistry of the TUM. The great choice of topic allowed me to gain valuable experience under great conditions of work. I am particularly grateful for his passion on science that showed me what good scientific practice really means.

My gratitude also goes to the BMW AG for the financial support of my PhD studies. I would like to offer my special thanks to my supervisors Barbara Stiaszny, Saskia Schneider and Stefan J. Sedlmaier for their reliable support, for providing me with their knowledge, experience, time and patience. All the guidance, instructions and discussions made a substantial contribution to my PhD Thesis.

I would like to extend my sincerest gratitude to all team members at BMW for the for supporting me whenever required. My special thanks to Jan-Philipp Schmidt for his patience in explaining EIS to me, to Konstantinos Antonopoulos and Roland Jung for the support with the ProMotion program and their scientific advice, to Odysseas Paschos and Filippo Maglia for the coordination with TUM, to Frederik Morgenstern and Sandra Zugmann for the scientific discussions and especially to my students Gloria Hong, Philipp Strobl and Enzo Moretti for their contribution to my research.

I further wish to acknowledge all members of the Gasteiger working group for the welcoming and friendly atmosphere, for their support and guidance whenever needed. I am particularly grateful for the numerous scientific discussions with Hans Beyer, Johannes Landesfeind, Daniel Pritzl, Sophie Solchenbach and Morten Wetjen. Assistance on paperwork provided by Veronika Pichler is also greatly appreciated.

Last but not least I would like to like to express my very great appreciation to my family, my friends and particularly Patrick Schalamon for the endless support and understanding they gave me. They covered my back whenever needed and I would not have made it that far without them. Thanks to all of you!

Abstract

The increasing demand for sustainable transportation has accentuated the importance of batteries with high energy density. In order to reach the self-imposed target of $800 \text{ Wh}\cdot\text{l}^{-1}$ at cell level, BMW has to achieve significant improvement over current prismatic cells of battery electric vehicles (BEV). One important aspect to increase the energy density involves the implementation of advanced electrode materials. Therefore, the All-Solid-State Battery (ASSB) concept, which might enable the use of Li metal anodes and high voltage cathodes, represents a promising technology.

Despite the advantages associated with the solid electrolyte (SE) in the literature, several challenges including manufacturing methods as well as chemical and mechanical issues have to be overcome to pave the way for application of ASSBs in BEVs. Two major aspects, namely the degradation of the Li metal/SE interface and the scalable fabrication of SE layers and cathode sheets are addressed in this thesis. Different strategies to stabilize the interface between the lithium metal anode and the solid electrolyte layer were investigated. Among them, thin polymer interlayers proved to be beneficial in combination with oxide-based electrolytes. However, if sulfide-based materials are used, continuous decomposition was observed. The underlying chemical instability was examined and possible reasons were evaluated.

In the second part of this PhD thesis, feasible processing strategies in view of automotive applications are evaluated. Different polymers were tested regarding their suitability as binders for slurry-processed SE sheets. Their impacts on processing parameters as well as the properties of the resulting SE sheet, namely homogeneity, density, mechanical stability and ionic conductivity, were investigated. Subsequently, the impacts of several processing parameters on the homogeneity of composite cathode sheets were evaluated and several key parameters were identified.

Besides presenting a more comprehensive understanding of the ASSB concept, this PhD thesis provides general guidelines for the fabrication of two major ASSB components, thereby guiding towards a feasible cell design for automotive applications.

Kurzfassung

Die Relevanz von Batterien mit hoher Energiedichte hat durch das stetig wachsende Interesse an nachhaltigen Transportmitteln stark an Bedeutung gewonnen. Um das selbst gesetzte Ziel von $800 \text{ Wh}\cdot\text{l}^{-1}$ auf Zellebene zu erreichen, müssen BMW deutliche Verbesserungen gegenüber derzeitigen prismatischen Zellen in Elektroautos gelingen. Ein wesentlicher Aspekt zur Steigerung der Energiedichte ist der Einsatz besserer Elektrodenmaterialien. Daher stellt die Feststoffbatterie (ASSB), welche die Verwendung von Lithium-Metall-Anoden und energiereicheren Kathodenmaterialien ermöglichen könnte, eine vielversprechende Zelltechnologie dar.

Trotz der Vorteile, die mit der Verwendung eines Festelektrolyten (SE) gemäß der Literatur einhergehen, müssen noch diverse chemische, mechanische und produktionsbedingte Probleme gelöst werden, um den Einsatz von ASSBs in Elektroautos zu realisieren. Diese Doktorarbeit behandelt hierbei zwei wesentliche Aspekte: Die Instabilität der Grenzfläche zwischen Lithiummetall und Festelektrolyt sowie die skalierbare Herstellung von SE- und Kathoden-Schichten. Dabei wurden verschiedene Strategien zur Stabilisierung der Grenzfläche untersucht. Dünne Polymer-Zwischenschichten in Kombination mit oxydischen Elektrolyten stellten sich als gut geeignet heraus. Wenn jedoch sulfidische Materialien verwendet wurden, trat Zersetzung auf. Die zugrundeliegende chemische Instabilität und mögliche Ursachen, um einen plausiblen Reaktionsmechanismus zu erarbeiten, wurden untersucht.

Den zweiten Schwerpunkt dieser Arbeit bilden skalierbare Herstellungsmethoden für ASSB-Komponenten. Diverse Polymere wurden als Binder für SE-Schichten getestet. Dabei wurde deren Einfluss auf Prozessparameter und Eigenschaften der SE-Schichten untersucht. Im Anschluss wurde getestet, wie die Prozessparameter die Homogenität von Kathoden beeinflussen, um so Stellschrauben zu identifizieren.

Insgesamt zielt diese Doktorarbeit nicht nur auf ein besseres Verständnis des ASSB-Konzepts ab, sondern bietet auch Richtlinien für die Herstellung von ASSB-Komponenten und somit ein mögliches Zelldesign für Automobilanwendungen.

Contents

ACKNOWLEDGEMENT	I
ABSTRACT	II
LIST OF ACRONYMS	VI
1 INTRODUCTION	1
1.1 LITHIUM – FUEL OF THE FUTURE?	1
1.2 THE ALL-SOLID-STATE BATTERY	5
1.3 CURRENT CHALLENGES IN ASSB RESEARCH	8
1.3.1 THE SOLID ELECTROLYTE	8
1.3.2 THE SOLID ELECTROLYTE/LITHIUM METAL INTERFACE	11
1.3.3 THE COMPOSITE CATHODE	13
2 MATERIALS AND METHODS	15
2.1 USED MATERIALS	15
2.2 MODIFICATIONS AT THE LI METAL SE INTERFACE	16
2.3 PROCESSING METHODS FOR ASSB COMPONENTS	17
2.4 USED EXPERIMENTAL TECHNIQUES	19
3 RESULTS	27
3.1 TOWARDS ENABLING THE LITHIUM METAL ANODE	27
3.1.1 STRATEGIES TO STABILIZE THE LI METAL/SOLID ELECTROLYTE INTERFACE	28
3.1.2 CHEMICAL STABILITY BETWEEN DIFFERENT SOLID ELECTROLYTES	33
3.2 TOWARDS THE FABRICATION OF ASSB COMPONENTS ON LARGE-SCALE	51
3.2.1 SLURRY-BASED PROCESSING OF SOLID ELECTROLYTES	51
3.2.2 PROCESSING PARAMETERS FOR COMPOSITE CATHODES	68
4 CONCLUSIONS	71
REFERENCES	77

List of Acronyms

Abbreviation	Description
ASSB	All-Solid-State Battery
BEV	Battery Electric Vehicle
CAM	Cathode Active Material
CNF	Carbon Nanofibers
DOL	1,3-Dioxolane
EDX	Energy-Dispersive X-ray Diffraction
EIS	Electrochemical Impedance Spectroscopy
FTIR	Fourier Transform Infrared Spectroscopy
HNBR	Hydrogenated Nitrile Butadiene Rubber
LATP	Lithium Aluminum Titanium Phosphate ($\text{Li}_{1.3}\text{Al}_{0.3}\text{Ti}_{1.7}(\text{PO}_4)_3$)
LCO	Lithium Cobalt Oxide (LiCoO_2)
LGPS	Lithium Germanium Thiophosphate ($\text{Li}_{10}\text{GeP}_2\text{S}_{12}$)
LIB	Lithium-Ion Battery
LiTFSI	Lithium Bis(Trifluoromethanesulfonyl)Imide
LLZO	Lithium Lanthanum Zirconium Oxide ($\text{Li}_7\text{La}_3\text{Zr}_2\text{O}_{12}$)
LPS	Lithium Thiophosphate ($\text{Li}_2\text{S}\cdot\text{P}_2\text{S}_5$)
LSPS	Lithium Tin Thiophosphate ($\text{Li}_{10}\text{SnP}_2\text{S}_{12}$)
NMC	Lithium Nickel Manganese Cobalt Oxide ($\text{LiNi}_x\text{Mn}_y\text{Co}_z\text{O}_2$)
NMR	Nuclear Magnetic Resonance Spectroscopy
PC	Propylene Carbonate
PEO	Poly(Ethylene Oxide)
PIB	Poly(Isobutene)
SE	Solid Electrolyte
SEI	Solid Electrolyte Interphase
SEM	Scanning Electron Microscopy
SES	Solid Electrolyte Separator
SPE	Solid Polymer Electrolyte
XPS	X-ray Photoelectron Spectroscopy

1 Introduction

1.1 Lithium – Fuel of the Future?

The latest BP statistical review of world energy disclosed a drastic growth of worldwide primary energy consumption of 2.2% in 2017, corresponding to the fastest growth since 2013. As Figure 1.1 demonstrates, today's main energy sources still are oil (34%), coal (28%) and gas (23%). Renewable energy sources and hydroelectricity cover only 4% and 7%, respectively, nuclear energy 4%.¹

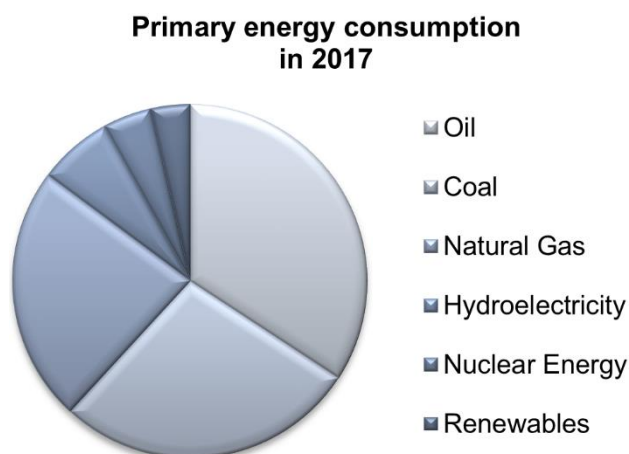


Figure 1.1. Worldwide primary energy consumption in 2017. The data were obtained from the latest BP statistical review of world energy.¹

The report moreover revealed that after three years of little to no growth in carbon emissions from energy consumption, an increase by 1.6% was recorded in 2017.¹ Not only the resulting impact on climate change but also the limited availability of fossil fuels urgently demand for a higher degree of electrification of power engines.² Battery electric vehicles (BEV) are the source of hope for green and sustained mobility, and simultaneously provide advantages over gasoline-powered vehicles with regard to energy efficiency, performance as well as energy independence.³

Although BEVs are constantly gaining popularity, effective penetration of the mass market requires a significant improvement in energy density and fast-charging capability whilst keeping costs reasonable. Figure 1.2 illustrates the gap between BEVs currently available on the market and the targeted driving ranges and vehicle prices. One main reason for the limited competitiveness of BEVs versus conventional gasoline-powered vehicles are poor driving ranges. Current prismatic cells of BEVs, based on established Li-ion battery (LIB) technologies, provide volumetric energy densities around $450 \text{ Wh}\cdot\text{l}^{-1}$ at cell level.⁴ In contrast, about twice this value is required for targeted driving ranges exceeding 500 km.² In order to successfully access the mass consumer market, battery technologies with higher energy density as well as better rate capability, lifetime, cost and safety have to be developed.⁵

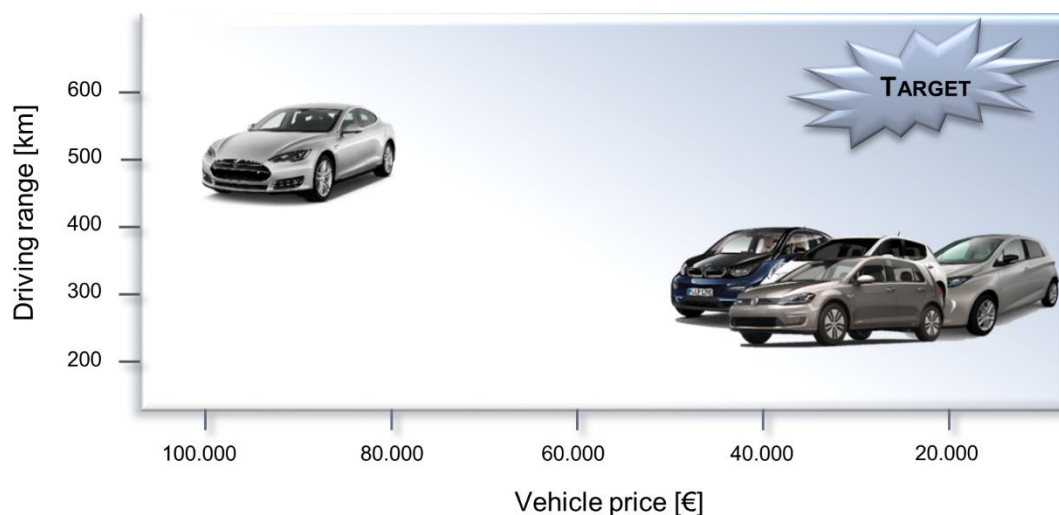


Figure 1.2. Illustration of selected currently available BEVs considering driving range and vehicle price. The target region for effective penetration of the mass consumer market is indicated for comparability.

The most commonly used anode material in nowadays' LIB cell technologies is graphite. Silicon came to the fore in recent years due to its promising theoretical capacity of $4200 \text{ mAh}\cdot\text{g}^{-1}$, which is an order of magnitude larger than that of graphite ($372 \text{ mAh}\cdot\text{g}^{-1}$).⁶ Owing to the large volume expansion of up to 300% upon lithiation, however, pure silicon has not been implemented as anode material in LIB cells yet and is still uncertain for the future.² The most favorable anode material with respect to energy density would be lithium metal. Besides its high theoretical capacity of $3860 \text{ mAh}\cdot\text{g}^{-1}$, it also provides light weight and the lowest potential among all elements.⁷ The combination of metallic lithium with liquid electrolytes in rechargeable batteries though poses severe safety risks and is thus not commercialized to date.²

Regarding the cathode active material (CAM), lithium metal oxides such as LiCoO_2 (LCO), $\text{LiNi}_{0.8}\text{Co}_{0.15}\text{Al}_{0.05}\text{O}_2$ (NCA) or $\text{LiNi}_{1/3}\text{Mn}_{1/3}\text{Co}_{1/3}\text{O}_2$ (NMC-111), which provide theoretical capacities as high as $270 \text{ mAh}\cdot\text{g}^{-1}$, are in the focus.² LCO has been applied successfully in LIBs for almost 30 years. Owing to structural changes at high degrees of delithiation, however, only half the lithium content can be cycled reversibly, resulting in capacities of only $140 \text{ mAh}\cdot\text{g}^{-1}$.⁸ The strive for better LIB technologies demands for higher energy density, voltage and reversible capacity.⁵ Another criterion with regard to large-scale applications is raw materials availability and costs. As a result of the continuously rising cobalt prices, LCO lost further attractiveness.⁹

Due to the high nickel and low cobalt content, higher capacities of $180 \text{ mAh}\cdot\text{g}^{-1}$ and reduced costs can be achieved with NCA.¹⁰ A drawback of the high nickel content is poor thermal stability, which is why NCA undergoes structural changes and oxygen loss at elevated temperatures.¹¹ Manganese helps to improve the thermal stability of NMC materials.¹² NMC-111 used to be the most common CAM in BEVs such as the BMW i3 for many years.¹⁰ Besides its rising price due to the high cobalt content, the limited practical capacity of $160 \text{ mAh}\cdot\text{g}^{-1}$ caused a shift of the focus to Ni-rich NMCs. The increased reversible capacity and improved rate capability with higher nickel content though is accompanied with a reduced thermal stability and higher capacity fading as well as with oxygen release upon heating and/or delithiation.^{12,13} In order to improve the performance of LIBs employing Ni-rich NMCs it is thus necessary to mitigate their surface reactivity,⁵ which will be discussed later. Andre et al. recently reviewed potential cathode materials, including energy density calculations at the automotive battery cell level.⁵ The benefits of selected electrode materials on energy density and cell costs in relation to the 94 Ah battery cell of the BMW i3 are presented in Figure 1.3.

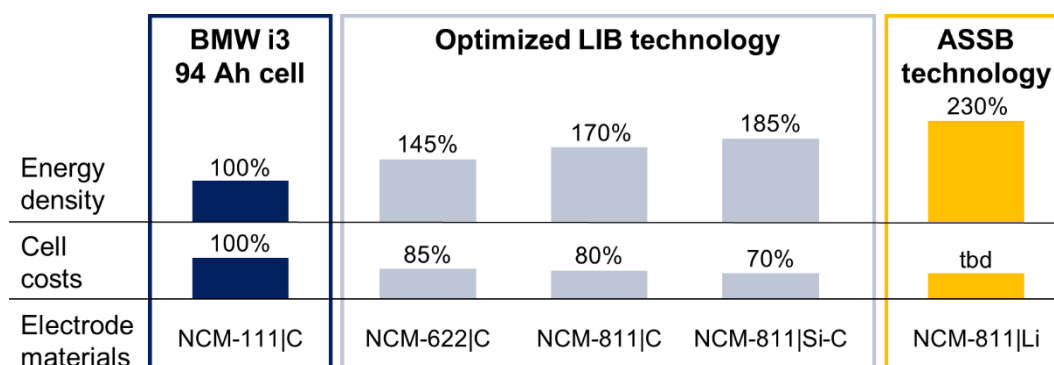


Figure 1.3. Trend of energy density and cell costs for future battery cell technologies, starting from the 94 Ah prismatic cell of the BMW i3. For comparability, the same cell design is considered in all cases.⁵

Apart from energy density and costs, additional key-performance parameters for a battery cell for automotive applications have been defined. These are illustrated in Figure 1.4 for the 94 Ah battery cell of the BMW i3 in comparison to the target for 2025. The map emphasizes that not only higher energy density and lower costs, but also better charging capability and low temperature performance are required.⁵ In order to close the large gap concerning energy density, the LIB technology has to be optimized to its maximum potential. This means above all implementation of high capacity cathodes and anodes (i.e. Li metal) as well as reduction of the separator thickness. These modifications though imply considerable safety concerns, which is why literature states that the energy density of LIBs might soon reach a limit.^{14,15}

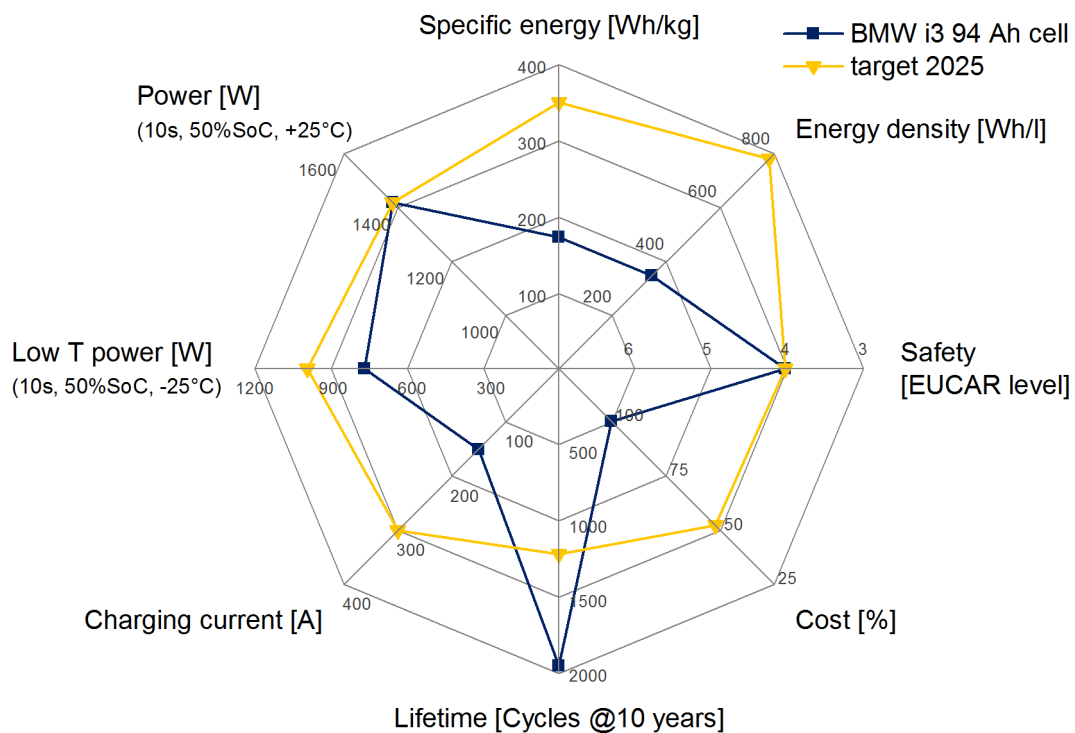


Figure 1.4. Key-performance parameters for a battery cell for automotive applications. Data from the 94 Ah cell of the BMW i3 are compared to the target values for 2025.⁵

As a consequence, novel cell technologies gained significance in the field of battery research.¹⁵ One promising concept to potentially enable the lithium metal anode is the all-solid-state battery (ASSB), which contains a solid electrolyte (SE) instead of the liquid electrolyte and the separator.^{14,16} As shown in the right column of Figure 1.3, implementation of a lithium metal anode in an ASSB cell results in a significant gain in energy density. The underlying principle of the ASSB as well as associated assets and drawbacks will be discussed in the following chapters.

1.2 The All-Solid-State Battery

The schematic setup of an ASSB cell in comparison to a conventional LIB cell is illustrated in Figure 1.5. The most important difference is that the liquid electrolyte (depicted in blue) is substituted by a solid one (shown in yellow). The porous graphite anode is further replaced by lithium metal, which is the reason for the increase of up to 70% in volumetric and 40% in gravimetric energy density of the ASSB cell.^{14,17}

In both cell concepts the cathode comprises an active material, a conductive agent and – depending on the way of processing – a binder.^{18,19} However, during cathode fabrication for conventional LIBs, only electronic pathways have to be established, as ionic conductivity is ensured afterwards by the liquid electrolyte penetrating the voids of the porous electrode. In contrast, ionic and electronic percolation has to be achieved at the same time in an all-solid-state cathode. Owing to the competition of polymeric binder, solid electrolyte and carbon additive for the surface area of the active material particles, fabrication of so-called composite cathodes is quite complex.²⁰ Respective strategies will be discussed in greater detail in chapter 2.3.

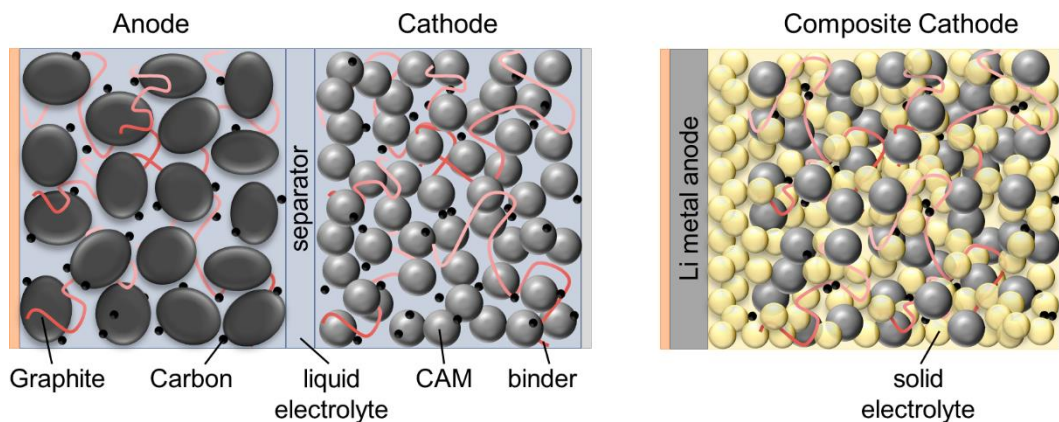


Figure 1.5. Schematic setup of a conventional LIB cell (left) and an ASSB cell (right). Besides replacement of the porous graphite anode by a lithium metal anode, the most important difference is the substitution of the liquid electrolyte (blue) by a solid one (yellow).

The main functions of the solid electrolyte are establishment of fast Li-ion conduction through the cell and, at the same time, prevention of electronic short-circuiting. Therefore, several conditions apply, including high ionic and negligible electronic conductivity, low resistances across the solid electrolyte/electrode interfaces and high electrochemical as well as chemical stability.^{21,22} For large-scale application in BEVs, additional environmental and economic requirements such as low costs, low toxicity, light weight and good thermomechanical properties have to be fulfilled.^{22,23}

Besides the possibility to enable energy rich electrode materials like lithium metal, there are also a series of potential benefits from solid electrolytes over liquid ones. From a safety point of view, the rigid structure prohibits leakage and flammability and possibly reduces the risk of short-circuiting. Higher thermal stability does not only affect safety, but also applicable temperature operation ranges. Performance advantages are attributed to the fact that (inorganic) SEs are single-ion conductors with a Li^+ transference number close to unity. Therefore, concentration gradients cannot arise, which enables higher power densities. In addition, chemical cross-talk between the electrodes is prevented, meaning that electrode components cannot travel across the battery. This also reduces the risk of internal self-discharge.^{14,24,25}

With regard to the type of solid electrolyte used as well as the battery specifications, different types of ASSBs can be described. The first ASSBs have already been developed in the 1970's.²⁶ These were primary, i.e. non-rechargeable thin-film batteries (Figure 1.6a) based on the Li-I₂ system, which are still applied in medical implants like pacemakers and hearing devices.²⁷ Ten years later, Hitachi introduced a secondary thin-film ASSB comprising a lithium metal anode, a titanium disulfide cathode and the solid electrolyte $\text{Li}_{3.6}\text{Si}_{0.6}\text{P}_{0.4}\text{O}_4$.²⁸ Thin-film batteries gained further importance with the discovery of lithium phosphorus oxynitride (LiPON) by Bates et al. in the 1990's.^{29,30} Besides the small dimensions, e.g. 10 – 15 μm cell stack thickness, excellent cycling performance over thousands of cycles paved the way for commercialization of thin-film batteries in low power applications in the aerospace sector, military facilities and medical instrumentation.^{25,29,31}

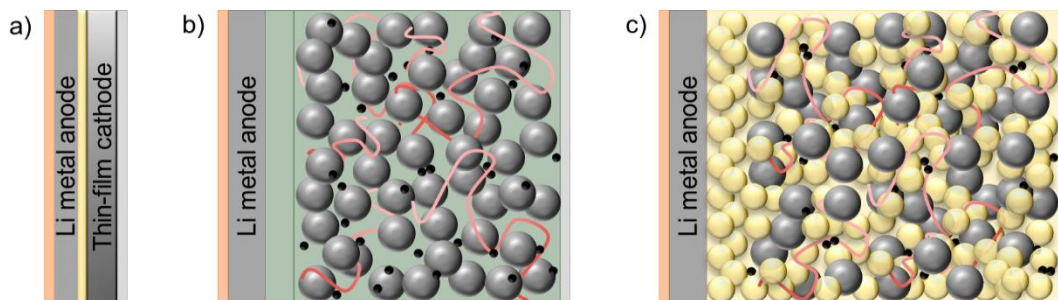


Figure 1.6. Schematic setup of different ASSB types. a) Thin-film cell with a sputtered SE layer (yellow). b) Polymer ASSB using a polymer electrolyte (green) as the solid electrolyte separator (SES) and in the cathode. c) Bulk-type ASSB employing an inorganic SE (yellow) as the SES and in the composite cathode.

The requirements for high power applications like BEVs differ. Regarding the key-performance parameters given in Figure 1.4, thin-film ASSBs do by far miss the targeted charging capabilities, as they are limited to low currents in the μA range.³² In addition, low energy densities and small capacities of less than 1 mAh make them unsuitable for automotive applications.^{25,32,33} Furthermore, considering cost, common fabrication processes such as sputtering are expensive and hardly scalable.³¹

In consequence, bulk-type ASSBs with thicker electrodes and thus higher capacities have to be developed for high power applications. Increasing the cathode thickness though demands for high chemical diffusion rates.²⁵ This means that a solid electrolyte with a high ionic conductivity of at least $10^{-4} \text{ S}\cdot\text{cm}^{-1}$ has to be incorporated in the cathode.¹⁸ So far, commercialization only succeeded for ASSBs employing a solid polymer electrolyte (SPE, Figure 1.6b). The reason for this is that processing of SPEs is much easier than of inorganic ones.³⁴ In addition, their ductile and soft nature enables good contacting at the SPE/electrode interfaces in the production process as well as during battery operation. The first BEV running on a polymer battery has been launched by Bolloré in 2011. Their battery, comprising a lithium metal anode, a LiFePO_4 cathode and a polyethylene oxide (PEO) based electrolyte, however only provides a energy density of roughly $250 \text{ Wh}\cdot\text{l}^{-1}$ at cell level.^{33,35} Moreover, owing to the poor ionic conductivity of SPEs in the range of $\mu\text{S}\cdot\text{cm}^{-1}$, the working temperature range of polymer-based ASSBs is restricted to $60 - 80 \text{ }^\circ\text{C}$ and even then the rate capability is limited.²¹ Overall, polymeric batteries can only become competitive to current LIBs if improved charging rates and energy densities are achieved.¹⁷

Higher ionic conductivity and thus lower operation temperatures could be enabled with inorganic SEs (Figure 1.6c).³⁶⁻³⁸ However, transition from laboratory test cells to industrial products did not succeed yet.^{18,39} One major reason is that lab cells are usually produced by cold-pressing of the crude powder materials.³⁹ This method leads to thick SE layers and low active material loadings, thus yielding poor energy densities below $50 \text{ Wh}\cdot\text{l}^{-1}$ at cell level.^{40,41} Furthermore, compression methods are not suitable for large-scale manufacturing processes.¹⁸ More recent approaches to produce sheet-type ASSBs using slurry-based processes are still on the research level and need to be scaled up.³⁹ Apart from that, limited understanding of the interactions between the different materials in an ASSB hinders commercialization.^{18,39} Major issues in this context will be discussed in detail in the following chapter.

1.3 Current Challenges in ASSB Research

After discussing the main characteristics of the ASSB concept, associated challenges with regard to automotive applications shall be reviewed. This chapter is divided into issues related to the solid electrolyte itself, the SE/electrode interfaces and the composite cathode in particular. The key challenges at cell level, including mechanical, chemical and electrochemical ones, are illustrated in Figure 1.7.

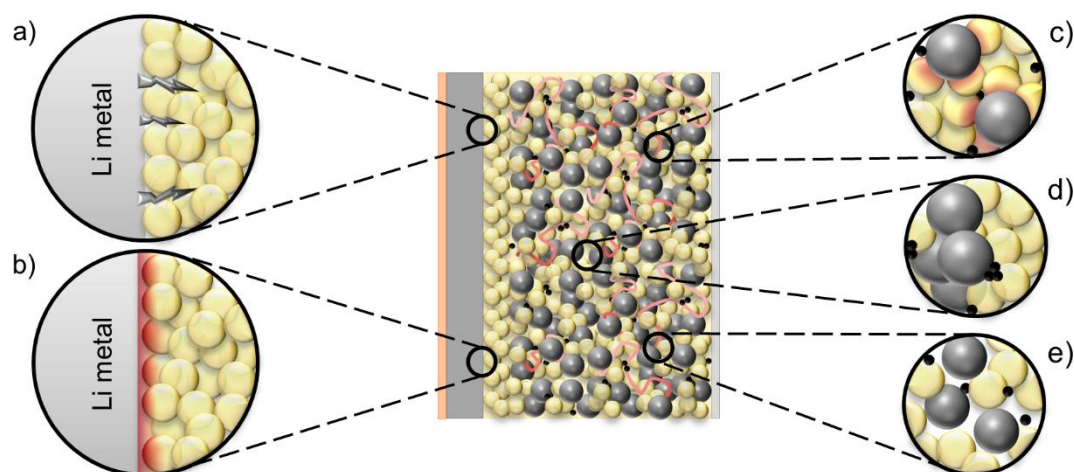


Figure 1.7. Schematic illustration of challenges associated with ASSBs at cell level. a) Li dendrite growth into the SE layer, b) decomposition at the Li metal/SE interface, c) degradation at the CAM/SE interface, d) inhomogeneous distribution of cathode components and e) contact losses in the composite cathode.

1.3.1 The Solid Electrolyte

As mentioned, solid polymer electrolytes that contain a polymer such as PEO and a conductive salt like lithium bis(trifluoromethanesulfonyl) imide (LITFSI) show low ionic conductivities in the range of $\mu\text{S}\cdot\text{cm}^{-1}$.²¹ Poor conductivity has also been seen as a major issue of inorganic solid electrolytes for a long time.¹⁴ Indeed, first oxide-based SEs such as the lithium superionic conductor (LISICON) $\text{Li}_{14}\text{ZnGe}_4\text{O}_{16}$, which was discovered in 1978 by Hong et al., feature low ionic conductivities on the order of $10^{-7} \text{ S}\cdot\text{cm}^{-1}$.^{34,42} Enhanced oxide-based materials like garnet $\text{Li}_7\text{La}_3\text{Zr}_2\text{O}_{12}$ (LLZO) or $\text{Li}_{1.3}\text{Al}_{0.3}\text{Ti}_{1.7}(\text{PO}_4)_3$ (LATP) provide higher conductivities of 10^{-4} and $10^{-3} \text{ S}\cdot\text{cm}^{-1}$, respectively.^{43–45} They further exhibit high chemical and electrochemical stabilities. Drawbacks with regard to application in bulk-type ASSBs arise from their hardness, which leads to brittleness and high interfacial resistances. Consequently, the power density of oxide-based ASSBs is rather limited.²⁵ In order to reduce the interfacial resistances, high temperature annealing steps are required during processing.^{16,46}

Compared to oxygen anions, sulfur anions feature a larger ionic radius and a higher polarization capability. As conduction properties are affected by the size and polarizability of the constituent ions and the size of the transport bottlenecks, replacement of oxygen by sulfur in thio-LISICONs resulted in much higher conductivities.⁴⁷ The thio-LISICON family, described by the general formula $\text{Li}_{4-x}\text{A}_{1-x}\text{B}_x\text{S}_4$ ($A = \text{Si, Ge}$; $B = \text{P, Al, Zn, Ga}$), was established in 2000 by Kanno et al.⁴⁸ Among them, the $\text{Li}_2\text{S-GeS}_2\text{-P}_2\text{S}_5$ system turned out to be the best, with $\text{Li}_{3.25}\text{Ge}_{0.25}\text{P}_{0.75}\text{S}_4$ showing the highest conductivity of $2.2 \text{ mS}\cdot\text{cm}^{-1}$ and the lowest activation energy of $20 \text{ kJ}\cdot\text{mol}^{-1}$.⁴⁹ In 2011, Kanno and co-workers also found $\text{Li}_{10}\text{GeP}_2\text{S}_{12}$ (LGPS) with a comparable activation energy of $24 \text{ kJ}\cdot\text{mol}^{-1}$, but a much higher conductivity of $12 \text{ mS}\cdot\text{cm}^{-1}$.³⁷ As shown by computational and experimental studies, the 3D framework of $(\text{Ge}/\text{P})\text{S}_4$ and PS_4 tetrahedra in LGPS provides 1D diffusion pathways for Li-ions along the c-axis. Additional diffusion in the a-b-plane results in 3D conductivity (Figure 1.8).^{50,51}

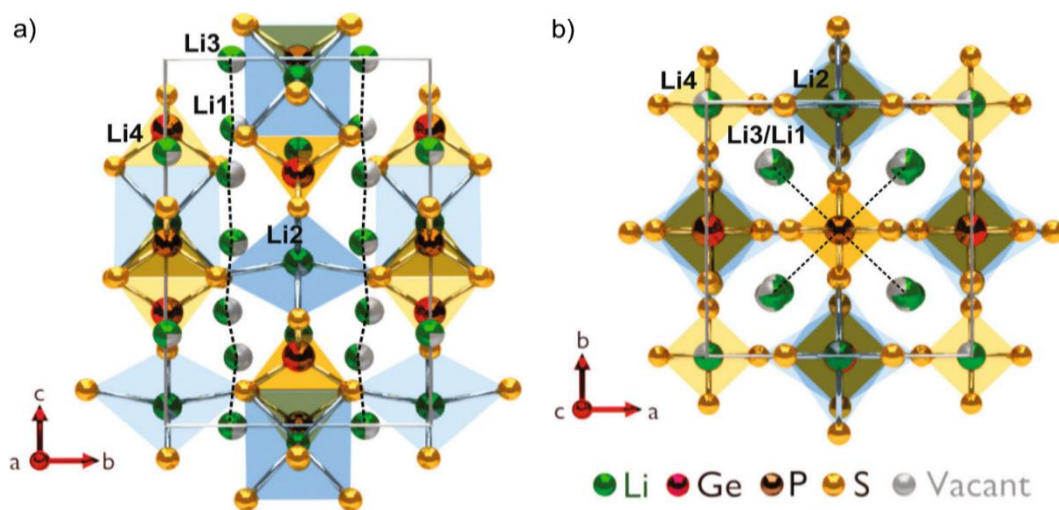


Figure 1.8. Crystal structure of LGPS in a polyhedral representation. The framework of PS_4 and $(\text{Ge}/\text{P})\text{S}_4$ tetrahedra (yellow) as well as LiS_6 octahedra (blue) is viewed along the a) [100] and b) [001] direction. Lithium diffusion pathways are indicated by dotted lines. Reprinted with permission from Lotsch et al., *J. Electroceram.* 2017, 38, 128–141.⁵² Copyright © 2017 B.V. Lotsch.

Ong et al. performed first principles calculations on the $\text{Li}_{10\pm 1}\text{MP}_2\text{X}_{12}$ compounds ($M = \text{Ge, Si, Sn, Al, P}$; $X = \text{O, S, Se}$), predicting similar properties for the other sulfide materials.⁵³ In line with this, $\text{Li}_{10}\text{SnP}_2\text{S}_{12}$ (LSPS) and $\text{Li}_{10}\text{SiP}_2\text{S}_{12}$ with conductivities of 4 and $2 \text{ mS}\cdot\text{cm}^{-1}$, respectively, were reported later.^{54–56} Besides the LMPS compounds, other sulfide materials like $70\text{Li}_2\text{S}\cdot 30\text{P}_2\text{S}_5$ (LPS) and $\text{Li}_{9.54}\text{Si}_{1.74}\text{P}_{1.44}\text{S}_{11.7}\text{Cl}_{0.3}$ show high conductivities of up to $25 \text{ mS}\cdot\text{cm}^{-1}$, exceeding that of current liquid electrolytes.^{36–38} Compared to oxide-based materials, their softness moreover allows for better contacting and thus lower grain-boundary and interfacial resistances.^{16,57}

While limited conductivity is no issue with these materials any more, poor electrochemical stability of most sulfide-based SEs causes big issues. This will be discussed in detail in the following section. Apart from that, limited chemical stability leads to additional difficulties during manufacturing, as they can only be handled in inert atmosphere due to severe reactivity with moist air.¹⁸ Another challenge that also applies to oxide-based SEs arises from energy density calculations. These revealed that SE layers in the range of 20 – 30 μm are required to obtain reasonable energy densities on cell level.³⁹ In combination with lithium metal, such a thin SE separator poses the risk of short-circuiting due to dendrite growth at higher current densities (Figure 1.7a). Despite the former assumption that the mechanical strength of inorganic SEs inhibits dendrite formation,²⁴ various studies showed the opposite in soft polymer and sulfide-based SEs, but also in sintered oxide-based SE layers.^{39,58–60}

From a manufacturing point of view, layers of less than 100 μm cannot be produced by the common lab scale approach of cold-pressing the SE powders.¹⁸ Not only the required pressure, but also the remaining porosity would be too high. Hence, novel processing methods have to be developed. Recent reviews pointed out that relevant synthesis and implementation methods are rare to find in the literature.^{18,39} Another production requirement is a certain mechanical flexibility of the SE layer. This might further be necessary to withstand mechanical stress and ensure interfacial contacting in the ASSB cell. A slurry-coating process that enables both fabrication of thin layers and introduction of a flexible component is thus indispensable.¹⁸

Even among the reports on slurry processing of ASSB electrodes, however, most SE layers were still prepared by powder compression.^{41,61–64} True sheet-type ASSBs were fabricated if graphite anodes were employed, which enable coating of the SE layer on top.^{61,65,66} Only Lee et al. coated the SE directly on a NMC cathode.⁶⁴ While this concept might allow for easier processing steps, thinner SE layers and better SE/electrode contacting, it also involves some challenges. According to Ito et al, using the same binder in the electrode and the SE layer causes mutual dissolution at the interface.⁶⁶ Consistently, Schnell et al. stated that the binder employed in the composite electrode must not dissolve in the solvent used for the SE layer.¹⁸ These issues were avoided by Jung and co-workers, who used a porous polymer material as scaffold for a free-standing SE sheet.^{67,68} In addition, separate fabrication of the SE layer allowed them to analyze its properties without any disturbing effects from the electrodes. However, a high amount of non-conductive material had to be used.

1.3.2 The Solid Electrolyte/Lithium Metal Interface

Limited electrochemical stability is another electrolyte-related issue especially for sulfidic materials. While first experimental studies on LGPS, for example, predicted an outstanding stability window exceeding 0 – 5 V vs. Li/Li⁺,^{37,69} computations by Mo et al. indicated that a kinetically stabilized passivation layer is responsible for masking of the true electrochemical stability window.⁵⁰ A narrow thermodynamic stability range of 1.7 – 2.1 V vs. Li⁺/Li as well as chemical instability towards metallic lithium and cathode materials such as LCO and NMC was finally proven for LGPS by computational and experimental studies.^{70–72} Mo and Ceder et al. also calculated the stability ranges of various other SEs.^{71,73,74} Selected ones are given in Figure 1.9.

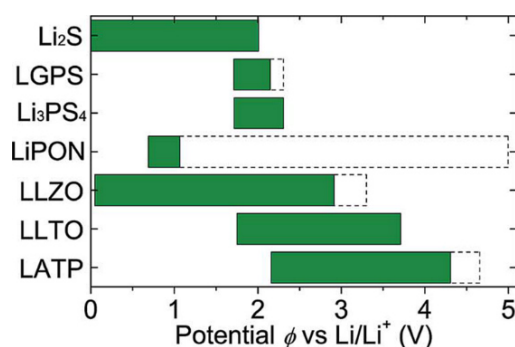


Figure 1.9. Electrochemical stability ranges of selected SE materials. Adapted from Zhu et al., *J. Mater. Chem. A* 2016, 4, 9, 3253-3266.⁷⁴ Copyright© 2016, with permission from The Royal Society of Chemistry.

Numerous recent studies demonstrated that the electrochemical stability of SEs has been overestimated.^{70,71,75–79} A narrow stability range leads to a chemical potential gap between the SE and the electrodes, thereby inducing interfacial decomposition reactions. As in conventional LIBs, this results in the formation of a solid electrolyte interphase (SEI) at the electrode/electrolyte interface.⁷ In ASSBs, different types of Li metal/SE interfaces can be described.⁷⁶ While a thermodynamically stable one would be the most desirable, no SE was found to be stable at the low potential of Li metal. Solely LLZO is considered kinetically stable at 0 V. vs. Li⁺/Li due to its low reduction potential of 0.05 V. vs. Li⁺/Li and unfavorable decomposition kinetics.⁷¹ A thermodynamically unstable interface provokes chemical reactions. If the degradation products are ionically, but not electronically conductive, a metastable SEI emerges. This has been observed at the interface of Li metal e.g. with Li₆PS₅Cl,⁷⁸ Li₇P₃S₁₁⁷⁷ and LiPON.⁷⁵ In case of a mixed conducting interphase, Li-ions and electrons can migrate and the interphase grows into the bulk SE (Figure 1.7b). This has been found for SEs like LGPS,⁷⁰ lithium lanthanum titanate⁷⁶ and LATP.⁷⁹

Besides searching for new materials that are stable at the low potential of metallic lithium, engineering of the interface with the solid electrolyte separator (SES) might enable the lithium metal anode. A protective interlayer could mitigate the chemical potential gap and thereby passivate the interface.^{73,74} Such an artificial SEI of defined structure and thickness should prevent decomposition of the solid electrolyte and ideally also dendrite growth.^{57,72,80} In addition, good physical contact both with lithium metal and the SES is essential to minimize interfacial resistances.⁸¹

One concept that has been studied in conventional LIBs is pretreatment of lithium metal with an organic solvent. Ding et al., for instance, found that the pre-reaction of lithium with 1,4-dioxane and 1,3-dioxolane, respectively, resulted in a smoother surface morphology and thereby improved interfacial and cycling stability.^{82,83} Such a wet-chemical pretreatment has also been proposed for Li/S batteries by Nimon et al.⁸⁴ Another approach comprises sputtering thin interlayers onto either the SES or the lithium metal anode.^{85–90} Decomposition of various SEs was inhibited with thin-films of Li-ion conductors like LiPON,^{85,86} metals such as gold⁸⁹ or indium⁹¹ as well as metalloids like silicon.⁸⁷ Kato et al. found that this also smoothens the lithium surface during cell operation (Figure 1.10).⁸⁹ Due to the high costs, however, most sputtering techniques are unattractive for large-scale applications. Limited conductivity and degradation of the interlayers are further challenges to be met.³¹

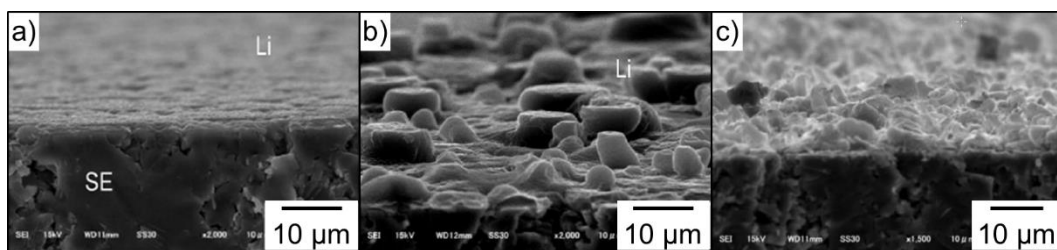


Figure 1.10. SEM images of a) the pristine Li metal/SE interface, b) the Li surface after galvanostatic cycling and c) the Li metal/SE interface with artificial SEI after galvanostatic cycling. Adapted from Kato et al., *J. Power Sources* 2016, 309, 27–32.⁸⁹ Copyright © 2016, with permission from Elsevier.

Thin polymer interlayers, which have been implemented in conventional LIBs^{92–95} and Li-air batteries based on lithium metal electrodes,^{96,97} might be better suited in terms of manufacturing costs. As mentioned, successful application of solid polymer electrolytes in ASSBs is often reported in the past 40 years.^{98–104} More recently, Lee et al. applied PEO-based membranes as interlayers in a Li | LATP | NMC cell.¹⁰⁵ They could thereby prevent degradation of LATP at metallic lithium and decrease the

interfacial resistance. Although PEO is also not thermodynamically stable in contact with lithium metal, it has been demonstrated that stable cycling succeeds due to the formation of a passivating SEI.^{24,106} The favorable effect of polymer interlayers in combination with oxide-based electrolytes has also been shown by Zhou et al., who reported improved cycling stability and dendrite resistance in lithium and sodium based ASSB cells.^{107,108} This architecture has moreover been tested in a different context, namely as a preventive measure for breakage of the SES and contact losses at the SES/electrode interfaces due to volume changes during cycling.^{109,110}

1.3.3 The Composite Cathode

Electrochemical stability issues also arise at the cathode side. While high operation voltages up to 5 V vs. Li⁺/Li are desired, the oxidative degradation of most SEs starts at much lower potentials. NASICON materials like LATP have the highest oxidation potential of roughly 4.2 V. LLZO as well as most sulfide materials, however, are oxidized already below 3 V.⁷¹ Hence, decomposition layers likewise emerge at the SE/CAM interface (Figure 1.7c). A common strategy to mitigate the surface reactivity of active materials in conventional LIBs is coating the particles with metal oxides like Al₂O₃ or ZrO₂.⁵ The amorphous buffer layer enables charging to higher cut-off voltages and thus higher reversible capacities, as electrolyte decomposition is lowered, resulting also in a better cycling stability.⁸

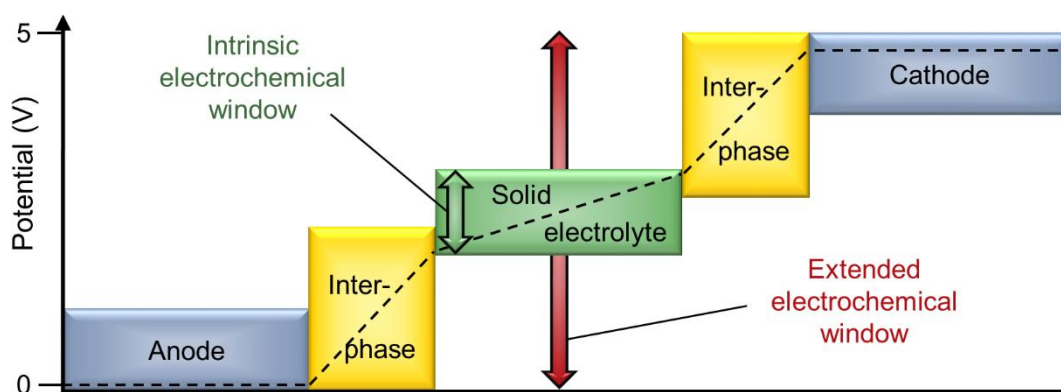


Figure 1.11. Schematic diagram on the electrochemical window (color bars) and the Li chemical potential profile (black line) in an ASSB cell. The intrinsic electrochemical stability window of the SE (green) can be extended (red) by applying interphases (yellow) between the SE and the electrodes (blue).

As at the anode side, the coating layer bridges the chemical potential gap and thereby passivates the AM/SE interface.^{73,74} By implementing interphases between the solid electrolyte and both electrodes, the electrochemical stability range of the SE

can be extended significantly, as illustrated by the red arrow in Figure 1.11.⁷¹ The beneficial effect of CAM coatings on cell performance has also been demonstrated in ASSBs. Machida et al., for instance, prevented decomposition of sulfidic LPS by using a ZrO₂ coating on NMC.¹¹¹ Ohta et al. studied LiNbO₃- and Li₄Ti₅O₁₂-coated LCO in composite cathodes with another sulfide-based SE, showing enhanced high-rate capability.^{112,113} Recently, Koerver et al. indicated that not only the CAM/SE interface but also the current collector has to be coated to prevent degradation.¹¹⁴

Apart from that, the strong effect of the cathode morphology on cell performance gives rise to manufacturing difficulties. First of all, homogeneous distribution of the components is crucial, as the accessible capacity is reduced in case of an insufficient electronic and ionic percolation (Figure 1.7d).^{14,19} Besides, good physical contact is essential to lower the interfacial resistances. Contrary to electrodes in LIBs, the porosity of ASSB cathodes thus needs to be minimized.^{18,39} Moreover, as intercalation materials exhibit volume changes, strategies to maintain mechanical integrity during cycling have to be developed.³⁹ The unit cell of LCO, for example, expands during delithiation, whereas that of NMC shrinks.¹¹⁵ In conventional LIBs, the liquid electrolyte can adapt to volume changes. The rigidity of inorganic SEs though leads to inconsistent interfaces^{14,21} and thereby high overvoltages and capacity fading in ASSBs (Figure 1.7e).¹¹⁵ The usage of lithium metal anodes aggravates this problem, as the metal foil also shrinks and expands during cycling. Stable long-term cycling of ASSB cells therefore requires application of an external pressure during operation.^{14,18,20} Recent studies on slurry processing of composite cathodes indicate that, as for the SES layer, introduction of a flexible polymeric binder helps to ensure mechanical durability as well as adhesion to the current collectors.^{40,64,65} However, as mentioned before, this additional component that likewise competes for the surface area of the CAM particles further complicates the manufacturing process.²⁰

In summary, the large number of challenges described in this section – which is not a complete list – gives an impression how important further fundamental investigation of ASSB cells is to optimize the cell design. Neither a full understanding of the degradation phenomena taking place at the SE/electrode interfaces nor a complete cell setup for automotive applications has yet been proposed. In this PhD thesis, two key challenges were investigated in detail: Engineering of the Li metal/SE interface and processing methods for the SES layer as well as the composite cathode.

2 Materials and Methods

2.1 Used Materials

At the beginning of this chapter, the main materials employed in this thesis shall be introduced. All of them were handled in an argon-filled glovebox (GS glovebox systemtechnik) and used without further purification. An oxide- and a sulfide-based SE material were employed in the work presented in section 3.1. $\text{Li}_{1.3}\text{Al}_{0.3}\text{Ti}_{1.7}(\text{PO}_4)_3$ (LATP) pellets of 12 mm diameter and roughly 100 μm thickness were provided by the Forschungszentrum Jülich GmbH. The fabrication method based on tape casting has been described elsewhere.¹¹⁶ $\text{Li}_{10}\text{SnP}_2\text{S}_{12}$ powder (>95%, LSPS) was purchased from NEI Corp. Lithium metal foil (99.9%, 750 μm), propylene carbonate (>99%, PC) and 1,3-dioxolane (>99.5%, DOL) were obtained from Alfa Aesar. Polymer films were made of polyethylene oxide (PEO, M_w 10^6 $\text{g}\cdot\text{mol}^{-1}$), polyethylene glycol dimethyl ether (PEGDME, M_w 2000 $\text{g}\cdot\text{mol}^{-1}$) as well as bis(trifluoromethane)sulfonimide lithium salt (99.95%, LiTFSI) purchased from Sigma Aldrich Corp.

Different polymeric binders were employed in the work presented in section 3.2.1. Polyisobutene (PIB, M_w of $3.1\cdot 10^6$ $\text{g}\cdot\text{mol}^{-1}$) was delivered by BASF SE. Poly(methyl methacrylate) (PMMA, M_w $4\text{-}5.5\cdot 10^5$ $\text{g}\cdot\text{mol}^{-1}$) was purchased from Alfa Aesar and poly(styrene-co-butadiene) (SBR, M_w $1.9\cdot 10^5$ $\text{g}\cdot\text{mol}^{-1}$) at 4 wt.% butadiene content from Sigma Aldrich Corp. Poly(ethylene vinyl acetate) (PEVA, M_w $3.5\cdot 10^5$ $\text{g}\cdot\text{mol}^{-1}$) at 60 wt.% VA content and poly(acrylonitrile butadiene) (HNBR, $5.5\cdot 10^5$ $\text{g}\cdot\text{mol}^{-1}$) with 17 wt.% acetonitrile content were provided by Arlanxeo. Toluene was purchased from Merck Millipore. The same LSPS powder from NEI Corporation was used.

In addition to these materials, a commercially available coated $\text{LiNi}_{0.6}\text{Mn}_{0.2}\text{Co}_{0.2}\text{O}_2$ (NMC-622, coating cannot be specified) material and carbon nanofibers (<100 ppm Fe, CNF) from Sigma Aldrich Corp. were used for the fabrication of composite cathodes described in section 3.2.2.

2.2 Modifications at the Li Metal | SE Interface

In the work presented in chapter 3.1.1, different strategies to stabilize the interface between the lithium metal anode and the solid electrolyte separator (SES) by a protective layer were investigated. The ability of the interlayers (Figure 2.1) to prevent decomposition reactions was probed in symmetric Li | Li cells using LATP and LSPS pellets, respectively, as the SES. LATP pellets were used as provided, whereas LSPS pellets with a thickness of roughly 0.5 mm were produced by compacting 100 mg powder within a 12 mm diameter stainless steel pellet die at 5 tons (430 MPa) for 20 min. The impact of the interlayers on interfacial stability and cell performance was evaluated by means of cycling as well as calendar life aging tests, which will be further explained in section 2.4.

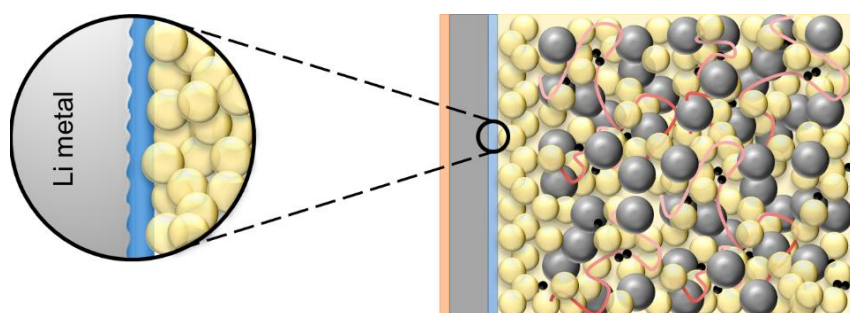


Figure 2.1. Schematic setup of an ASSB with an artificial SEI (blue) implemented between the lithium metal anode (grey) and the SES layer (yellow).

Pretreatment of lithium metal with organic solvents was attempted first. Inspired by a study from Ding et al., who tested pretreated lithium metal electrodes in conventional LIBs,^{82,83} propylene carbonate (PC) and 1,3-dioxolane (DOL) were selected as test solvents. Lithium metal disks of 12 mm diameter were dipped for 1 min into the solvent and dried at ambient conditions to let the surface structure develop.

Furthermore, application of thin polymer layers between lithium metal and the SES was tested. One concept was to coat a PEO-LiTFSI film directly on the SE pellet and the metal electrode, respectively, from an acetonitrile solution and vacuum-dry the samples at 80 °C. Alternatively, free-standing polymer films were fabricated either solution-based or by hot-pressing. The former included coating of the acetonitrile solution on Mylar® foil and vacuum drying at 80 °C. Hot-pressed PEO, PEGDME and PEO₁₅LiTFSI membranes of a thickness of 30 – 50 µm were produced by pressing the material powders at a P 200 PM press (Collin) at 100 °C and 50 kN for 15 min.

2.3 Processing Methods for ASSB Components

The second part of this thesis focuses on scalable processing methods for the fabrication of solid electrolyte layers and composite cathodes. In contrast to the thick and fragile LSPS pellets produced by powder compression in section 3.1, thin and flexible LSPS sheets shall be fabricated by a slurry-based approach in section 3.2.1.

The slurry-coating process is represented in Figure 2.2. First, the LSPS powder was dispersed and the polymeric binder dissolved in the solvent toluene by stirring. The respective amount of binder solution was then added to the LSPS dispersion. After stirring for 12 h, the viscosity of the slurry was adjusted and it was coated on siliconized polyester foil (PPI Adhesive Products GmbH) using the doctor blade technique. The cast film was dried for 1 h at ambient conditions and further 12 h under dynamic vacuum. Subsequent calendering to yield the final SE sheet was performed in a sealed aluminum foil pouch at 60 °C outside the glovebox. The gap size was reduced by 10 μm per step until the pouch bag started curling up.

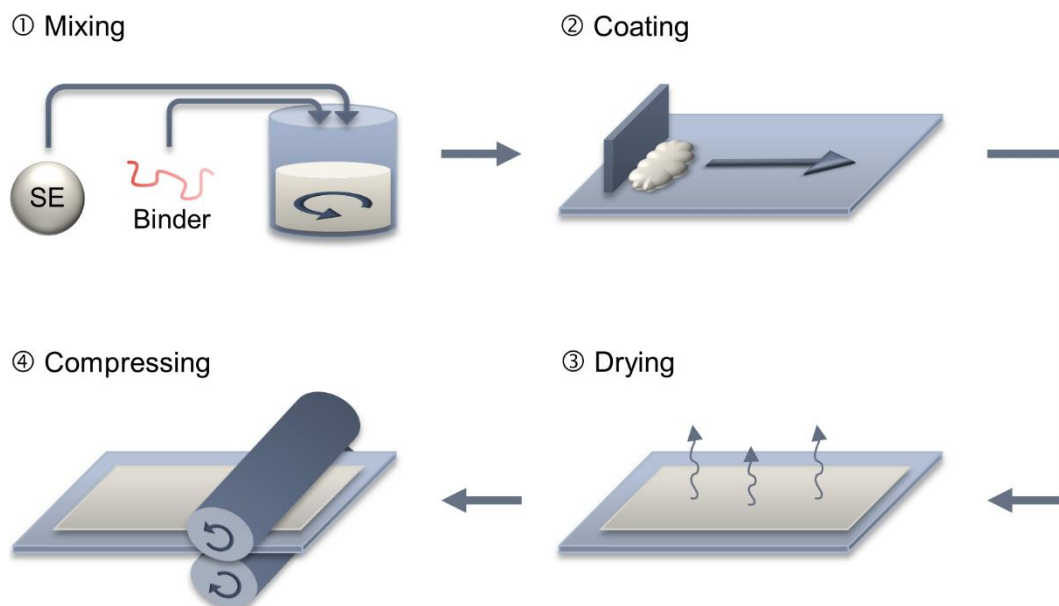


Figure 2.2. Schematic illustration of the slurry-coating process applied for SE layers in this thesis. (1) Mixing of the components. (2) Coating of the slurry on a carried foil using the doctor blade technique. (3) Drying under vacuum at ambient temperature. (4) Compressing by means of a calender at 60 °C.

For the slurry-based fabrication of composite cathodes presented in section 3.2.2, a cathode composition had to be identified first. Nam et al. tested various CAM shares, obtaining the highest reversible capacity for a CAM/SE ratio of 70:30 wt.%.⁶⁵ They moreover found that dry premixing of the two components has a beneficial effect.

In this thesis, the slurry process was optimized with regard to percolation. As mentioned, ionic and electronic pathways have to be established simultaneously during fabrication of composite cathodes. To focus on the effect of mixing and distribution, a fixed composition of 68.1 wt.% NMC-622, 29.2 wt.% LSPS, 1.3 wt.% CNF and 1.4 wt.% binder was chosen, according to Nam et al.⁶⁵ Variations were made regarding the type of binder used, the premixing and the mixing procedure (Figure 2.3).

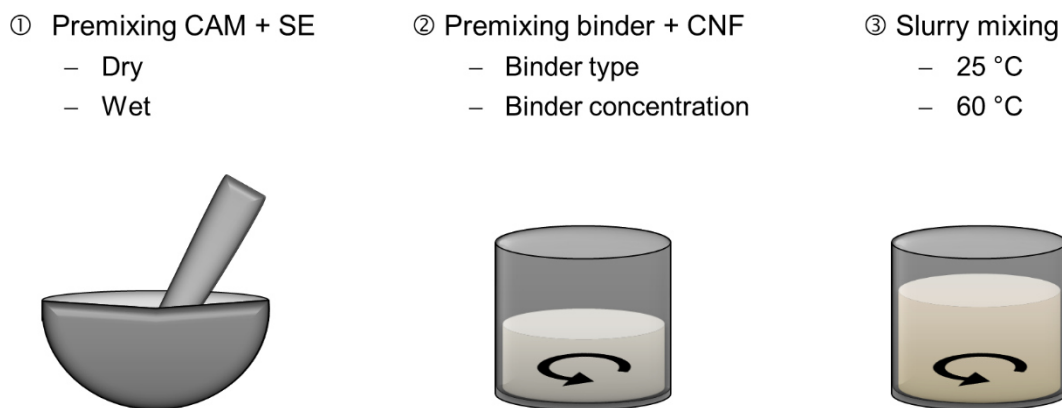


Figure 2.3. Varied parameters during slurry processing of composite cathodes within this thesis. (1) Premixing of CAM and SE under dry and wet conditions. (2) Premixing of binder and CNF using different binders at different concentrations. (3) Mixing of the final slurry at different temperatures.

The premixing of NMC and LSPS using mortar and pestle was either performed dry or by adding a small amount of solvent. In parallel, the CNF were dispersed in the binder solution. Two binders, namely PIB and HNBR, at different concentrations between 0.5 – 3.0 wt.% were probed. The NMC/LSPS mixture was then added to the CNF/binder dispersion and the slurry was stirred either at room temperature or at 60 °C. The subsequent coating process was performed as described for the SE layer (see Figure 2.2), using aluminum foil (Hydro-Aluminium) as the carrier foil and an applicator gap size of 200 μm . For densification, the cathodes were either punched into 12 mm diameter disks and compressed with a stainless steel pellet die at 6 t or calendered inside the glovebox at ambient temperature. The gap size was reduced by 10 μm per step until the aluminum foil started corrugating.

For evaluation of the distribution pattern of the cathodes, scanning electron microscopy (SEM) and energy-dispersive X-ray diffraction (EDX) was conducted. Electrochemical impedance spectroscopy (EIS) was used to examine first electrochemical properties. For this purpose, compressed cathodes were assembled in symmetric cells with a slurry-processed LSPS sheet as the SES. These as well as further main techniques used in this thesis will be explained in the following chapter.

2.4 Used Experimental Techniques

In the studies presented in chapter 3, a large variety of electrochemical and analytical methods was employed. The most important techniques shall be introduced in the following. Electrochemical tests were mainly conducted using TSC battery cells (RHD instruments). As shown in Figure 2.4, they comprise an airtight PEEK housing and a Ni-plated base that is equipped with a PT100 temperature sensor. The current collectors are pressed onto one another by means of a spring with defined spring constant that is fixed by a screw. Knowing the thread pitch and the number of turns, the applied pressure can be calculated. In contrast to other test cell setups, the TSC battery cell thus allows for setting of a defined load. Owing to technical restrictions of the cell setup, however, the maximum pressure is limited to roughly 1 MPa.

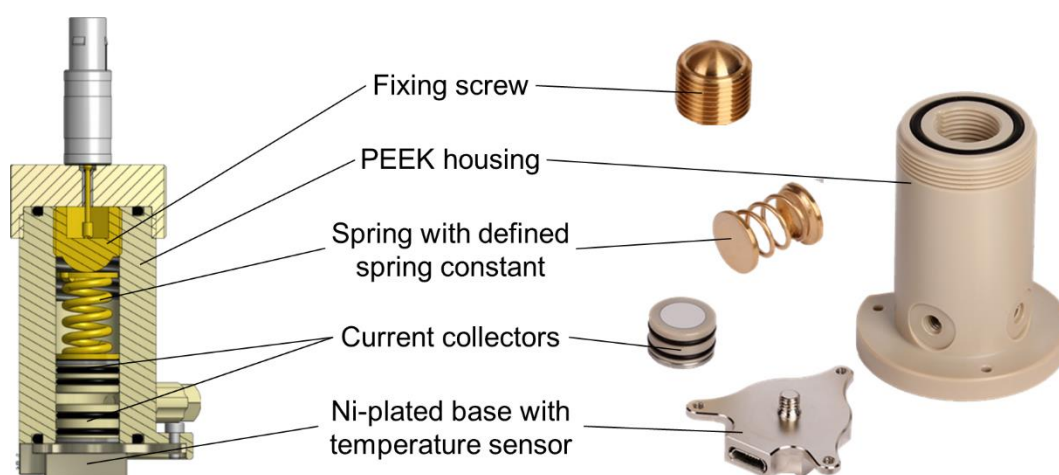


Figure 2.4. Schematic drawing (left) and images (right) of the components of a TSC battery cell.¹¹⁷

In the work presented in section 3.1, symmetrical cells were tested. These comprise two lithium metal electrodes (\varnothing 10 mm, 750 μm), an LSPS (\varnothing 12 mm, \sim 500 μm) or an LATP pellet (\varnothing 12 mm, \sim 100 μm) and optionally polymer interlayers (\varnothing 12 mm, \sim 30 μm). According to the literature standard, the cells containing polymer layers were first heated to 60 $^{\circ}\text{C}$ to ensure good interfacial contacting.¹⁰⁶ EIS, which will be explained in the following, was probed either in a temp. range or at constant temp. Cycling tests were run at 40 $^{\circ}\text{C}$ at current densities of 0.01 – 0.1 $\text{mA}\cdot\text{cm}^{-2}$.

In order to test the slurry-processed SE layers (\varnothing 12 mm, \sim 30 μm) in section 3.2.1, they were compressed between aluminum foils (\varnothing 12 mm, 10 μm). The composite cathodes in section 3.2.2 were probed in symmetrical cells employing two cathodes (\varnothing 12 mm, \sim 80 μm) and a slurry-processed LSPS layer (\varnothing 12 mm, \sim 30 μm).

Electrochemical impedance spectroscopy (EIS).

EIS probes the ability of a circuit to resist an electrical current and store electrical energy. The working principle of this main electrochemical test method shall be explained in more detail. In general, the impedance Z is the frequency dependent resistance of a system. Experimentally, it can be measured by applying an AC voltage signal with an amplitude U_{amp} over a wide frequency range and recording the current response.¹¹⁸ While linearity of the system is an essential condition during the measurement, real electrochemical systems usually behave in a non-linear fashion. The input signal thus has to be chosen small enough to reach a pseudo-linear state. In the case of a linear, causal and time invariant system, the sinusoidal voltage input at a certain frequency f results in a sinusoidal current output of the same frequency, however with a shift in phase (Figure 2.5a). According to equation 2.1, the complex impedance $Z(f)$ at a certain frequency is defined by the voltage amplitude U_{amp} , the current amplitude I_{amp} and this phase shift $\Delta\varphi$.

$$Z(f) = \frac{U_{amp}}{I_{amp}} \cdot e^{j \cdot \Delta\varphi} \quad (2.1)$$

A full impedance spectrum is obtained by repeating this measurement at different frequencies. Figure 2.5b shows the Nyquist plot for a model electrical circuit with each data point representing one $Z(f)$ measurement. The circuit consists of a serial resistor R , a resistor connected in parallel to a capacitor R/C and a serial capacitor C . At high frequencies, the impedance through the capacitor of the R/C element is much lower than through the parallel resistor, which is why the real impedance part $Re(Z)$ dominates. In contrast, the current mainly flows through the resistor at low frequencies, resulting in a predominantly capacitive impedance response $Im(Z)$.¹¹⁸

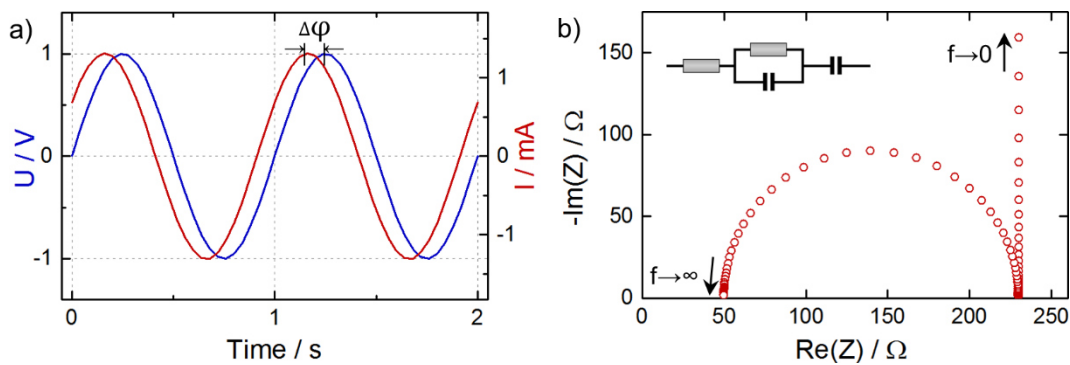


Figure 2.5. a) Sinusoidal voltage input V at a single frequency $f = 1$ Hz and current response I . b) Nyquist plot of an impedance spectrum simulated for the model electrical circuit shown in the top left.

In an ASSB cell, different contributions to the overall resistance are expected. Common physical and electrochemical processes are illustrated in Figure 2.6 for a schematic cell. At very high frequencies, signals originate from electrical resistances R_{el} of the cables and the cell housing. In addition, bulk and grain-boundary resistances R_{GB} of the SE appear at high frequencies. Contributions in the mid-frequency range include interfacial contact and charge-transfer resistances R_{CT} between the Li metal anode and the SES as well as between the SE and the CAM. At low frequencies, semi-infinite diffusion W inside the CAM particles and contact resistances $R_{contact}$ between the cathode and the current collector foil can be detected.^{119,120}

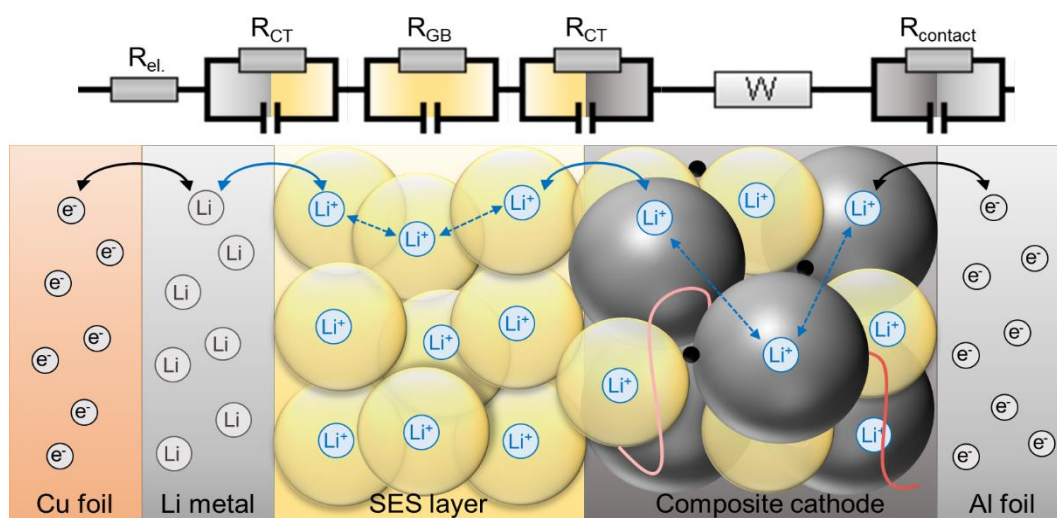


Figure 2.6. Schematic drawing of different processes contributing to the overall impedance of an ASSB cell. The respective elements of the electrical equivalent circuit used for EIS analysis are presented above.

EIS spectra in this thesis were probed with an Autolab M101 impedance analyzer (Metrohm) in a frequency range between 1 MHz – 1 mHz at an amplitude of 20 mV. When temperature variant tests were performed between 0 – 60 °C, the cells were kept at the respective temperature for 3 hours prior to the measurement. For calendar aging tests, temperature was kept constant and impedance was measured every 12 – 24 h for 7 – 30 days. For deconvolution of the different contributions and quantification of the resistances, the spectra were then fitted using electrical equivalent circuits and the RelaxIS software package (RHD instruments).

Depending on the cell setup, different fitting models were required. Suitable circuit elements that represent the different processes had to be identified. A pure resistor R can be used to model ionic resistances of the bulk SE as well as electrical resistances. Transport processes across grain boundaries and electrochemically active interfaces, which appear as semicircles in the Nyquist plot, can be described by R/C

elements. As most solid-solid interfaces show a non-ideal capacitive behavior due to inhomogeneities at the surface, constant phase elements are often used instead of ideal capacitors.^{120,121} Semi-infinite diffusion processes, which result in a 45° line at low frequencies, can be fitted by a Warburg diffusion element W .^{119,120}

A suitable electrical equivalent circuit for the various processes referred to above is given in the top of Figure 2.6. The large number of circuit elements highlights the complexity of analyzing EIS spectra of full cells. It should be noted that detrimental processes that affect the cell impedance, e.g. additional resistances originating from decomposition layers, were not even considered here. Hence, the equivalent circuit of real ASSB cells can be even more complex. It is thus worth to probe the different components separately, i.e. by assembling the SES in blocking conditions between current collectors to exclude charge-transfer and diffusion processes or built symmetrical cells to minimize the number of contributions. Knowing the characteristics of the individual components then allows interpreting the spectrum of a full cell.

Scanning electron microscopy (SEM).

For detailed investigation of the surfaces and compositions of various ASSB components, SEM in combination with energy dispersive X-ray diffraction (EDX) mapping was conducted. The samples were mounted on the sample holder and transferred to the SUPRA 55VP (Zeiss) microscope in an airtight transport vessel to minimize exposure to ambient air (< 5s). The schematic setup of a scanning electron microscope is represented in Figure 2.7. During the experiment, a primary electron beam is focused on the sample and the emerging secondary signals are detected. As illustrated, interaction of this beam with the sample surface induces emission of high-energy backscattered electrons, low-energy secondary electrons as well as X-rays.

While the backscattered electrons are used to create a topographical image of the sample surface, SEM itself cannot provide chemical information. The emitted X-rays though are characteristic for an atomic structure and yield a unique series of peaks in the X-ray spectrum. Hence, an elemental map of the sample surface can be obtained by detecting the characteristic energies via an EDX analyzer. In this thesis, EDX mapping was mainly used to evaluate the distribution of the components in the SE and cathode sheets fabricated in the work presented in chapter 3.2. SEM imaging helped to analyze the surface structure, homogeneity and porosity in all studies.

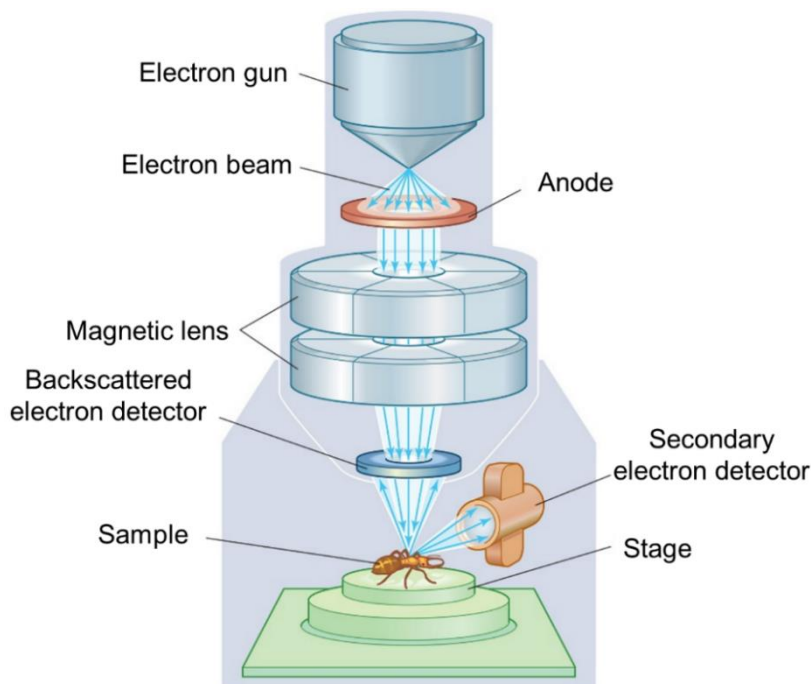


Figure 2.7. Setup of an scanning electron microscope, reproduced from Encyclopædia Britannica.¹²²

X-ray photoelectron spectroscopy (XPS).

If not only the type of element, but also its oxidation state is of interest, XPS can be used. Similar to SEM, a primary beam is focused on the sample and the emitted electrons are detected, whereby soft X-rays instead of electrons are used in XPS. The underlying principle is based on the photoelectric effect, namely that ionization of atoms by absorption of X-ray photons leads to emission of core electrons. These are of discrete kinetic energy that corresponds to the difference between the energy of the radiated photon and the binding energy of the emitted electron, corrected by an instrumental work function. XPS spectra are then obtained by plotting the number of emitted electrons per energy versus their kinetic energy. Quantitative information can be received by separating and integrating the peaks. As the binding energy is characteristic for atoms of different elements and different oxidation states, the emitted electron beam provides insights not only into the elemental composition on the surface, but also into the chemical state of the respective elements.¹²³⁻¹²⁵

While the history of XPS goes back to the early 20th century,¹²⁵ the method has been limited to *ex-situ* applications until recently in terms of battery research. In 2013, the group of Janek introduced a setup for *in-situ* lithiation of solid electrolytes.⁷⁹ This enables chemical analysis of lithium metal/SE interfaces and interphases during formation.⁷⁶ For instance, while the reaction products that emerge during

decomposition of LGPS in contact with lithium metal have only been predicted by computation before,⁷¹ Wenzel et al. used *in-situ* XPS to experimentally prove them.⁷⁰ They observed rising peak intensities of Li₂S (orange), metallic Ge (purple) and Li₃P (green) with increasing lithium deposition on a LGPS sample (Figure 2.8).

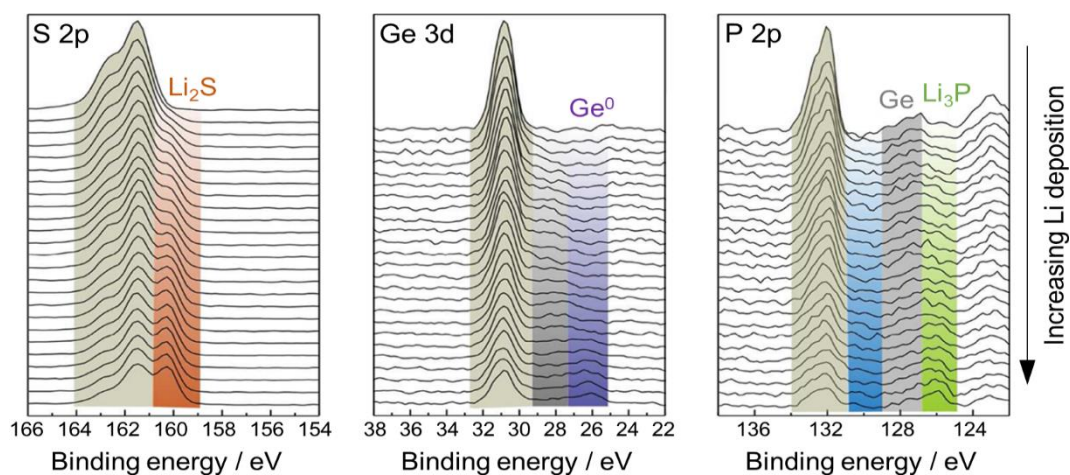


Figure 2.8. XPS spectra recorded during deposition of Li metal on LGPS. S 2p, Ge 3d, and P 2p/Ge 3p detail spectra at different deposition states are arbitrary shifted for better visibility. The identified decomposition species are marked and labeled in the spectra. Adapted with permission from Wenzel et al., Chem. Mater. 2016, 28, 2400–2407.⁷⁰ Copyright © 2016 American Chemical Society.

In this thesis, XPS was employed in the work presented in section 3.1.2 and 3.2.1. In particular, chemical stability between LSPS and different polymers was probed and possible degradation products were identified. Special attention had to be paid to sample preparation, as contaminations e.g. by ambient atmosphere can provoke decomposition reactions, thereby posing a risk for false data evaluation. The sample holder was thus prepared inside an argon-filled glovebox and transferred into the load lock of the XPS system without air exposure using a transfer vessel (Kratos).

XPS spectra were recorded with an Axis Supra system (Kratos) using monochromatic Al K α radiation ($h\nu = 1486.6$ eV) in hybrid lens mode with the instrument's charge neutralizer turned on. The high radiation energy enables penetration depths in the order of 1 – 10 nm. In some experiments, sputtering was used to remove potential surface impurities and probe the inner surface of the sample. Sputtering was performed using an argon ion cluster gun at an acceleration voltage of 10 kV and an argon ion current of 1 μ A. The obtained spectra were processed and fitted using the ESCApe software (Kratos, version 1.1). In line with literature, binding energies were corrected based on the C-C/C-H peak of adventitious carbon at 284.8 eV in the C 1s spectrum.^{77,115,123}

Further analytical techniques.

In addition to the main methods described above, a range of further experimental techniques was employed in the work presented in section 3. As these are standard methods that were performed by project partners, they are only briefly mentioned.

For the detailed chemical analysis in chapter 3.1.2, X-ray diffraction (XRD), Fourier transform infrared spectroscopy (FTIR), UV-Vis spectroscopy and – in collaboration with the group of Sylvio Indris from the Institute for Applied Materials of the Karlsruhe Institute of Technology (KIT IAM) – ^{31}P / ^{119}Sn magic-angle spinning nuclear magnetic resonance spectroscopy (MAS NMR) was conducted. Among these, XRD and MAS NMR helped to identify the impurities and crystalline side phases in the as-received SE material. FTIR and UV-Vis spectroscopy were used to confirm the decomposition products that have been identified by XPS analysis.

Further collaborations emerged in the scope of the processing study described in section 3.2.1. Together with Joscha Schnell from the Institute for Machine Tools and Industrial Management (*iwb*) of the TUM, Mandrel bend tests of the fabricated SE sheets were performed in order to assess their mechanical properties. In a further cooperation with the group of Sylvio Indris, the ionic conductivity of different SE sheets was evaluated by means of pulsed-field gradient (PFG) NMR spectroscopy. Details on their method can also be found in a recent publication on LSPS.¹²⁶

3 Results

All work, published and unpublished, that was carried out within the scope of this PhD thesis is presented in the following. It is grouped along two main topics: Section 3.1 comprises the studies that focus on the lithium metal anode; in section 3.2, all work regarding processing strategies for the other ASSB cell components, namely the solid electrolyte separator layer and the composite cathode, is summarized.

3.1 Towards Enabling the Lithium Metal Anode

The high theoretical capacity of $3860 \text{ mAh}\cdot\text{g}^{-1}$ makes Li metal the most attractive anode material for all Li-based battery technologies.⁷ Indeed, the expected gain in energy density of ASSBs compared to conventional LIBs is based on the assumption that the porous graphite anode can be replaced by a thin lithium foil.¹⁴ However, as discussed in chapter 1.3, several challenges have to be overcome to enable the lithium metal anode in a secondary battery system. One key issue in ASSBs is the poor electrochemical stability of most SEs at the low potential of metallic lithium, which has been demonstrated in various experimental and computational studies during recent years.^{70,71,75-79} Especially when the decomposition products form a mixed-conducting interphase that grows into the bulk SE layer, electronic short-circuiting is a major risk factor for safety and functionality. But even if a metastable SEI forms at the interface, high resistances and thus poor cell performance pose a problem.

As described in chapter 1.3, different strategies addressing this issue are reported in the literature. In the following, selected approaches to stabilize the Li metal/SE interface are evaluated. First, the results obtained with two model solid electrolytes, namely oxide-based LATP and sulfide-based LSPS, are summarized. As a result of these investigations, the stability of two solid electrolytes towards each other was studied in detail. In particular, the degradation of LSPS in contact with a PEO-based solid polymer electrolyte was investigated and possible reasons were evaluated.

3.1.1 Strategies to Stabilize the Li Metal/Solid Electrolyte Interface

In this section, different concepts to stabilize the interface between a solid electrolyte pellet and the lithium metal anode were evaluated. The main motivation behind this study lies in the demand for highly conductive solid electrolytes for high power applications of ASSBs. While high conductivities of up to $25 \text{ mS}\cdot\text{cm}^{-1}$, exceeding that of nowadays liquid electrolytes, were achieved with sulfide-based electrolytes,³⁶⁻³⁸ none of them is thermodynamically stable in contact with metallic lithium.^{70,77,78} An artificial SEI that passivates the Li metal/SE interface is thus required to use these currently most promising solid electrolytes in secondary batteries.⁵⁷ The protective interlayer should moreover improve the physical contact between the lithium metal electrode and the solid electrolyte separator, thus reducing interfacial resistances and minimizing defects at the interface that might provoke dendrite growth.⁸¹

This thesis focuses on two strategies to implement protection layers. As described in section 2.2, the first approach includes wet-chemical pretreatment of lithium metal with organic solvents. The artificial SEI that forms by chemical reactions between lithium and the solvent was found to provide a smoother surface morphology and thereby better cycling stability in Li-ion as well as Li/S batteries.⁸²⁻⁸⁴ The metal electrodes in this study were dipped into propylene carbonate (PC) and 1,3-dioxolane (DOL), respectively, and dried at ambient conditions. The resulting surface morphology in comparison to pristine lithium metal was investigated by means of SEM. Figure 3.1 shows that different structures emerge depending on the solvent used; however, the thickness of these layers could not be determined. With PC a porous layer arises, whereas DOL leads to a homogeneous film on the metal surface.

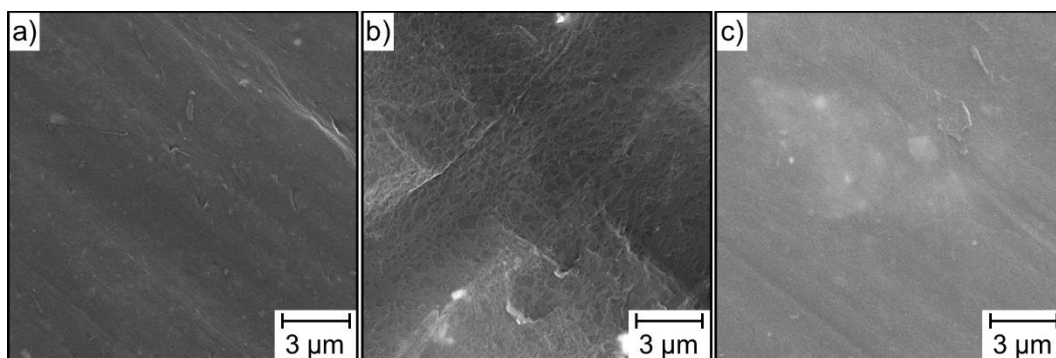


Figure 3.1. SEM images of the surface of a) pristine lithium metal, b) lithium metal pretreated with propylene carbonate (PC) and c) lithium metal pretreated with 1,3-dioxolane (DOL).

Subsequently, electrochemical tests were conducted to probe whether the artificial SEI can stabilize the Li metal/SE interface. For this, pretreated electrodes were assembled in symmetric Li | SE pellet | Li cells. Two representative inorganic solid electrolytes, oxide-based LATP and sulfide-based LSPS, were selected because they are known to decompose rapidly in contact with metallic lithium.^{70,79} This enables a quick assessment of the ability of the interlayers to prevent degradation reactions. The course of the cell impedance over time was explored in calendaric life aging tests. Symmetric cells with pristine Li metal electrodes were tested in comparison.

Figure 3.2 represents the Nyquist plots of the cell impedance of two exemplary LSPS cells employing (a) DOL-treated and (b) pristine Li electrodes. Both show an initial impedance of about 1.2 k Ω . After ageing for one week at 25 °C, the impedance of cell (a) rose by roughly 4 k Ω , whereas that of cell (b) increased only by about 1 k Ω . Comparable results were obtained with cells comprising LATP pellets and PC-treated electrodes, respectively. The interlayer growth thus seems to slow down, but not inhibit the degradation of the Li metal/SE interface. Most likely, the protective surface film is too thin and/or too porous to fully prevent contacting between the Li metal surface and the SE pellet. This strategy was therefore not pursued any further.

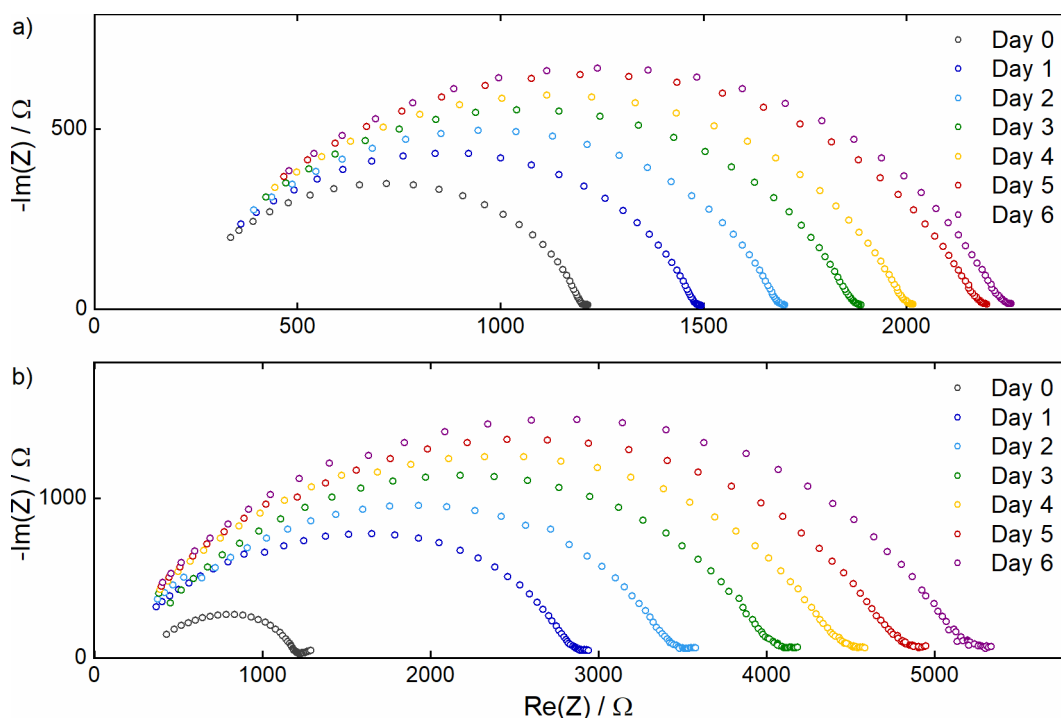


Figure 3.2. Nyquist diagram of the impedance of two Li | LSPS | Li cells at 25 °C. a) The Li metal electrodes were pretreated with DOL. b) Pristine Li metal electrodes were used. The impedance of both cells rises steadily over the storage time of 7 days, indicating an ongoing degradation of the Li metal/LSPS interface.

The second concept investigated in this thesis was to implement thin polymer films as interlayers. Contrary to the pretreatment approach, which results in undefined surface layers, the structure and thickness of polymer films can be adjusted. Contact between the SE pellet and the lithium metal surface can thus be completely avoided. A common solid polymer electrolyte, PEO₁₅LiTFSI, was selected to be tested in symmetric Li | Li cells with LATP and LSPS pellets, respectively.

First, different approaches to fabricate thin polymer films were tested, including (i) direct coating of a polymer solution on either the SE pellet or the lithium metal electrode, (ii) solution-based fabrication of free-standing polymer films and (iii) hot-pressing of free-standing membranes according to Keller et al.¹²⁷ As described in section 2.2, the former two involve preparation of an acetonitrile solution and – in order to remove the solvent after coating – vacuum drying at elevated temperature. The hot-pressing approach just required dry-mixing of the powder materials.

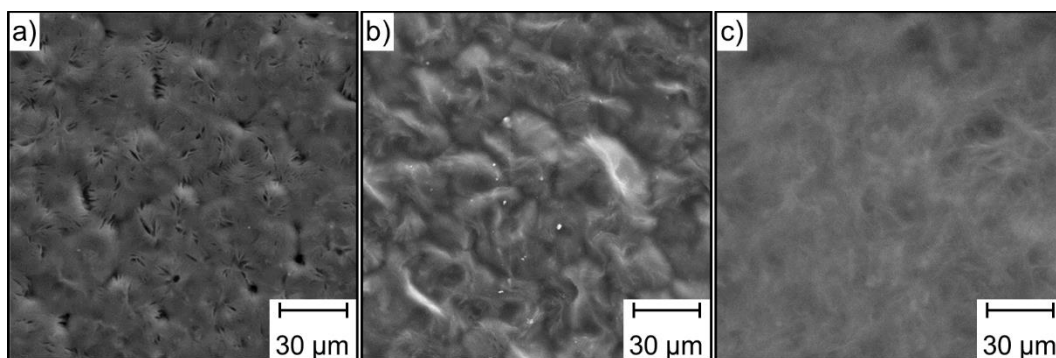


Figure 3.3. SEM images of PEO-LiTFSI films a) coated on a LATP pellet from an acetonitrile solution, b) coated free-standing from an acetonitrile solution and c) prepared by hot-pressing after Keller et al.¹²⁷

SEM analysis revealed that the resulting microstructure varies greatly. Concept (i) forms a pitted and inhomogeneous film, as shown for a polymer-coated LATP pellet in Figure 3.3a. This can be mainly attributed to the drying process, which involves migration of gas bubbles that lead to pore formation. Moreover, chemical reactions between lithium and the solvent form a highly resistive decomposition layer when the solution is coated on Li metal instead of the SE pellet. Approach (ii) leads to a denser film (Figure 3.3b), most likely because the polymer can move freely during the drying process whereas it is attached to the substrate in case (i). A completely dense and homogeneous film though is only obtained by concept (iii), as Figure 3.3c demonstrates. Besides the absence of an evaporation step that causes migration of the polymer, the compression during film formation seems to be beneficial.

Hence, hot-pressed PEO₁₅LiTFSI membranes were selected for subsequent electrochemical testing. The protective properties were also probed in calendaric life aging tests of symmetric Li | Li cells in combination with LATP and LSPS pellets, respectively. The impedance of an exemplary LATP cell is shown in Figure 3.4 for a time span of 30 days. It remained constant over the entire measuring period, indicating that the interlayers successfully prevent degradation reactions. In line with Lee et al., who applied PEO-based membranes as interlayers in a Li | LATP | NMC cell,¹⁰⁵ the resistance was moreover reduced by a factor of three compared to cells without polymer layers, demonstrating that interfacial contacting was enhanced significantly. This can be assigned to the stiffness of the oxide-based electrolyte, whereas the soft polymer electrolyte conforms to both the LATP and the Li metal surface.

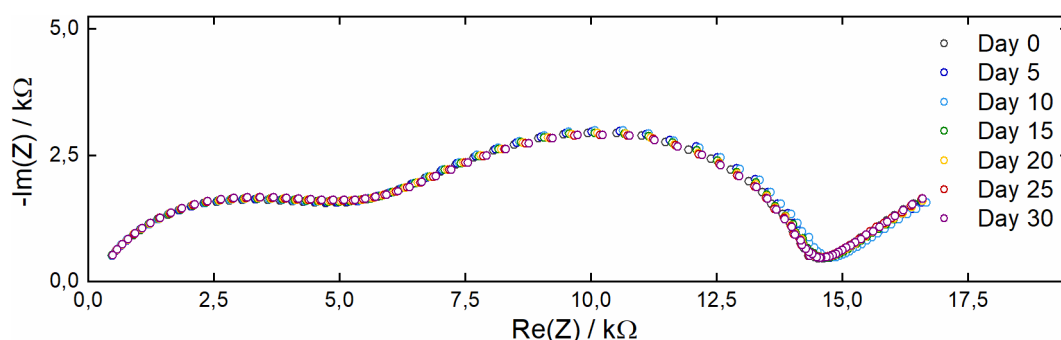


Figure 3.4. Nyquist diagram of the impedance of a Li | PEO₁₅LiTFSI | LATP | PEO₁₅LiTFSI | Li cell stored for 30 days at 40 °C. The cell impedance remains constant over time, indicating stable interfaces.

In order to evaluate the impact of the polymer interlayers on cell performance, symmetric cells were cycled galvanostatically. Due to the low ionic conductivity of the LATP pellets in the range of $\mu\text{S}\cdot\text{cm}^{-1}$, the power density of these cells was very limited. At a low current density of $0.01\text{ mA}\cdot\text{cm}^{-2}$, however, stable cycling was possible for more than 100 cycles without significant changes in overpotential (Figure 3.5).

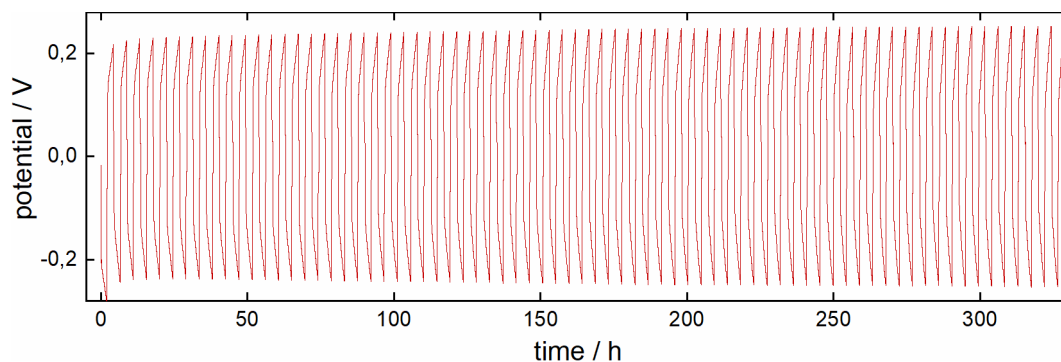


Figure 3.5. Potential vs. time profile of a Li | PEO₁₅LiTFSI | LATP | PEO₁₅LiTFSI | Li cell obtained through galvanostatic cycling at 40 °C for 330 h at a current density of $0.01\text{ mA}\cdot\text{cm}^{-2}$.

In contrast, cycling of LAMP cells without polymer layers resulted in a rapid potential drop and electric short-circuiting. Formation of a mixed-conducting interphase and its propagation into the bulk SE layer likely causes the instability of these cells, as reported in the literature.⁷⁹ This finally confirms that PEO₁₅LiTFSI interlayers can stabilize the Li metal/LAMP interface without impairing the cell performance.

Compared to LAMP, the LSPS pellets in this study provide a three orders of magnitude higher conductivity. While this would enable higher power densities, the low conductivity of the polymer electrolyte is restrictive in LSPS cells. At least a tenfold higher current density of 0.1 mA·cm⁻² though could be applied without aggravating the voltage profile. Despite the comparable cycling data obtained, the calendar life aging results differed strongly. While the resistance of LAMP cells remains constant during the test period of 30 days, that of LSPS cells rises significantly. As Figure 3.6 shows, the cell impedance already increased by 10% over a time span of one week.

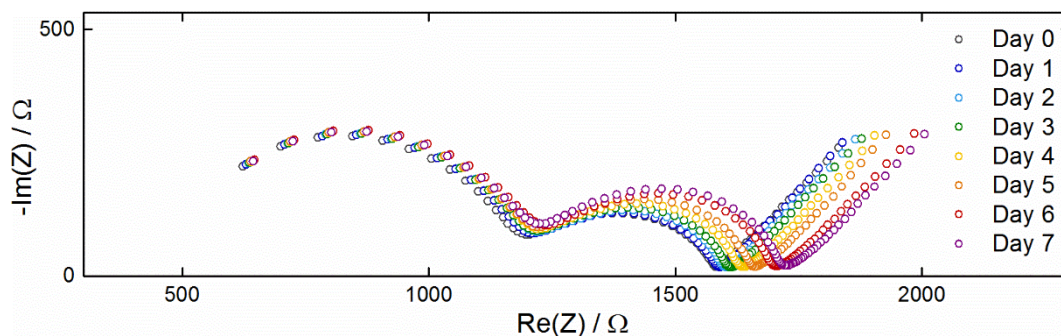


Figure 3.6. Nyquist diagram of the impedance of a Li | PEO₁₅LiTFSI | LSPS | PEO₁₅LiTFSI | Li cell stored for 7 days at 40°C. The cell impedance increased significantly, indicating ongoing degradation processes.

Apparently, PEO-LiTFSI interlayers can prevent degradation in LAMP cells, whereas ongoing decomposition takes place in LSPS cells. The disparate behavior indicates that the solid electrolyte must be somehow involved in the degradation reaction. That, however, was entirely unexpected, as not only the compatibility of LAMP with PEO,¹⁰⁵ but also that of LSPS with PEO has been demonstrated in the literature.¹²⁸ This observation therefore provided the starting point for the detailed investigations on the chemical stability between LSPS and PEO presented in the next chapter.

In conclusion, this study showed that the implementation of a low-cost artificial SEI that simultaneously prevents degradation of the Li metal/SE interface and provides sufficiently high conductivity and stability to ensure high power density is still a big challenge in bulk-type secondary ASSBs.

3.1.2 Chemical Stability between Different Solid Electrolytes

In the following, the article “Understanding Chemical Stability Issues between Different Solid Electrolytes in All-Solid-State Batteries” is presented. It was published in the *Journal of The Electrochemical Society* in March 2019 as Editor’s Choice open access article.¹²⁹ The results of this paper were also presented by Nathalie Riphaut at the 233rd Meeting of The Electrochemical Society in Seattle, USA (May 13th – 17th, 2018), abstract #488.

In this study, the compatibility of PEO-based polymer films with the sulfide-based electrolyte LSPS was evaluated. The driving force for investigating the stability of different solid electrolytes towards each other lies in the results obtained during attempting protection of the Li metal/SE interface. Application of thin PEO₁₅LiTFSI interlayers between lithium metal and a LSPS pellet could not prevent degradation during calendaric aging of the cells. This observation seemed to be in contradiction with a recent study by Blanga et al., who successfully combined PEO and LSPS in a composite electrolyte for Li/S batteries.¹²⁸ As the concept of implementing polymer interlayers at the Li metal/electrolyte interface is well established among various cell technologies including conventional LIBs,^{92–95} Li-air batteries^{96,97} and Li-based ASSBs,^{105,107,109,110,130} we saw an urgent need to understand the origin of the degradation processes occurring in cells that include a PEO/LSPS contact.

Therefore, the interfacial properties between LSPS and a PEO₁₅LiTFSI membrane were analyzed. The continually increasing impedance during first electrochemical tests (see Figure 3.6) already indicated degradation issues. Further experiments revealed that degradation reactions also take place in cells with stainless steel instead of lithium metal electrodes, proving that the origin of degradation is rooted in stability issues between the two solid electrolytes. Therefore, the surface composition at the LSPS/polymer interface was investigated in the next step. By means of XPS, FTIR and UV-Vis spectroscopy decomposition products consisting of polysulfides, P-[S]_n-P like bridged PS₄³⁻ units and sulfite, SO₃²⁻, were identified. Additional analysis of the pristine materials using XRD as well as MAS NMR revealed Li₇PS₆, lithium hydroxide and lithium carbonate as contaminations in the as-received LSPS.

In order to determine the origin of degradation, different possibilities were discussed and various tests were performed to confirm or reject them. In this context, a reaction of LSPS with traces of water or the conductive salt LiTFSI was ruled out, whereas surface impurities on LSPS and the functional groups in PEO turned out to have an influence on the decomposition. Further tests revealed that polysulfides are formed independently of the type of polymer used, while the formation of sulfite requires the presence of hydroxyl groups. As a result of these findings, two separate degradation processes are expected to take place at the LSPS/PEO interface. Based on literature references, a plausible reaction mechanism was developed. In conclusion, this study points out the necessity of an in-depth chemical analysis in addition to electrochemical tests in order to fully understand interfaces in ASSB cells.

Author contributions

Nathalie Riphhaus, Barbara Stiaszny and Hubert A. Gasteiger developed the concept for the study. Nathalie Riphhaus and Hans Beyer carried out the XPS measurements. Sylvio Indris took care of the MAS NMR experiments. All further experiments were conducted by Nathalie Riphhaus. Together with Hubert A. Gasteiger and Stefan J. Sedlmaier, she also wrote the paper. All authors discussed the results and commented on the manuscript.



Understanding Chemical Stability Issues between Different Solid Electrolytes in All-Solid-State Batteries

Nathalie Riphaut,^{1,2,z} Barbara Stiaszny,² Hans Beyer,¹ Sylvio Indris,^{3,4} Hubert A. Gasteiger,^{1,*} and Stefan J. Sedlmaier^{1,2}

¹Chair of Technical Electrochemistry, Department of Chemistry and Catalysis Research Center, Technische Universität München, 85748 Garching, Germany

²BMW Group, 80809 Munich, Germany

³Institute for Applied Materials - Energy Storage Systems, Karlsruhe Institute of Technology, 76344 Eggenstein-Leopoldshafen, Germany

⁴Helmholtz Institute Ulm, 89081 Ulm, Germany

Sulfide-based solid electrolytes (SE) are quite attractive for application in all-solid-state batteries (ASSB) due to their high ionic conductivities and low grain boundary resistance. However, limited chemical and electrochemical stability demands for protection on both cathode and anode side. One promising concept to prevent unwanted reactions and simultaneously improve interfacial contacting at the anode side consists in applying a thin polymer film as interlayer between Li metal and the SE. In the present study, we investigated the combination of polyethylene oxide (PEO) based polymer films with the sulfide-based SE $\text{Li}_{10}\text{SnP}_2\text{S}_{12}$ (LSPS). We analyzed their compatibility using both electrochemical and chemical techniques. A steady increase in the cell resistance during calendar aging indicated decomposition reactions at the interfaces. By means of X-ray photoelectron spectroscopy and further analytical methods, the formation of polysulfides, $\text{P}-[\text{S}]_n-\text{P}$ like bridged PS_4^{3-} units and sulfite, SO_3^{2-} , was demonstrated. We critically discuss potential reasons and propose a plausible mechanism for the degradation of LSPS with PEO. The main objective of this paper is to highlight the importance of understanding interfaces in ASSBs not only from an electrochemical perspective, but also from a chemical point of view.

© The Author(s) 2019. Published by ECS. This is an open access article distributed under the terms of the Creative Commons Attribution 4.0 License (CC BY, <http://creativecommons.org/licenses/by/4.0/>), which permits unrestricted reuse of the work in any medium, provided the original work is properly cited. [DOI: 10.1149/2.0351906jes]



Manuscript submitted February 11, 2019; revised manuscript received March 8, 2019. Published March 26, 2019. This was Paper 488 presented at the Seattle, Washington Meeting of the Society, May 13–17, 2018.

It is often discussed that it might be difficult with today's Li-ion cell technologies to meet future long term targets for application in battery electric vehicles (BEV).^{1–3} In particular, the increasing demand for extended driving ranges, which comes along with higher energy density, conflicts with the limited energy density of conventional Li-ion batteries.¹ While gravimetric energy densities exceeding $300 \text{ Wh}\cdot\text{kg}^{-1}$ are targeted at cell level, only up to $170 \text{ Wh}\cdot\text{kg}^{-1}$ were reached in current EVs.⁴ In addition, high power density is desired due to fast-charging requirements.¹ Consequently, battery research was extended to novel cell technologies. Solid electrolytes (SE) have attracted growing interest as they have the potential to enable the use of metallic Li as anode material. They feature several advantages over liquid electrolytes, such as a rigid and non-leaking structure, non-flammability as well as a larger temperature operation range.^{1,5} All-solid-state batteries (ASSB) thus have great potential to simultaneously enhance safety, lifetime and energy density compared to established Li-ion cell technologies.²

Initially, poor ionic conductivity at ambient temperature has been regarded as the major drawback of SEs, but recent reports prove that this challenge has been met with sulfide-based materials like $\text{Li}_{10}\text{GeP}_2\text{S}_{12}$ (LGPS) or $\text{Li}_2\text{S}\cdot\text{P}_2\text{S}_5$. They provide conductivities as high as $25 \text{ mS}\cdot\text{cm}^{-1}$, exceeding that of current liquid electrolytes.^{6–9} Moreover, their softness allows for good contacting, thus providing lower grain-boundary and interfacial resistance compared to oxide-based SEs. High total cell resistance evolving from rigid solid-solid interfaces indeed is a major issue.^{5,10} In a pure solid system, volume changes of the active materials during cycling lead to a loss of interfacial contact and thus complicate realization of a bulk ASSB.^{11,12} Another problem especially for sulfide-based SEs is their chemical instability not only in contact with air and moisture, but also with Li metal and the cathode materials.^{1,2,10,13} Furthermore, recent studies revealed that their electrochemical stability has generally been overestimated so far.^{14–16} According to Zhu et al., the rather slow decomposition kinetics at the SE/electrode interface, which only gradually lead to high overpotentials, are responsible for a seemingly large stability

window in most electrochemical materials stability screening tests.¹⁶ As a matter of fact, the rather poor oxidative/reductive stability of most SEs requires protection on both cathode and anode side.¹

While coating of the active material is a common strategy to prevent unwanted reactions at the cathode interface,¹⁷ different approaches aim for overcoming decomposition issues at the interface with the Li metal anode. Numerous examples of sputtering thin interlayers onto the SE and Li metal, respectively, have been reported.^{18–21} Li-ion conductors such as LiPON,¹⁸ metals like indium²² or gold²¹ as well as metalloids such as silicon¹⁹ have been proven to effectively prevent decomposition reactions between SEs and metallic Li. However, most sputtering techniques are expensive and thus less attractive for large-scale applications. Moreover, limited ionic conductivity as well as degradation of the interlayers still questions their suitability.²³

An alternative concept, which has been studied in liquid electrolyte based LIBs^{24,25} and in Li-air batteries using Li metal anodes,²⁶ consists in application of a thin polymer film as interlayer. Polyethylene oxide (PEO) based solid polymer electrolytes (SPE) are well established in polymer-based ASSBs, and many successful examples have been reported in the literature.^{27–29} In contrast to inorganic SEs, SPEs provide a certain flexibility, ensuring good contacting at the interfaces.^{3,30}

In a different study, PEO-based membranes were applied between electrodes and $\text{Li}_{1+x}\text{Al}_x\text{Ti}_{2-x}(\text{PO}_4)_3$ (LATP),³¹ an oxide-based SE that is known to rapidly decompose in contact with metallic Li.¹⁰ Thereby, degradation reactions could be prevented, resulting in improved interfacial contacting and decreased interfacial resistance. Although it has recently been demonstrated that also PEO is thermodynamically not stable in contact with Li metal, the formed passivation layer allows for sufficient cycling behavior.^{3,30} Similarly, Zhou et al. reported a beneficial effect of the SPE | oxide-based SE | SPE sandwich architecture on cycling behavior and dendrite stability in lithium and sodium ASSB test cells.^{32,33} The same setup has been examined with regard to its ability to mitigate the risk of SE breakage as well as contact loss between SE and electrodes,³⁴ which is a major issue during cycling due to volume expansions.¹¹

Inspired by this promising concept, we investigated the combination of polymer interlayers with sulfide-based SEs, as they usually feature higher ionic conductivities than oxides.^{1,10} As a model electrolyte,

*Electrochemical Society Fellow.

^zE-mail: nathalie.riphaut@tum.de

we selected $\text{Li}_{10}\text{SnP}_2\text{S}_{12}$ (LSPS), the thiostannate analogue of LGPS that features a comparable conductivity of $2\text{--}4\text{ mS}\cdot\text{cm}^{-1}$,^{7,35} while its cost is significantly lower due to the replacement of germanium with tin, making it more attractive for large-scale applications.⁷ The compatibility of LSPS with PEO has already been tested in a different context. Blanga et al. reported on a composite electrolyte showing improved cycling behavior and safety in Li/S batteries.³⁶ They stated that prolonged annealing of a LSPS-PEO film with the salt LiI at 90°C results in the formation of a novel $\text{Li}_{10+x}\text{I}_x\text{SnP}_2\text{S}_{12}/\text{P}(\text{EO})_3/\text{LiI}$ electrolyte. X-ray photoelectron spectroscopy (XPS) and X-ray diffraction (XRD) were used to characterize the composite. The study though did not include post-mortem analysis, so no conclusions can be drawn with respect to the chemical stability between LSPS and PEO. To the best of our knowledge, this has also not yet been reported elsewhere. In the present study, we analyzed the compatibility of LSPS with PEO-based membranes by examining the interfacial resistance using electrochemical impedance spectroscopy (EIS), by characterizing the surface composition using XPS, as well as by applying further analytical methods. We found clear experimental evidence for the chemical reactivity of LSPS in contact with PEO and we critically discuss potential reasons and propose a plausible degradation mechanism.

Experimental

Materials.—All materials were handled within an argon filled glove box ($\text{O}_2, \text{H}_2\text{O} < 1\text{ ppm}$; GS Glovebox Systemtechnik GmbH). $\text{Li}_{10}\text{SnP}_2\text{S}_{12}$ (>95%, LSPS) was purchased from NEI Corporation and used without further purification. Polyethylene oxide (PEO, $M_w 10^6\text{ g}\cdot\text{mol}^{-1}$), polyethylene glycol dimethyl ether (PEGDME, $M_w 2000\text{ g}\cdot\text{mol}^{-1}$) and bis(trifluoromethane)sulfonamide lithium salt (99.95%, LiTFSI) were purchased from Sigma Aldrich Corp. and dried in a vacuum oven (Büchi B-585 Drying) at 120°C . SE pellets (ca. 0.5 mm of thickness) were obtained by compacting 100 mg of LSPS powder within a 12 mm diameter stainless steel pellet die at 5 tons ($\equiv 430\text{ MPa}$) for 20 min inside the glove box. For preparation of $\text{PEO}_{15}\text{LiTFSI}$ membranes of a thickness of $30\text{--}50\text{ }\mu\text{m}$, 1.25 g of PEO and 0.50 g of LiTFSI were homogenized using mortar and pestle and annealed for 72 h at 100°C under argon atmosphere. The material was hot-pressed between siliconized Mylar foils under argon atmosphere in a P 200 PM press (Collin) at 100°C and $0.5\text{ kN}\cdot\text{cm}^{-2}$ for 15 min. The same procedure was used for preparation of pure PEO and PEGDME membranes.

Cell assembly.—Electrochemical measurements were conducted in air-tight two electrode TSC battery cells (rhd instruments). Cells were stacked in the following order: Li metal electrode (AlfaAesar, $\varnothing = 10\text{ mm}$, $750\text{ }\mu\text{m}$ thickness), $\text{PEO}_{15}\text{LiTFSI}$ membrane ($\varnothing = 12\text{ mm}$), LSPS pellet ($\varnothing = 12\text{ mm}$), $\text{PEO}_{15}\text{LiTFSI}$ membrane ($\varnothing = 12\text{ mm}$), Li metal electrode ($\varnothing = 10\text{ mm}$). Sufficient contacting was ensured by applying a constant pressure of 5 bar. Calendar aging tests of polymer membranes covered with LSPS powder were performed in air-tight ECC-std. cells (EL-cell GmbH). Stainless steel spacers of 0.5 mm and a hard spring (32.6 Nm) served for sufficient contacting. Individual cells for storage experiments were welded into pouch bags (Showa Denko) under argon atmosphere in order to reliably assure the absence of air intrusion even over extended times. For investigations of the interfaces after cell testing, cells were disassembled and the individual layers were separated carefully using a tweezer.

Electrochemical impedance spectroscopy (EIS).—EIS was probed in TSC battery cells (rhd instruments) with an Autolab M101 impedance analyzer (Metrohm) in a frequency range between 1 MHz and 10 mHz using an amplitude of 20 mV in the temperature range from $20\text{--}60^\circ\text{C}$. For calendar aging tests, the cells were kept at a defined temperature and EIS was measured every 12 h for 7–21 days. EIS spectra were evaluated using electrical equivalent circuits and the RelaxIS software package (rhd instruments).

X-ray photoelectron spectroscopy (XPS).—Samples were mounted floating on a stainless steel sample holder ($\varnothing = 15\text{ mm}$) using adhesive copper tape inside the glove box. The sample holder was then transferred from the glove box into the load lock of the XPS system without air exposure using a transfer vessel (Kratos). XPS spectra were recorded with an Axis Supra system (Kratos) using monochromatic Al K_α radiation ($h\nu = 1486.6\text{ eV}$) in hybrid lens mode with the instrument's charge neutralizer turned on. Sputtering was performed using an argon ion cluster gun at an acceleration voltage of 10 kV and an argon ion current of $1\text{ }\mu\text{A}$. The obtained spectra were processed and fitted using the ESCApe software (Kratos, version 1.1). Binding energies were corrected based on the C-C/C-H peak of adventitious carbon at 284.8 eV in the C 1s spectrum. A mixture of 30% Laurentzian and 70% Gaussian functions was used for the least-squares curves fitting procedure utilizing a Shirley background subtraction. For fitting of doublets, peak ratio and peak separation were fixed.

Fourier transform infrared spectroscopy (FTIR).—Samples were investigated by FTIR inside the glove box. Spectra were recorded from $4000\text{--}380\text{ cm}^{-1}$ at a MIRacle Germanium ATR (Pike Technologies) incorporated in the spectrometer Spectrum Two (Perkin Elmer).

UV-Vis spectroscopy.—Measurements were carried out at room temperature with a Lambda 35 UV-VIS Spectrometer (PerkinElmer). UV-Vis spectra were recorded in a wavelength range of $700\text{--}200\text{ nm}$, at a scan rate of $60\text{ nm}/\text{min}$, an interval of 1 nm and a slit width of 2 nm, using the program UV Winlab (PerkinElmer). Sample preparation took place in the glove box. The samples were dissolved in dimethylacetamide (anhydrous, 99.8%) or diglyme (anhydrous, 99.5%, both Sigma Aldrich Corp.) and filled into an air-tight quartz cuvette with a thickness of 1 mm.

Solid-state NMR spectroscopy.—Samples were filled into 2.5 mm ZrO_2 rotors in an argon-filled glove box. ^{31}P and ^{119}Sn magic-angle spinning (MAS) NMR experiments were carried out with a Bruker Avance 500 MHz spectrometer equipped with a 2.5 mm MAS NMR double-resonance probe at a spinning speed of 20 kHz. The magnetic field strength was 11.7 T, corresponding to Larmor frequencies of 202.4 MHz (^{31}P) and 186.4 MHz (^{119}Sn). A rotor-synchronized Hahn-echo pulse sequence was used for data acquisition with a $\pi/2$ time of 2 μs and recycle delays of 60 s.

Results and Discussion

Stability of the LSPS | $\text{PEO}_{15}\text{LiTFSI}$ interface.—In order to assess the compatibility of $\text{PEO}_{15}\text{LiTFSI}$ membranes with LSPS, we first investigated their electrochemical properties in symmetrical Li | $\text{PEO}_{15}\text{LiTFSI}$ | LSPS | $\text{PEO}_{15}\text{LiTFSI}$ | Li cells by means of EIS at different temperatures. In general, several contributions to the overall cell resistance are expected, namely from: (i) bulk and (ii) grain-boundary resistance of LSPS; (iii) bulk resistance of $\text{PEO}_{15}\text{LiTFSI}$; (iv) interfacial resistance between Li metal and $\text{PEO}_{15}\text{LiTFSI}$; (v) interfacial resistance between LSPS and $\text{PEO}_{15}\text{LiTFSI}$; and, (vi) semi-infinite diffusion in the SE sandwich layer.^{37,38}

Representative impedance spectra for the first heating and cooling cycle (ca. 3 h holding time at each temperature) are shown in Figure 1. The initial high resistance of nearly $29\text{ k}\Omega$ at 20°C is largely dominated by the contributions from the resistances (iii)–(v). The main reason for this is the poor ionic conductivity and flexibility of PEO at ambient temperature, which has been shown in various contexts before.^{39,40} To ensure sufficient contacting between PEO and Li metal, an initial conditioning step at elevated temperature is essential.³⁰ This can be linked to the phase transition of PEO from crystalline to amorphous state, which is accompanied by a decrease in viscosity and thus allows better adhesion at the interfaces.^{3,41}

As expected, EIS spectra recorded during the cool-down cycle showed remarkably lower overall cell impedances than the spectra at the same temperature during the heating cycle (e.g. 15 vs. $29\text{ k}\Omega$ at 20°C), indicating that the interfacial resistances decreased. The

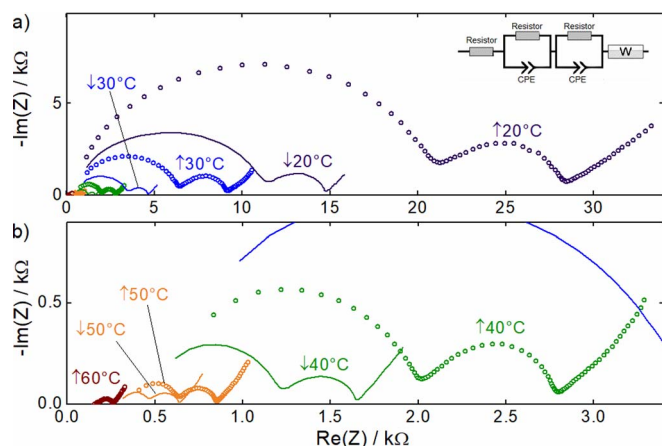


Figure 1. Nyquist diagram of the impedance of a Li | PEO₁₅LiTFSI | LSPS | PEO₁₅LiTFSI | Li cell during the first heating (circles) and the subsequent cooling (lines) cycle from 20–60°C (1 MHz to 10 MHz with 20 mV amplitude; ca. 3 h holding time at each temperature). The electric equivalent circuit used for fitting is shown in the top right.

electric equivalent circuit used to fit the experimental impedance results is shown in the top right of Figure 1. As the bulk and grain-boundary resistances of LSPS (i.e. (i) and (ii) listed above) are very small in the here measured temperature range, their contributions are expected to appear beyond the maximum applied frequency of 1 MHz.⁴² Hence, they cannot be resolved and are included in the serial resistor (s. left-most resistor in the inset of Figure 1), along with electrical resistances of the cables and the cell body. Transport through the PEO₁₅LiTFSI films and across the PEO₁₅LiTFSI | Li and the PEO₁₅LiTFSI | LSPS interfaces (contributions (iii) – (v)) appear as semicircles in the Nyquist plot and are thus modeled by a parallel circuit of a resistor and a capacitor. To account for the non-ideal capacitive behavior of solid-solid interfaces, indicated by a depression of the semicircles in Figure 1, constant phase elements (CPE) were used instead of ideal capacitors, in accordance with previous reports.^{15,43,44} The semi-infinite diffusion in the SE layer (vi), which appears as a 45° line in the low frequency region, is fitted by a Warburg diffusion element.^{37,44}

Fitting of the semicircle in the high frequency (HF) region revealed capacitances in the nF range, corresponding to a time constant on the order of milliseconds for the HF process. The middle-frequency (MF) semicircle, in contrast, showed capacitances in the μF range, corresponding to a time constant on the order of microseconds. For a clear assignment of the two processes to the contributions (iii) – (v), comparative measurements were performed with Li | PEO₁₅LiTFSI | Li and SS | PEO₁₅LiTFSI | LSPS | PEO₁₅LiTFSI | SS cells, where SS represents the stainless steel current collector. An exemplary Nyquist and Bode plot of the impedance of the three different cell configurations at 20°C is shown in Figure 2. The MF process (ascribed to the right semicircle in Figure 2a) can only be found in those cells comprising Li metal, and thus it can be assigned to the Li | PEO₁₅LiTFSI interface (iv). The capacitance on the order of μF is in good agreement with previously reported values.^{38,45} On the other hand, the HF process (ascribed to the left semicircle in Figure 2b) occurs in all cells, indicating that it is linked to Li-ion transport in the polymer layer (iii) as well as across the LSPS | PEO₁₅LiTFSI interface (v). Similar capacitances have been reported for RCPE elements describing Li-ion transport across the SE layer.^{42,44}

In order to evaluate the calendar aging of these cells, time-resolved EIS was performed at 40°C (after prior heating to 60°C). Impedance spectra recorded over the course of one week are shown in Figure 3, demonstrating a steady rise in cell impedance with time. Fitting was performed using the same equivalent circuit model as for the temperature-dependent EIS spectra (Figure 1). The resistance of the HF process was increasing slightly, while the capacitance remained

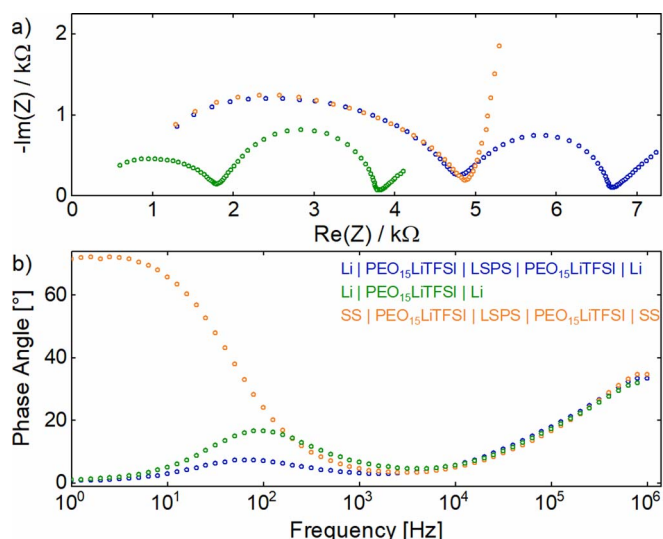


Figure 2. a) Nyquist and b) Bode diagram of the impedance of three different cell setups at 20°C prior to any heating cycle (1 MHz to 1 Hz with 20 mV amplitude): Li | PEO₁₅LiTFSI | LSPS | PEO₁₅LiTFSI | Li (blue), Li | PEO₁₅LiTFSI | Li (green) and SS | PEO₁₅LiTFSI | LSPS | PEO₁₅LiTFSI | SS (orange).

in the nF range. This might indicate an ongoing degradation process at the LSPS | PEO₁₅LiTFSI interface. In contrast, the MF process showed a strong increase in resistance with a simultaneous decrease in capacitance. This trend could arise from either contact losses or decomposition to result in electrochemically inactive species at the Li | PEO₁₅LiTFSI interface. Similar conclusions were reached in previous studies.^{30,38,45} However, a clear assignment of the impedance rise to changes in the cell is difficult as the various contributions to the cell impedance partially overlap in the EIS spectra. For a more accurate analysis of the compatibility of the two electrolytes while excluding interfering influences from Li metal, stainless steel (SS) electrodes were used for subsequent testing.

Symmetrical SS | PEO₁₅LiTFSI | LSPS | PEO₁₅LiTFSI | SS cells were built and characterized by EIS over time, likewise revealing a continuously rising cell impedance (Figure 4). Fitting required adoption of the equivalent circuit, as the resistance at the Li | PEO₁₅LiTFSI interface (process (iv)) is eliminated due to the absence of lithium. Instead, an additional constant phase element CPE3 was introduced to represent the SS | PEO₁₅LiTFSI interface (Figure 4, top left). The values for R and CPE of the HF semicircle increased linearly. As for the cells with Li metal electrodes, the time constant was determined to be in the microsecond range and can thus be assigned to the LSPS | PEO₁₅LiTFSI interface. This growing resistance at the LSPS | PEO₁₅LiTFSI interface clearly indicates chemical stability issues between LSPS and PEO₁₅LiTFSI, further supported by the intense

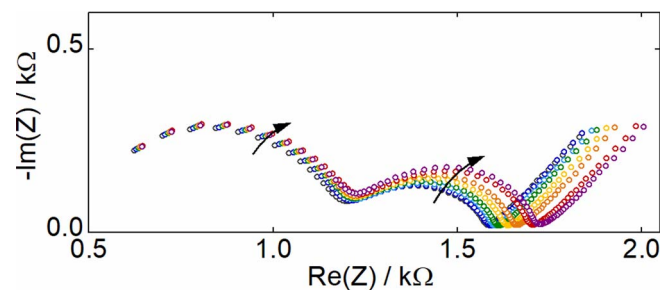


Figure 3. Nyquist diagram of the impedance of a Li | PEO₁₅LiTFSI | LSPS | PEO₁₅LiTFSI | Li cell stored at 40°C after prior heating to 60°C (1 MHz to 10 MHz with 20 mV amplitude). The arrows indicate the development over time, taken at 1-day intervals (blue: initial impedance, pink: after 7 days).

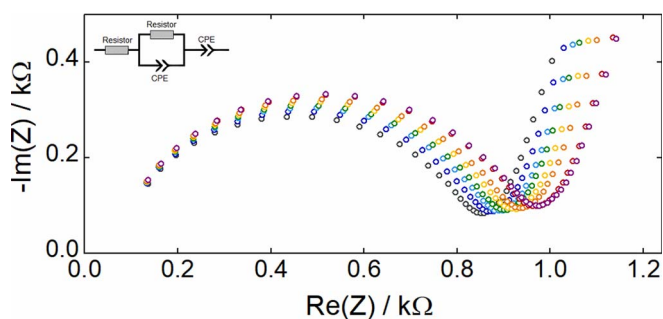


Figure 4. Nyquist diagram of the impedance of an SS | PEO₁₅LiTFSI | LSPS | PEO₁₅LiTFSI | SS cell stored at 40°C after prior heating to 60°C (1 MHz to 10 MHz with 20 mV amplitude). The arrow indicates the development over time, taken at 1-day intervals (blue: initial impedance, pink: after 7 days). The electric equivalent circuit used for fitting is shown in the top left.

yellow coloration of the PEO₁₅LiTFSI membrane seen after cell disassembly (Figure S1).

Identification of the decomposition products.—In order to identify the decomposition products between LSPS and PEO₁₅LiTFSI, the cells were disassembled and the aged interfaces were investigated. XRD pattern of the aged samples were identical to those of pristine LSPS and PEO₁₅LiTFSI, showing that the degradation products must be either amorphous or constitute very small fractions not detectable by XRD. XPS analysis, in contrast, revealed significant changes in the S 2p and P 2p spectra of the LSPS pellet surface which had been in contact with the PEO₁₅LiTFSI membrane in the cell at 60°C over appx. 7 days (Figure 5). We will first focus on the chemical environment of the sulfur atoms. An adequate fit of the S 2p detail spectra required modeling the signal with five doublets. The main signal at 168.9 eV (S 2p_{3/2}; note that doublet binding energies are always referenced here to the lower binding energy peak of a doublet) marked by the gray areas in Figure 5a represents the sulfur in [SO₂-CF₃] units of LiTFSI, as shown by Xu et al.³⁰ The signal at 161.2 eV (marked in green), corresponding to the lowest oxidation state of sulfur, originates from the terminal sulfur in PS₄³⁻ and SnS₄⁴⁻ units of LSPS. Similar binding energies were already reported for LSPS as well as its derivate LGPS.^{36,43}

The remaining three S 2p doublets could not be assigned to the pure compounds. Comparison to literature data indicates that the peak at 167.0 eV (marked in red) derives from oxygen-bound sulfur, as reported for sulfites.^{43,46} The signal at 163.3 eV (marked in yellow), which originates from sulfur in a lower oxidation state, most likely corresponds to the bridging sulfur atoms of polysulfide species: bridging sulfur atoms (S⁰) are usually reported at S 2p_{3/2} binding energies of 163.1–163.9 eV, while terminal sulfur atoms (S⁻) usually appear in the range of 161.7–162.3 eV.^{46–49} It should be mentioned that the signal ratio as well as their exact binding energy depends on the polysulfide chain lengths, which however, cannot be quantified with certainty due to a strong overlap with the signals resulting from the bulk LSPS phase.

An adequate fit of the P 2p signal required two binding states to be considered. In accordance with Zhang et al., the main signal at 132.0 eV (P 2p_{3/2}) marked by the green area in Figure 5b was assigned to phosphorus in a tetrahedral coordination with sulfur, namely to the PS₄³⁻ units in LSPS.⁴³ A second signal at 132.9 eV (marked in blue) might originate from P-[S]_n-P type bonding configurations, e.g. represented by a P₂S₇⁴⁻ unit, with the corresponding S 2p_{3/2} signal appearing at 162.9 eV.^{43,49} A similar binding energy was reported for P-S-P bonds in P₂S₅ in a different study, also matching the S 2p_{3/2} doublets detected at 162.1 eV and 163.5 eV.⁵⁰ Note that due to smaller signal intensities in the P 2p region and a significant overlap of the doublets, quantification of the two components involves a high degree of uncertainty.

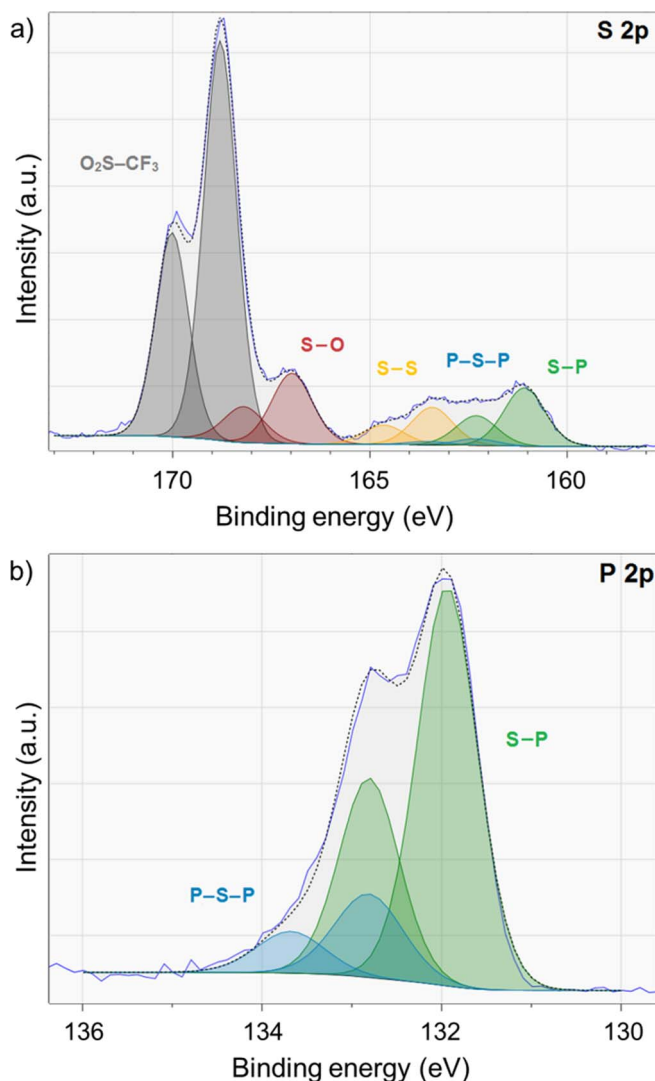


Figure 5. a) XPS S 2p and b) XPS P 2p spectra of the LSPS surface which was at the interface between LSPS and PEO₁₅LiTFSI after aging in an SS | PEO₁₅LiTFSI | LSPS | PEO₁₅LiTFSI | SS cell at 60°C over appx. 7 days. Grey peaks are attributed to the [SO₂-CF₃] unit in LiTFSI (168.9 eV), red peaks to S-O bonds in sulfite (167.0 eV), yellow peaks to S-S bonds in polysulfides (163.3 eV), blue peaks to P-[S]_n-P type bonds (162.9 eV for the P 2p and 132.9 eV for the S 2p signals), and green peaks to PS₄³⁻ or SnS₄⁴⁻ bonds in LSPS (161.2 eV for the P 2p and 132.0 eV for the S 2p signals). Note that doublet binding energies are always referenced here to the lower binding energy peak of a doublet.

Figure 6 depicts the FTIR spectra of an aged (60°C over appx. 7 days) PEO₁₅LiTFSI | LSPS sample in comparison to the pristine materials. The shoulders emerging at 1030 and 1420 cm⁻¹ can be attributed to S=O vibrations (marked by red stars), as shown by Hesse et al.⁵¹ S-S stretching vibrations in polysulfides (marked by the yellow star) usually yield weak bands around 500 cm⁻¹.⁵² However, due to the strong overlap with S-P and S-Sn bands in LSPS, which appear around 400 and 570 cm⁻¹, an unambiguous confirmation of polysulfides is not possible. Strong bands at 635, 905 and 1615 cm⁻¹ (green stars) match the values reported for C=C-H stretching vibrations.^{51,53} This indicates a reduction of the polymer accompanied by hydrogen or water release, which will be discussed later.

In order to confirm the development of polysulfides during aging of LSPS with PEO as suggested by XPS analysis (Figure 5a), UV-Vis spectroscopy based studies showed that the detected S_n²⁻ species thereby depends on the properties of the solvent.^{54–56} In solvents with

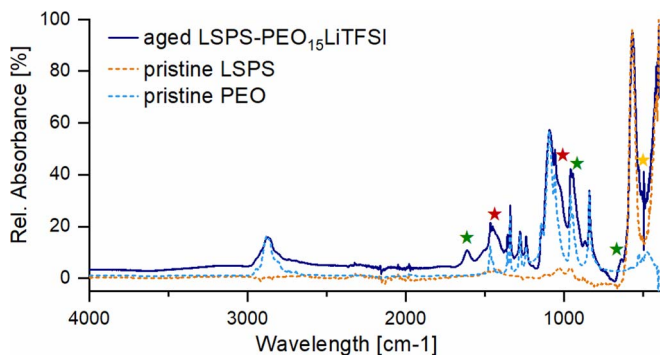


Figure 6. FTIR spectra of the aged LSPS | PEO₁₅LiTFSI interface (solid blue line) aged at 60°C over approx. 7 days compared to pristine LSPS (dashed orange line) and pristine PEO (dashed light blue line). Vibrations bands of S–S (yellow star), S=O (red stars) and C=C–H bonds (green stars) are indicated for better visibility.

a high donor number, e.g. dimethyl sulfoxide or dimethylacetamide (DMA), multiple redox reactions involving S_8^{2-} , S_6^{2-} , S_4^{2-} and $S_3^{•-}$ species take place, with the strongly blue-colored $S_3^{•-}$ radical being the predominantly stabilized intermediate. In contrast, low donor number solvents such as 1,3-dioxolane or diglyme promote the formation of short-chain polysulfides, mostly the yellow-colored S_4^{2-} anion. To determine whether polysulfides were produced during the aging of the PEO₁₅LiTFSI | LSPS interface at 60°C over 7 days, the aged PEO₁₅LiTFSI membranes were rinsed in DMA and diglyme, respectively. The DMA solution immediately turned blue while the yellow coloration of the polymer disappeared, indicating the presence of the blue $S_3^{•-}$ radical expected upon the solvation of polysulfides in DMA. With diglyme instead, the membrane had to be dissolved to obtain a yellow solution indicating short-chain polysulfides. Thus, the coloration of the solutions was a first indication for polysulfide species in the aged PEO₁₅LiTFSI membrane, and several features characteristic of polysulfides were observed in the UV-Vis spectra of the solutions obtained with both solvents (Figure 7). As discussed above, the different donor properties of diglyme and DMA result in the stabilization of different polysulfide species. In diglyme, the UV-Vis features can be attributed to S_2^{2-} (280 nm) and S_4^{2-} (345 and 420 nm), whereas S_6^{2-} (338 and 448 nm) and $S_3^{•-}$ (618 nm) were detected in DMA.^{55,57} In summary, the expected speciation of polysulfides in the two solvents is an unambiguous proof of the formation of polysulfides in the PEO₁₅LiTFSI membrane during the aging of the PEO₁₅LiTFSI | LSPS interface at 60°C. The existence of polysulfides in the aged PEO₁₅LiTFSI membrane was also confirmed by Raman spectroscopy (not shown).

For further analysis, magic-angle-spinning (MAS) nuclear magnetic resonance (NMR) spectroscopy was performed on fresh LSPS and LSPS aged at 60°C over approx. 7 days in an SS | PEO₁₅LiTFSI | LSPS | PEO₁₅LiTFSI | SS cell.³¹ ³¹P MAS NMR spectra of the fresh LSPS (Figure 8a, red line) revealed two strong peaks at 92.6 ppm and 77.9 ppm, which represent isolated $[PS_4]^{3-}$ units and can be assigned to the 2a (occupied exclusively by P) and 4d sites (occupied by Sn and P in a ratio of 1:1) in the LSPS phase.³⁵ Another peak is visible at 86.8 ppm, which is consistent with the presence of a small amount (15%) of either Li₇PS₆ or Li₃PS₄. To clearly distinguish between the two, XRD analysis was performed. Rietveld refinement revealed 7.94% Li₇PS₆ as the only side phase in pristine LSPS (Figure S2). This argyrodite, which can be described as a double salt of PS_4^{3-} and S^{2-} anions,⁵⁸ has recently been reported as a side phase of LSPS by Kaus et al.³⁵ In addition, a small and rather broad ³¹P MAS NMR peak is visible at 68 ppm in Figure 8a, which hints at the presence of P-rich amorphous regions (1%), and a small peak at 10 ppm reveals the presence of a minor Li₃PO₄ contribution (0.3%). The NMR spectrum of the aged LSPS (blue line) looks very similar to that of the fresh sample. The only clear difference is a broadening of the peak at

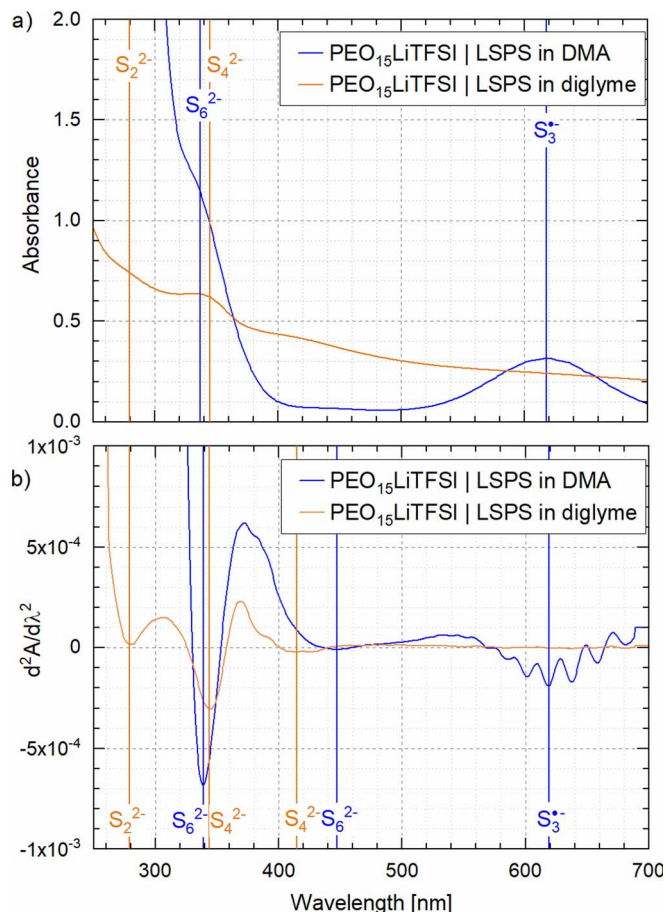


Figure 7. a) UV-Vis spectra of aged PEO₁₅LiTFSI membranes which were soaked in either DMA (blue) and diglyme (orange); membranes were aged at 60°C over approx. 7 days in an SS | PEO₁₅LiTFSI | LSPS | PEO₁₅LiTFSI | SS cell. b) 2nd derivative of the absorbance to better detect the various spectral contributions: S_2^{2-} at 280 nm, S_4^{2-} at 345 and 420 nm, S_6^{2-} at 338 and 448 nm, $S_3^{•-}$ at 618 nm.

86.8 ppm, which shows that the impurity phase undergoes an amorphization during aging. However, no conclusion with regard to the P–S–P type bonds suggested by XPS analysis (blue marked peaks in Figure 5b) can be drawn, as the expected signal would overlap with those of Li₇PS₆ or Li₃PS₄.⁵⁹

The ¹¹⁹Sn MAS NMR spectra (Figure 8b) are again very similar for the fresh and the aged LSPS. A single peak at 87 ppm can be assigned to the $[SnS_4]^{4-}$ units in the LSPS phase.³⁵ The asymmetry of this peak might hint at some Sn–P exchange between the 2a and 4d sites. A slight broadening of this peak for the aged sample (blue line) might result from some increased structural disordering of the main phase. As in the ³¹P MAS NMR spectra, no additional phases can be evidenced.

Potential reasons for the decomposition of LSPS at the LSPS | PEO₁₅LiTFSI interface.—Polysulfides S_n^{2-} , sulfite SO_3^{2-} and P–[S]_n–P type bridged PS_4^{3-} units were identified as decomposition products in the previous section, without, however, discussion their possible origin. Within this part, conceivable reasons for the observed degradation products are reviewed. Before looking into contaminations and structural features of the two materials, the influence of temperature on decomposition was investigated. Therefore, calendar aging of SS | PEO₁₅LiTFSI | LSPS | PEO₁₅LiTFSI | SS cells and SS | PEO₁₅LiTFSI | LSPS | SS cells using LSPS powder was performed at 20, 40 and 60°C. Cell disassembly demonstrated the degradation enhancing effect of temperature, as samples stored at 60°C showed

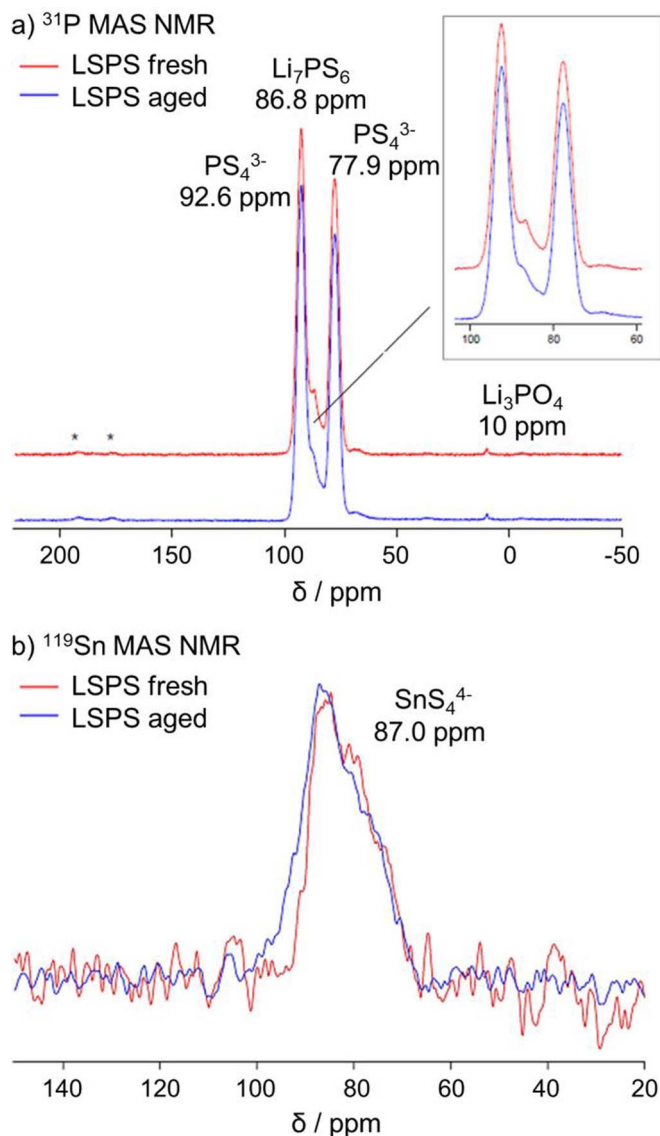


Figure 8. a) ^{31}P MAS NMR spectra of fresh (red) and aged (blue) LSPS. Peaks can be attributed to two isolated $[\text{PS}_4]^{3-}$ units in LSPS, a Li_7PS_6 contamination, and a small fraction of Li_3PO_4 . Comparison of the fresh and aged sample indicates a slight amorphization of the side phases in the aged sample. Spinning sidebands are marked with an asterisk. b) ^{119}Sn MAS NMR spectra of fresh (red) and aged (blue) LSPS. The peak can be assigned to $[\text{SnS}_4]^{4-}$ units in LSPS.

more intense coloration than those stored at 20°C. This observation was supported by XPS analysis, which yielded a higher fraction of degradation products for the samples stored at 60°C. Hence, the decomposition reaction seems to be kinetically controlled.

One conceivable origin of the observed degradation is a reaction of LSPS with traces of water in the system. PEO is known to trap water even throughout vacuum drying, and Karl-Fischer titration as well as FTIR spectroscopy were reported as suitable methods to explore this.^{30,60} However, both measurements, conducted with the pure materials and the hot-pressed $\text{PEO}_{15}\text{LiTFSI}$ membranes, did not indicate any residual water. An alternative source of moisture could originate from leakage of the test cells. To fully exclude any possibility of moisture intrusion, several test cells were stored in argon-filled pouch bags sealed in the glove box. XPS analysis conducted after storage for one week at 60°C revealed the same degradation products for cells with and without additional sealing in pouch bags, so that leakage of ambient air into the cell could be ruled out as an origin of

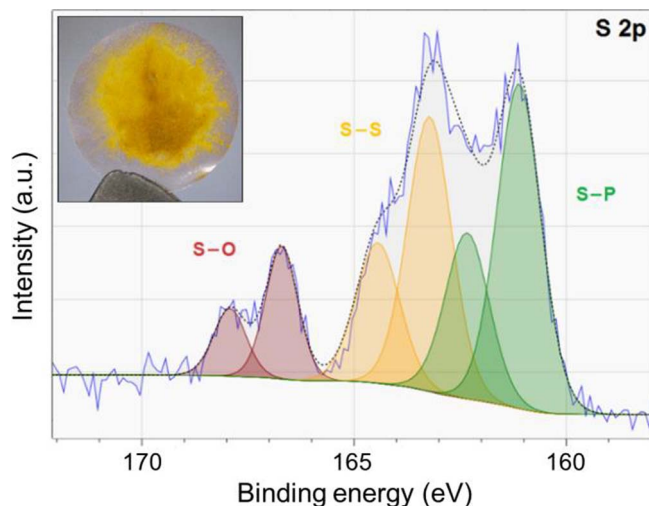


Figure 9. Image (top left) and XPS S 2p spectra of a PEO membrane after aging in an SS | PEO | LSPS | SS cells using LSPS powder at 60°C over approx. 7 days. Red peaks are attributed to S–O bonds in sulfite (166.9 eV), yellow peaks to S–S bonds in polysulfides (163.4 eV) and green peaks to PS_4^{3-} or SnS_4^{4-} bonds in LSPS (161.2 eV).

the decomposition. As a further test to exclude residual moisture or ambient air intrusion into the cell as the cause for the here observed LSPS, the reaction products of LSPS with water were examined. For this, a cell containing LSPS powder was purged with humidified argon that was saturated with water at 25°C. Subsequent XPS and FTIR analysis revealed Li_2S , LiOH , elementary tin as well as reduced phosphorus species as the reaction products, next to only minor amounts of SO_x compounds (Figure S3). Apparently, reaction with water results in a reduction of LSPS, whereas only oxidized species were found in the LSPS- $\text{PEO}_{15}\text{LiTFSI}$ samples aged at 60°C in SS | $\text{PEO}_{15}\text{LiTFSI}$ | LSPS | SS cells, and XPS as well as UV-Vis spectroscopy of the former confirmed the same degradation products. This ultimately refutes the possibility that the reaction of LSPS with trace water impurities might be the origin of the observed decomposition.

In the next step, LiTFSI as the conductive salt was investigated. To exclude a possible reaction between LiTFSI and LSPS, PEO membranes without salt were prepared and stored in SS | PEO | LSPS | SS cells using LSPS powder. Cell disassembly after calendar aging for 7 days at 60°C revealed an intense yellow coloring, as observed for the LSPS- $\text{PEO}_{15}\text{LiTFSI}$ samples stored for 7 days in SS | $\text{PEO}_{15}\text{LiTFSI}$ | LSPS | SS cells, and XPS as well as UV-Vis spectroscopy of the former confirmed the same degradation products. The XPS S 2p spectrum is shown in Figure 9 together with an image of the aged salt-free PEO membrane, which is essentially identical with that shown in Figure 5 for the aged SS | $\text{PEO}_{15}\text{LiTFSI}$ | LSPS | $\text{PEO}_{15}\text{LiTFSI}$ | SS cell, except for the absence of the LiTFSI features at 168.9 eV. These results do not only prove that the conductive salt is not required for the observed LSPS decomposition, but also demonstrate that all the sulfur-containing reaction products stem from the oxidative decomposition of LSPS. This was particularly surprising with regard to the sulfite species, which we considered to originate from LiTFSI before.

Since Blanga et al. did not report stability issues for their composite electrolyte based on PEO and LSPS,³⁶ one could question whether contaminants in the pristine materials cause the decomposition. Beside the Li_7PS_6 phase identified by ^{31}P -NMR, XPS analysis of the raw materials indicated lithium hydroxide and carbonate as contaminants in LSPS (Figure S4). The assignment of the O 1s peak to LiOH was confirmed by comparative measurements of an LSPS-LiOH pellets (wt ratio 2:1), yielding an O 1s signal at exactly the same binding energy. The pellets were moreover stored at 60°C for two weeks and analyzed via XPS. As no changes were observed in the spectra, LSPS and LiOH were proven to not react with each other (shown for the S 2p spectrum in Figure S5). The LiOH impurity though might react with PEO and thereby might lead to the observed degradation of LSPS.

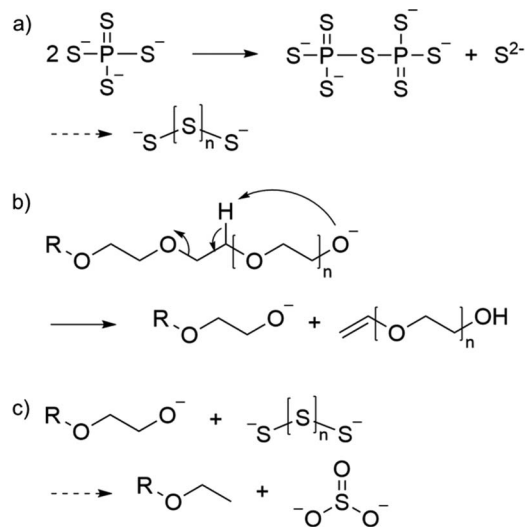
To probe this, an SS | LSPS-LiOH | PEO | SS cell was stored for appx. 7 days at 60°C. Subsequent XPS analysis revealed a remarkably higher sulfite amount than in SS | LSPS | PEO | SS cells (Figure 9), and even traces of sulfate were detected (Figure S6). The same observation was made for SS | LSPS | PEO | SS cells aged for an extended time of appx. 6 weeks. Apparently, LiOH has a promoting effect on sulfite formation, indicating that it plays a role in the degradation mechanism.

In order to explain a reactivity of PEO with LSPS, we also took a closer look at the functional groups of the polymer. The here used PEO with an average molecular weight of 10^6 g·mol⁻¹ only features hydroxyl groups at the chain ends, from which a nominal hydroxyl mass fraction of 0.034 mg·g⁻¹ can be calculated.⁶¹ Despite this small value, a reactivity of these hydroxyl groups cannot be generally excluded. Their impact on the degradation reaction can be examined by replacing PEO by a similar polymer without hydroxyl groups. Polyethylene glycol dimethyl ether (PEGDME), which differs from PEO by having methoxy end groups, was selected to be tested against LSPS powder. XPS analysis after calendar aging of an SS | PEGDME | LSPS | SS cell for appx. 7 days at 60°C likewise yielded polysulfides, which was additionally verified by UV-Vis spectroscopy. In contrast to previous XPS experiments with aged LSPS-PEO samples (e.g. Figure 9), however, no S–O species were detected in the S 2p spectrum (Figure S7). Apparently, removal of the hydroxyl functionality prevents sulfite formation, while the appearance of polysulfides is not affected by the presence/absence of hydroxyl functionalities. It seems that two different decomposition processes take place simultaneously at the LSPS | PEO interface. The tests with PEGDME revealed that sulfite formation is most likely caused by a reaction of LSPS with the hydroxyl groups of PEO and, with regard to the previous experiment, promoted by LiOH contaminations in pristine LSPS.

Discussion of a possible degradation mechanism.—Based on the above findings, the reactants involved in the decomposition reaction of LSPS and PEO are PEO itself, the PS₄³⁻ units of LSPS and possibly LiOH impurities in LSPS. The resulting degradation products are polysulfides S_n²⁻, sulfite SO₃²⁻ and P–[S]_n–P type bridged PS₄³⁻ units. As mentioned, comparative measurements indicated two degradation mechanisms. The hydroxyl groups in PEO and the LiOH contaminant in LSPS turned out to be involved in the oxidation of LSPS to sulfite, but polysulfides and P–[S]_n–P units were also found in aged LSPS-PEGDME samples.

To the best of our knowledge, fundamental investigations of the chemical stability between organic polymers and sulfide-based inorganic SEs have not been conducted without applying electrochemistry so far. A literature research though revealed that the same degradation products were found in XPS studies of sulfide-based SEs in contact with cathode active materials in ASSBs after cycling.^{12,43,48–50} Auvergniot et al., for instance, reported the formation of polysulfides, P₂S₅ and LiCl during oxidation of Li₄PS₅Cl in contact with LiCoO₂.⁵⁰ They moreover detected sulfite, which was attributed to the reaction of the argyrodite with traces of oxygen in the cell. Zhang et al. analyzed the interfacial properties of an LGPS/LiCoO₂/carbon composite cathode, identifying S–O, S–S, P=S and P–S–P type bonds formed during cycling.⁴³ Similar observations were made by Koerver et al., who found S–S and P–[S]_n–P species in a composite cathode based on LiNi_{0.8}Co_{0.1}Mn_{0.1}O₂ (NMC) and β-Li₃PS₄ (LPS) after cycling.^{48,49}

To better understand the connection between these oxidation reactions provoked by galvanostatic cycling and the oxidation processes herein, we took a deeper look into the underlying mechanisms. The formation of P–[S]_n–P bridges (n ≥ 2) in a polymerization-like reaction of PS₄³⁻ units was predicted in computational studies on the LPS/FePO₄ interface by Sumita et al.^{62,63} The reaction is accompanied by a decrease in Li-ion sites, and Li-ion diffusion into the cathode is a driver for further oxidation. In a follow up experimental study, the behavior of LPS/carbon cathodes during Li deinsertion and insertion was examined.⁶⁴ Hakari et al. showed that the sulfide ions in LPS contribute to charge compensations. By XPS analysis it was demonstrated that the local bonding environment of phosphorus remained unchanged, but higher oxidation states were observed in S 2p spectra



Scheme 1. Reaction scheme for a possible degradation mechanism of LSPS. (a) Reaction of PS₄³⁻ units to P₂S₇⁴⁻ units and polysulfides, analogous to what was proposed by Koerver et al.⁴⁹ (b) Intramolecular fragmentation of deprotonated PEO, according to Hester et al.⁶⁹ (c) Reaction of the alkoxides produced by reaction (b) with polysulfides produced by reaction (a) to sulfite and polymer fragments, inspired by Liang et al.⁴⁷

of charged cathodes. The signal at 162.7 eV was assigned to bridging sulfur atoms between PS₄³⁻ units, which results in a formal sulfur oxidation state of –1.

A similar reaction has recently been reported by Koerver et al., who also observed interconnection of PS₄³⁻ units upon oxidation of an LPS/NMC/carbon composite.⁴⁹ They presumed formation of corner- and edge-sharing species, namely Li₄P₂S₈, Li₄P₂S₇ or Li₂P₂S₆. In contrast to the polymerization proposed by Sumita et al., this reaction is not only accompanied by reduction of Li-ion sites, but also by sulfur release, resulting in a nominal loss of Li₂S (Scheme 1a). They stated that during the charging process sulfur might be accumulated in the cathode and Li-ions are transferred to the counter electrode.^{49,64} According to various studies, the released sulfur most likely reacts with sulfide ions, which are e.g. present in the Li₇PS₆ side phase, to form polysulfides.^{43,48–50}

Interestingly, Koerver et al. found the same oxidation products, albeit less intense, by XPS analysis of the LPS/carbon mixtures prior to electrochemical testing.⁴⁹ This was not further commented, however regarding the results presented in our study, we suggest that cycling only accelerates the oxidation, but is not the actual trigger. Li extraction toward the counter electrode cannot be the driving force in this case, as the material was not exposed to a current or a potential. The same is true for the calendar aging tests shown here, suggesting that the LSPS decomposition mechanism involves a reaction with the PEO. Firstly, PEO is well-known to have a high Li-ion solvation ability, owing to its crown-ether-like structure that allows efficient complexation of Li-ions.^{3,40,65} Furthermore, several studies in the field of Li/S battery research demonstrated that polysulfides can be dissolved in PEO, showing high mobility in Li/S cells with SPEs.^{66–68} It can therefore be assumed that removal of the LSPS decomposition products, i.e., of Li-ions and polysulfides, into the polymer is a driving force for the oxidation of LSPS, following the principle of Le Chatelier.

The FTIR results moreover indicated that the polymer gets reduced, resulting in formation of C=C double bonds. Hester et al. reported various fragmentation reactions for deprotonated PEO.⁶⁹ LiOH being present in pristine LSPS might act as a deprotonation agent. The formation of alkoxides has already been reported for the reaction of PEO with different alkali metal hydroxides by Xiao et al.⁷⁰ In a subsequent intramolecular ether cleavage reaction, smaller fragments could emerge (Scheme 1b).⁷¹ The fragmentation of PEO leads to a much higher amount of terminal oxygen than in the pristine material, which

becomes relevant concerning sulfite formation. In search of a reaction mechanism, we found an interesting correlation with Li/S batteries. Liang et al. showed that graphene oxide is reduced in contact with polysulfides.⁴⁷ More precisely, they stated that C-OH bonds get reduced to C-H bonds during oxidation of polysulfides to thiosulfate. The formation of thiosulfate by oxidation of sulfur with metal hydroxide has also been reported earlier.⁷²

In summary, a plausible degradation mechanism for LSPS could start with the polymerization of PS_4^{3-} units. The released sulfur can react to polysulfides which are, likewise Li-ions, taken up by PEO. At the same time, the polymer could undergo an intramolecular fragmentation, which is accelerated by deprotonation of PEO with LiOH. The resulting alkoxides might then react with polysulfides to form sulfite and polymer fragments (Scheme 1c). This mechanism would also explain the absence of sulfite species in LSPS-PEGDME samples, as the lack of a terminal hydroxyl group prohibits both the initial deprotonation and the subsequent intramolecular fragmentation to alkoxides.

Conclusions



In the present study, we analyzed the compatibility of the inorganic solid electrolyte LSPS with PEO-based polymer membranes. First electrochemical investigations in a Li | $\text{PEO}_{15}\text{LiTFSI}$ | LSPS | $\text{PEO}_{15}\text{LiTFSI}$ | Li cell demonstrated a continuous increase in the overall cell resistance, clearly indicating an ongoing degradation reaction of the LSPS solid electrolyte. SS | $\text{PEO}_{15}\text{LiTFSI}$ | LSPS | $\text{PEO}_{15}\text{LiTFSI}$ | SS cells where the lithium electrodes were replaced by stainless steel blocking electrodes showed an analogous impedance increase which could be ascribed to a growing impedance at the LSPS | $\text{PEO}_{15}\text{LiTFSI}$ interface caused by a reaction between these two materials. Subsequent XPS analysis, ^{31}P MAS NMR, and UV-Vis spectroscopic tests of the aged LSPS | $\text{PEO}_{15}\text{LiTFSI}$ interface revealed polysulfides, P-[S]_n-P type bridged PS_4^{3-} units and sulfite as decomposition products. Additional experiments showed that artifacts due to reaction of LSPS with trace water impurities as well as the reaction of LSPS with the conductive salt LiTFSI could be ruled out as possible causes for the observed LSPS degradation. On the other hand, surface impurities on pristine LSPS as well as the hydroxyl end groups in PEO were found to affect the LSPS decomposition: while comparative tests showed that polysulfides are evolved independently of whether the end groups of the polymer were hydroxyl (in PEO) or methoxyl (in PEGDME) moieties sulfite is only formed in the presence of hydroxyl end groups (i.e. with PEO). Our data clearly prove that the LSPS | PEO interface is chemically instable, even in the absence of any electrochemistry. Based on a literature review, we proposed a plausible reaction mechanism for the purely chemical degradation of LSPS at the LSPS | PEO interface, considering not only the raw materials LSPS and PEO, but also contaminants such as lithium hydroxide on the LSPS surface.

We hereby want to highlight the importance of investigating interfaces in ASSBs both in terms of electrochemical and chemical properties. Regarding surface impurities and evaluating their role in potential unwanted side reactions is indispensable when analyzing electrochemical properties at the material level. Although surface impurities like lithium hydroxide or carbonate can be found in all types of battery materials, they are rarely taken into account when it comes to interpretation of the experimental data. This work shows that extensive post-mortem analysis is essential to get a complete picture of the interfacial reactions taking place in ASSBs.

Acknowledgment

The authors thank the BMW AG for the financial support of this work. Simon Qian, Qi He and Michele Piana from the Chair of Technical Electrochemistry (TEC) of the Technische Universität München are greatly acknowledged for their support with the UV-Vis measurements and the purging experiments with humidified argon, respectively.

ORCID

Nathalie Riphaut  <https://orcid.org/0000-0001-5860-1106>
 Sylvio Indris  <https://orcid.org/0000-0002-5100-113X>
 Stefan J. Sedlmaier  <https://orcid.org/0000-0002-5337-3076>

References

- J. Janek and W. G. Zeier, *Nat. Energy*, **1**(9), 16141 (2016).
- F. Mizuno, C. Yada, and H. Iba, in *Lithium-Ion Batteries*, p. 273, Elsevier B.V. 2014.
- A. Varzi, R. Raccichini, S. Passerini, and B. Scrosati, *J. Mater. Chem. A*, **4**(44), 17251 (2016).
- D. Andre, H. Hain, P. Lamp, F. Maglia, and B. Stiaszny, *J. Mater. Chem. A*, **5**(33), 17174 (2017).
- W. Weppner, in *Encyclopedia of Electrochemical Power Sources*, p. 162, Elsevier B.V. 2009.
- Y. Seino, T. Ota, K. Takada, A. Hayashi, and M. Tatsumisago, *Energy Environ. Sci.*, **7**(2), 627 (2014).
- P. Bron, S. Johansson, K. Zick, Schmedt auf der Günne, Jörn. S. Dehnen, and B. Roling, *J. Am. Chem. Soc.*, **135**(42), 15694 (2013).
- Y. Kato, S. Hori, T. Saito, K. Suzuki, M. Hirayama, A. Mitsui, M. Yonemura, H. Iba, and R. Kanno, *Nat. Energy*, **1**(4), 16030 (2016).
- N. Kamaya, K. Homma, Y. Yamakawa, M. Hirayama, R. Kanno, M. Yonemura, T. Kamiyama, Y. Kato, S. Hama, K. Kawamoto, and A. Mitsui, *Nat. Mater.*, **10**(9), 682 (2011).
- C. Cao, Z.-B. Li, X.-L. Wang, X.-B. Zhao, and W.-Q. Han, *Front. Energy Res.*, **2**(Part 1), 947 (2014).
- J. B. Goodenough and P. Singh, *J. Electrochem. Soc.*, **162**(14), A2387 (2015).
- F. Han, T. Gao, Y. Zhu, K. J. Gaskell, and C. Wang, *Adv. Mater.*, **27**(23), 3473 (2015).
- W. D. Richards, L. J. Miara, Y. Wang, J. C. Kim, and G. Ceder, *Chem. Mater.*, **28**(1), 266 (2016).
- S. Wenzel, D. A. Weber, T. Leichtweiss, M. R. Busche, J. Sann, and J. Janek, *Solid State Ionics*, **286**, 24 (2016).
- S. Wenzel, S. Randau, T. Leichtweiss, D. A. Weber, J. Sann, W. G. Zeier, and J. Janek, *Chem. Mater.*, **28**(7), 2400 (2016).
- Y. Zhu, X. He, and Y. Mo, *ACS Appl. Mater. Interfaces*, **7**(42), 23685 (2015).
- C. Yada, C. E. Lee, D. Laughman, L. Hannah, H. Iba, and B. E. Hayden, *J. Electrochem. Soc.*, **162**(4), A722 (2015).
- K.-I. Chung, W.-S. Kim, and Y.-K. Choi, *J. Electroanal. Chem.*, **566**(2), 263 (2004).
- M. Ogawa, R. Kanda, K. Yoshida, T. Uemura, and K. Harada, *J. Power Sources*, **205**, 487 (2012).
- K. Nagao, A. Hayashi, M. Deguchi, H. Tsukasaki, S. Mori, and M. Tatsumisago, *J. Power Sources*, **348**, 1 (2017).
- A. Kato, A. Hayashi, and M. Tatsumisago, *J. Power Sources*, **309**, 27 (2016).
- M. Nagao, A. Hayashi, and M. Tatsumisago, *Electrochemistry*, **80**(10), 734 (2012).
- B. Son, J. G. Kim, S. Mukherjee, N. Schuppert, A. Bates, O. Kwon, M. J. Choi, H. Y. Chung, and S. Park, *J. Power Sources*, **282**, 299 (2015).
- B. Zhu, Y. Jin, X. Hu, Q. Zheng, S. Zhang, Q. Wang, and J. Zhu, *Adv. Mater.*, **29**(2), (2017).
- S. M. Choi, I. S. Kang, Y.-K. Sun, J.-H. Song, S.-M. Chung, and D.-W. Kim, *J. Power Sources*, **244**, 363 (2013).
- T. Zhang, N. Imanishi, S. Hasegawa, A. Hirano, J. Xie, Y. Takeda, O. Yamamoto, and N. Sammes, *J. Electrochem. Soc.*, **155**(12), A965 (2008).
- T. Shodai, *J. Electrochem. Soc.*, **141**(10), 2611 (1994).
- H. H. Sumathipala, J. Hassoun, S. Panero, and B. Scrosati, *J. Appl. Electrochem.*, **38**(1), 39 (2007).
- Y.-C. Jung, M.-S. Park, D.-H. Kim, M. Ue, A. Eftekhari, and D.-W. Kim, *Sci. Rep.*, **7**(1), 17482 (2017).
- C. Xu, B. Sun, T. Gustafsson, K. Edström, D. Brandell, and M. Hahlin, *J. Mater. Chem. A*, **2**(20), 7256 (2014).
- S.-D. Lee, K.-N. Jung, H. Kim, H.-S. Shin, S.-W. Song, M.-S. Park, and J.-W. Lee, *ChemSusChem*, **10**(10), 2175 (2017).
- W. Zhou, S. Wang, Y. Li, S. Xin, A. Manthiram, and J. B. Goodenough, *J. Am. Ceram. Soc.*, **138**(30), 9385 (2016).
- W. Zhou, Y. Li, S. Xin, and J. B. Goodenough, *ACS Cent. Sci.*, **3**(1), 52 (2017).
- W. E. Tenhaeff, X. Yu, K. Hong, K. A. Perry, and N. J. Dudney, *J. Electrochem. Soc.*, **158**(10), A1143 (2011).
- M. Kaus, H. Stöffer, M. Yavuz, T. Zinkevich, M. Knapp, H. Ehrenberg, and S. Indris, *J. Phys. Chem. C*, **121**(42), 23370 (2017).
- R. Blanga, M. Goor, L. Burstein, Y. Rosenberg, A. Gladkikh, D. Logvinuk, I. Shechtman, and D. Golodnitsky, *J. Solid State Electrochem.*, **20**(12), 3393 (2016).
- T. Abe, M. Ohtsuka, F. Sagane, Y. Iriyama, and Z. Ogumi, *J. Electrochem. Soc.*, **151**(11), A1950 (2004).
- G. B. Appetecchi, S. Scaccia, and S. Passerini, *J. Electrochem. Soc.*, **147**(12), 4448 (2000).
- E. Quartarone and P. Mustarelli, *Chem. Soc. Rev.*, **40**(5), 2525 (2011).
- Z. Xue, D. He, and X. Xie, *J. Mater. Chem. A*, **3**(38), 19218 (2015).
- F. M. Gray, *Solid Polymer Electrolytes: Fundamentals and Technological Applications: Solid Polymer Electrolytes: Fundamentals and Technological Applications*, Wiley-VCH, Weinheim 1991.
- P. Bron, S. Dehnen, and B. Roling, *J. Power Sources*, **329**, 530 (2016).

43. W. Zhang, T. Leichtweiss, S. P. Culver, R. Koerver, D. Das, D. A. Weber, W. G. Zeier, and J. Janek, *ACS Appl. Mater. Interfaces*, 2017.
44. P. Schichtel, M. Geiß, T. Leichtweiss, J. Sann, D. A. Weber, and J. Janek, *J. Power Sources*, **360**, 593 (2017).
45. I. Ismail, A. Noda, A. Nishimoto, and M. Watanabe, *Electrochim. Acta*, **46**(10–11), 1595 (2001).
46. M. Fantauzzi, B. Elsener, D. Atzei, A. Rigoldi, and A. Rossi, *RSC Adv.*, **5**(93), 75953 (2015).
47. X. Liang, C. Hart, Q. Pang, A. Garsuch, T. Weiss, and L. F. Nazar, *Nat. Comm.*, **6**, 5682 (2015).
48. R. Koerver, I. Aygün, T. Leichtweiss, C. Dietrich, W. Zhang, J. O. Binder, P. Hartmann, W. G. Zeier, and J. Janek, *Chem. Mater.*, **29**(13), 5574 (2017).
49. R. Koerver, F. Walther, I. Aygün, J. Sann, C. Dietrich, W. Zeier, and J. Janek, *J. Mater. Chem. A*, (5), 22750 (2017).
50. J. Auvergniot, A. Cassel, D. Foix, V. Viallet, V. Seznec, and R. Dedryvère, *Solid State Ionics*, **300**, 78 (2017).
51. M. Hesse, H. Meier, and B. Zeeh, *Spektroskopische Methoden in der organischen Chemie*, Stuttgart etc., G. Thieme 2005.
52. C. N. R. Rao, R. Venkataraghavan, and T. R. Kasturi, *Can. J. Chem.*, **42**(1), 36 (1964).
53. B. C. Smith, *Infrared Spectral Interpretation: A Systematic Approach*, Taylor & Francis 1998.
54. Y.-C. Lu, Q. He, and H. A. Gasteiger, *J. Phys. Chem. C*, **118**(11), 5733 (2014).
55. Q. Zou and Y.-C. Lu, *J. Phys. Chem. Lett.*, **7**(8), 1518 (2016).
56. Q. He, Y. Gorlin, M. U. M. Patel, H. A. Gasteiger, and Y.-C. Lu, *J. Electrochem. Soc.*, **165**(16), A4027 (2018).
57. N. S. A. Manan, L. Aldous, Y. Alias, P. Murray, L. J. Yellowlees, M. C. Lagunas, and C. Hardacre, *J. Phys. Chem. B*, **115**(47), 13873 (2011).
58. H. Eckert, Z. Zhang, and J. H. Kennedy, *Chem. Mater.*, **2**(3), 273 (1990).
59. C. Dietrich, D. A. Weber, S. J. Sedlmaier, S. Indris, S. P. Culver, D. Walter, J. Janek, and W. G. Zeier, *J. Mater. Chem. A*, **5**(34), 18111 (2017).
60. S. J. Wen, T. J. Richardson, D. I. Ghantous, K. A. Striebel, P. N. Ross, and E. J. Cairns, *J. Electroanal. Chem.*, **408**(1–2), 113 (1996).
61. H. F. Mark, *Encyclopedia of Polymer Science and Engineering*, New York, Wiley 1985.
62. M. Sumita, Y. Tanaka, and T. Ohno, *J. Phys. Chem. C*, **121**(18), 9698 (2017).
63. M. Sumita, Y. Tanaka, M. Ikeda, and T. Ohno, *J. Phys. Chem. C*, **120**(25), 13332 (2016).
64. T. Hakari, M. Deguchi, K. Mitsuhara, T. Ohta, K. Saito, Y. Orikasa, Y. Uchimoto, Y. Kowada, A. Hayashi, and M. Tatsumisago, *Chem. Mater.*, **29**(11), 4768 (2017).
65. M. Armand, *Adv. Mater.*, **2**(6–7), 278 (1990).
66. F. Lee, M.-C. Tsai, M.-H. Lin, Y. L. Ni'mah, S. Hy, C.-Y. Kuo, J.-H. Cheng, J. Rick, W.-N. Su, and B.-J. Hwang, *J. Mater. Chem. A*, **5**(14), 6708 (2017).
67. H. Zhong, C. Wang, Z. Xu, F. Ding, and X. Liu, *Sci. Rep.*, **6**, 25484 (2016).
68. J. Chen, W. A. Henderson, H. Pan, B. R. Perdue, R. Cao, J. Z. Hu, C. Wan, K. S. Han, K. T. Mueller, J.-G. Zhang, Y. Shao, and J. Liu, *Nano Lett.*, **17**(5), 3061 (2017).
69. T. H. Hester, D. E. Castillo, and D. J. Goebbert, *Rapid Communications in Mass Spectrometry*, **27**(14), 1643 (2013).
70. Y. Xiao, J. Jiang, and H. Huang, *Sci. Rep.*, **4**, 6305 (2014).
71. C. Elschenbroich, *Organometallics, s.l.*, Wiley-VCH 2016.
72. H. V. Tartar and C. Z. Draves, *J. Am. Chem. Soc.*, **46**(3), 574 (1924).

Supporting Information

Understanding Chemical Stability Issues between Different Solid Electrolytes in All-Solid-State Batteries

**Nathalie Riphaus,^{*,a,b} Barbara Stiaszny,^b Hans Beyer,^a Sylvio Indris,^{c,d} Hubert A.
Gasteiger,^a Stefan J. Sedlmaier^b**

^a Chair of Technical Electrochemistry, Department of Chemistry and Catalysis Research
Center, Technische Universität München, 85748 Garching, Germany

^b BMW Group, 80809 München, Germany

^c Institute for Applied Materials – Energy Storage Systems, Karlsruhe Institute of
Technology, 76344 Eggenstein-Leopoldshafen, Germany

^d Helmholtz Institute Ulm, 89081 Ulm, Germany

E-mail:

nathalie.riphaus@tum.de

Index:

1. Image of an aged PEO₁₅LiTFSI membrane which was in contact with an LSPS pellet.
2. X-ray diffraction (XRD) measurement of the pristine LSPS.
3. XPS spectra of an LSPS pellet exposed to humidified argon.
4. XPS spectra of pristine LSPS and comparison with aged LSPS-LiOH.
5. XPS spectra of the aged interface between LiOH-LSPS and a PEO membrane.
6. XPS spectra of a PEGDME membrane aged in contact with LSPS.

1. Image of an aged PEO₁₅LiTFSI membrane which was in contact with an LSPS pellet.

Electrochemical impedance spectroscopy (EIS) evolution over time at a constant temperature of 40 °C was performed to evaluate the calendar aging of PEO₁₅LiTFSI membranes in contact with LSPS. In order to exclude interfering influences from Li metal, stainless steel (SS) current collectors were applied. The aging tests indicated chemical stability issues between LSPS and PEO₁₅LiTFSI, which are accompanied by an increase in resistance. As Figure S1 shows, cell disassembly after testing revealed an intense yellow coloration of the polymer membrane, supporting this finding.

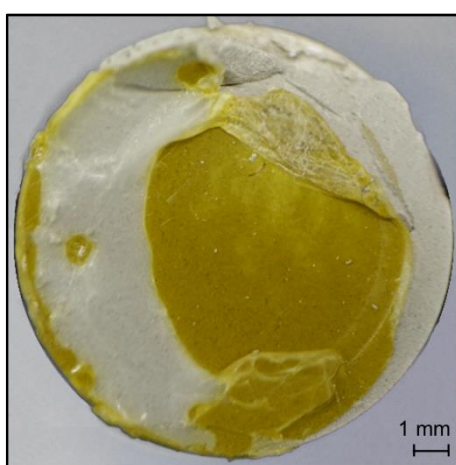


Figure S1. Image of a PEO₁₅LiTFSI membrane on top of a LSPS pellet after aging for appx. 7 days at 60 °C in an SS | PEO₁₅LiTFSI | LSPS | PEO₁₅LiTFSI | SS cell. The intense yellow coloration clearly indicates decomposition. The partial delamination originates from cell disassembly.

2. X-ray diffraction (XRD) measurement of the as-received LSPS.

XRD analysis of the as-received LSPS powder was conducted in order to identify potential side phases. As Figure S2 shows, Rietveld refinement revealed 7.94% Li_7PS_6 as the only side phase of LSPS, confirming the MAS NMR results (see Figure 8 in the main text). Li_7PS_6 also been reported as a side phase of commercially available LSPS by Kaus et al.¹

Experimental. The as-received LSPS powder was measured in a sealed glass capillary with a diameter of 0.5 mm. XRD was performed at a STOE STADI/P powder diffractometer, using Mo $K\alpha_1$ radiation ($\lambda = 0.7093 \text{ \AA}$), a Ge(111) monochromator and a Debye-Scherrer geometry within a 2θ range of $3 - 61^\circ$ (scan step 0.15° , time/step 10 sec). Rietveld refinement was done using FullProf Suite.

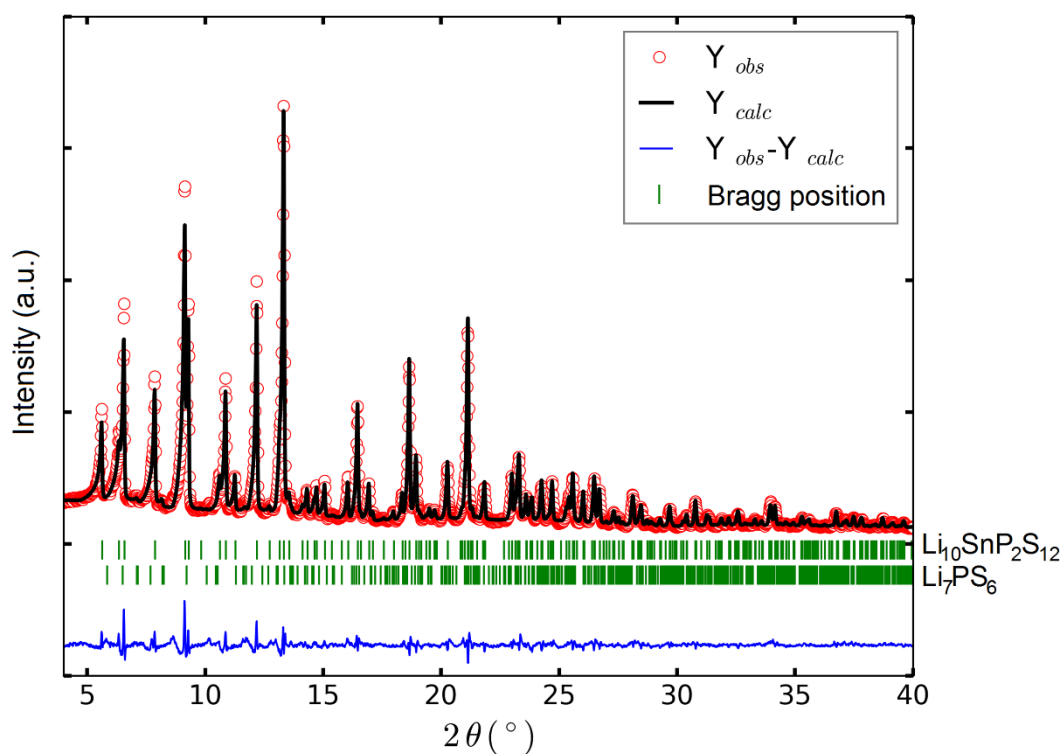


Figure S2. XRD pattern of the as-received LSPS with Rietveld refinement ($\lambda = 0.7093 \text{ \AA}$). The main phase, LSPS; was refined to 92.06%. The remaining 7.94% were assigned to Li_7PS_6 .

¹ M. Kaus, H. Stöffler, M. Yavuz, T. Zinkevich, M. Knapp, H. Ehrenberg and S. Indris, *J. Phys. Chem. C* **2017**, *121* (42), 23370–23376.

3. XPS spectra of an LSPS pellet exposed to humidified argon.

The reaction of LSPS with trace water in the system was considered as one possible origin of the degradation phenomena observed in this study. One of the tests to examine this possibility included investigation of the reaction products of LSPS with water. For this, an LSPS pellet was placed in a cell which then was purged with humidified argon at 25 °C for appx. 1 h. Subsequently, the surface of the pellet was analyzed via XPS. Fitting of the spectra revealed Li_2S , LiOH , elementary tin as well as reduced phosphorus species as the reaction products, next to only minor amounts of SO_x compounds (Figure S3).

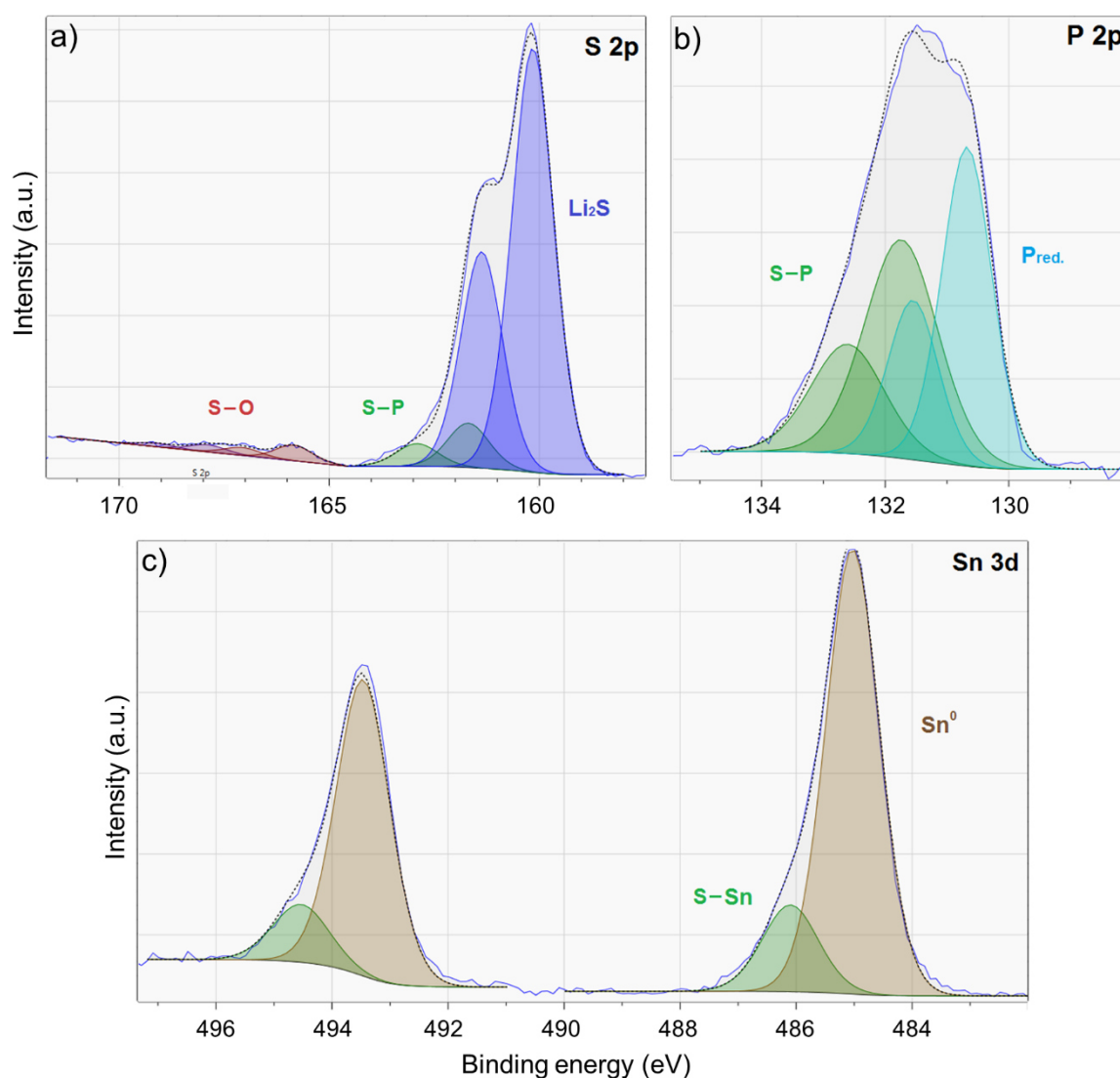


Figure S3. a) XPS S 2p, b) XPS P 2p, c) XPS Sn 3d spectra of an LSPS pellet placed in a cell which was purged with humidified argon. Green peaks are assigned to PS_4^{3-} or SnS_4^{4-} bonds in LSPS (161.7, 468.1, 131.8 eV), red peaks to S–O bonds (165.8, 167.8 eV), blue peaks to Li_2S (160.2 eV), brown peaks to Sn^0 (485.0 eV) and turquoise peaks to reduced P (130.7 eV).

4. XPS spectra of pristine LSPS and comparison with aged LSPS-LiOH.

XPS analysis of a pristine LSPS pellet was performed in order to identify potential contaminants. Beside the Li_7PS_6 phase identified by XRD (see Figure S2), XPS analysis revealed LiOH and Li_2CO_3 as surface impurities in LSPS (Figure S4). A clear assignment of the O 1s peak to LiOH was possible by comparative measurements with an LSPS-LiOH pellet (wt. ratio 2:1), which gave an O 1s signal at the same binding energy. A LSPS-LiOH sample was moreover stored at 60 °C for two weeks. Subsequent XPS analysis gave no changes in the spectra, as exemplarily shown for the S 2p spectrum in Figure S5. The two materials were thus proven to not react with each other.

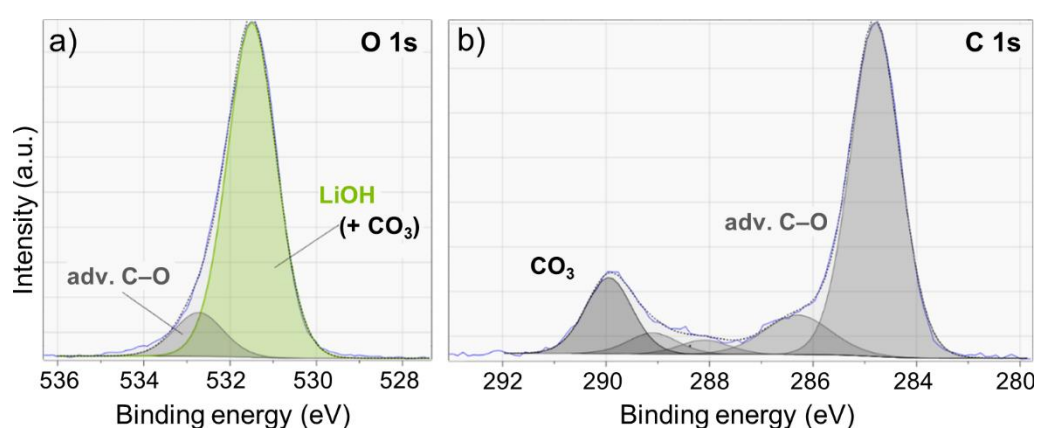


Figure S4. a) XPS O 1s and b) XPS C 1s spectra of pristine LSPS. Peaks assigned to adventitious carbon are shown in light grey. The dark grey peak in the C 1s can be attributed to Li_2CO_3 (290.0 eV). The respective O 1s peak appears at 531.8 eV. Although it is impossible to distinguish between Li_2CO_3 and LiOH in the O 1s spectra, quantification of the respective C 1s peak of Li_2CO_3 clearly shows that it cannot make up for more than 50% of the O 1s peak.

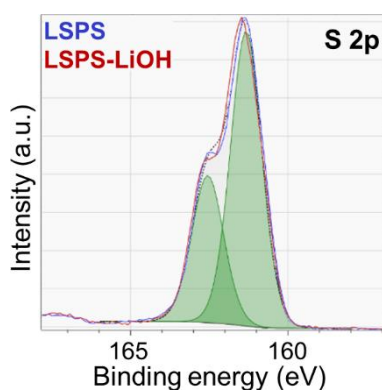


Figure S5. Overlay of the XPS S 2p spectra of pristine LSPS (blue) and LSPS-LiOH aged at 60 °C (red). The green peaks can be assigned to PS_4^{3-} or SnS_4^{4-} bonds in LSPS (161.2 eV).

5. XPS spectra of the aged interface between LiOH-LSPS and a PEO membrane.

As shown in Figure S3, LiOH was found as a surface contaminant on pristine LSPS. In order to probe whether LiOH affects the degradation in contact with PEO, an SS | LSPS-LiOH | PEO | SS cell was stored for appx. 7 days at 60 °C. Subsequent XPS analysis revealed a much higher sulfite amount than in SS | LSPS | PEO | SS cells stored under the same conditions (see Figure 9 in the main text), and even traces of sulfate were detected (Figure S6).

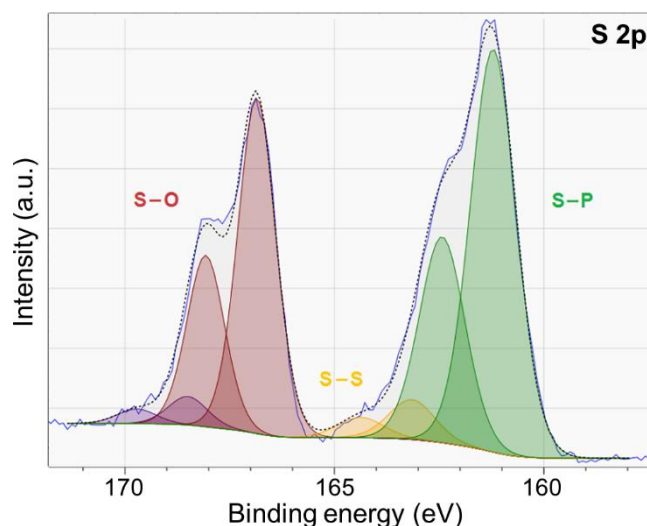


Figure S6. XPS S 2p spectra of the interface between LSPS-LiOH and PEO after aging in a SS | LSPS-LiOH | PEO | SS cell at 60 °C over appx. 7 days. Purple peaks are attributed to S–O bonds in sulfate (168.5 eV), red peaks to S–O bonds in sulfite (166.9 eV), yellow peaks to S–S bonds in polysulfides (163.2 eV), and green peaks to S–(P/Sn) bonds in LSPS (161.2 eV).

6. XPS spectra of a PEGDME membrane aged in contact with LSPS.

Aging tests with polyethylene glycol dimethyl ether (PEGDME) membranes were performed in order to assess the impact of the hydroxyl groups in PEO on the degradation reaction with LSPS. PEGDME features methoxy end groups instead, thus a potential reactivity of hydroxyl groups can be excluded. XPS analysis after calendar aging of an SS | PEGDME | LSPS | SS cell for appx. 7 days at 60 °C yielded polysulfides, which was further verified by UV-Vis spectroscopy. As Figure S7 shows, no S–O species were detected in the S 2p spectrum contrary to XPS experiments with aged LSPS-PEO samples (see Figure 9 in the main text).

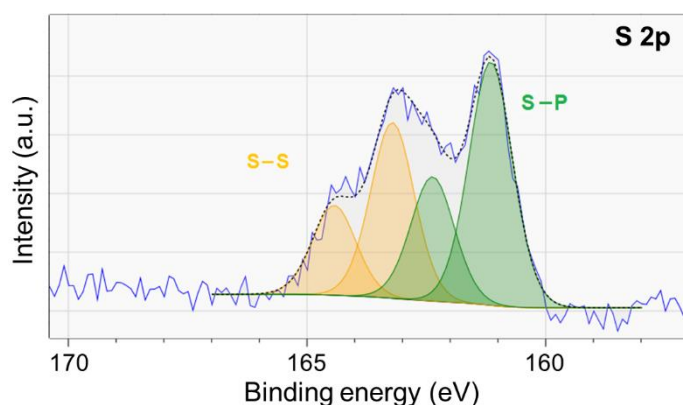


Figure S7. XPS S 2p spectra of a PEGDME membrane after aging in an SS | PEGDME | LSPS | SS cells using LSPS powder at 60 °C over appx. 7 days. Yellow peaks are attributed to S–S bonds in polysulfides (163.0 eV) and green peaks to S–(P/Sn) bonds in LSPS (161.0 eV).

3.2 Towards the Fabrication of ASSB Components on Large-Scale

The second main topic of this thesis deals with processing strategies for two ASSB cell components – the solid electrolyte separator (SES) and the composite cathode. To date, literature on those topics is rarely available. Indeed, despite the increasing demand for an automotive ASSB cell concept, most bulk-type laboratory cells are fabricated by direct cold-pressing of the crude powder material.³⁹ As discussed in more detail in chapter 1.3, this method gives rise to several problems.

On the one hand, thick SES layers of several hundred micrometers are fabricated to prevent short-circuiting by lithium dendrite growth. At the same time, low percentages of less than 80 wt.% cathode active material were used to ensure sufficient ionic percolation. Consequently, the energy density often reaches not even 10% of the target of 800 Wh·l⁻¹ at cell level.^{2,40,41} On the other hand, as mass production of ASSB cells requires scalable processes, powder compression on large scale does not seem to be an option. Besides extremely high pressures, which would be required, the remaining porosity will most likely be too high. Furthermore, the components have to provide a certain flexibility, at least if roll-to-roll processes are implemented.¹⁸ Therefore, different processing methods are evaluated within this thesis.

First, slurry-based fabrication of SE layers comprising LSPS and a polymeric binder was probed and general guidelines for a deliberate choice of the binder for sulfide-based solid electrolytes were developed. Subsequently, the two-component system was expanded to a four-component one, meaning that the cathode active material and a carbon additive were added to the system consisting of the solid electrolyte and a polymeric binder. In particular, the impact of different processing parameters on the homogeneity of composite cathode sheets was evaluated.

3.2.1 Slurry-based Processing of Solid Electrolytes

In this section, the article “Slurry-based Processing of Solid Electrolytes – A Comparative Binder Study” is presented. The paper was published in the *Journal of The Electrochemical Society* in December 2018 as open access article.¹³¹ The results were further presented by Nathalie Riphaut at the *AiMES Meeting of The Electrochemical Society* in Cancun, Mexico (Sep 30th – Oct 4th, 2018), abstract #323.

Different polymer materials were investigated in the scope of this study concerning their suitability as binders for thin and free-standing SE sheets based on LSPS. Our interest in slurry processing methods was mainly driven by the need for thin SES layers. As mentioned, a thickness comparable to the separator in conventional LIBs, meaning 20 – 30 μm , is required for competitive energy densities in ASSB cells.^{18,39} Apart from that, a slurry-coating process enables introduction of a flexible component such as a polymeric binder. The effect of the latter on processing properties as well as properties of the resulting SE layer though has been rarely studied so far.

Therefore, different binders were examined and a broad parameter study was conducted to optimize e.g. LSPS-to-binder ratio and viscosity. Although these had to be adapted to the binder used, some general trends could be identified. One important aspect is the minimum amount of binder required for mechanically stable sheets. Moreover, clear differences between the SE sheets regarding homogeneity, porosity and mechanical stability were observed by means of SEM analysis and bend tests. The impacts of binder type and weight fraction on ionic conductivity were evaluated with PFG NMR measurements, revealing additional differences between the tested binders. In a last step, the PFG NMR results were compared to a more standardized method for conductivity measurements – impedance spectroscopy. Despite the lower value determined by AC impedance analysis, the ionic conductivity was proven to be sufficiently high for potential application of these SE sheets in ASSBs.

With this study we wanted to emphasize the prominent role of the polymeric binder in slurry-processed SE layers. In comparison to recent publications,^{64,65,67,68} this paper provides a significant expansion of tested binders and analytical methods. We thereby demonstrated the importance of a deliberate choice of parameters to achieve good processing properties as well as desirable features for the SE sheet.

Author contributions

Nathalie Riphaut, Barbara Stiaszny and Stefan J. Sedlmaier developed the concept for the study. Nathalie Riphaut and Philipp Strobl prepared the SE sheets. Sylvio Indris and Tatjana Zinkevich carried out the PFG NMR experiments. Joscha Schnell and Philipp Strobl took care of the bend tests. The XRD analysis was conducted by Murat Yavuz. Nathalie Riphaut performed all further experiments. Together with Hubert A. Gasteiger and Stefan J. Sedlmaier, she also wrote the manuscript. All authors discussed the results and commented on the manuscript.



Slurry-Based Processing of Solid Electrolytes: A Comparative Binder Study

Nathalie Riphaus,^{1,2,*} Philipp Strobl,^{1,2} Barbara Stiaszny,² Tatiana Zinkevich,^{3,4} Murat Yavuz,³ Joscha Schnell,⁵ Sylvio Indris,^{3,4} Hubert A. Gasteiger,^{1,**} and Stefan J. Sedlmaier^{1,2}

¹Chair of Technical Electrochemistry, Department of Chemistry and Catalysis Research Center, Technische Universität München, 85748 Garching, Germany

²BMW Group, 80809 Munich, Germany

³Institute for Applied Materials - Energy Storage Systems, Karlsruhe Institute of Technology, 76344 Eggenstein-Leopoldshafen, Germany

⁴Helmholtz Institute Ulm, 89081 Ulm, Germany

⁵Institute for Machine Tools and Industrial Management, Technische Universität München, 85748 Garching, Germany

Limited energy density of today's Li-ion battery technologies demands for novel cell technologies, such as the all-solid-state battery (ASSB). In order to achieve high energy densities and enable large-scale processing, thin and flexible solid electrolyte (SE) layers have to be implemented. This study focuses on slurry-based processing of the sulfidic solid electrolyte $\text{Li}_{10}\text{SnP}_2\text{S}_{12}$ (LSPS). Various polymers were investigated concerning their suitability as binders for thin and freestanding SE sheets. We conducted a parameter study in order to optimize e.g. LSPS-to-binder ratio, solids content and porosity. Significant differences were found with regard to the minimum amount of binder required for mechanically stable sheets as well as the homogeneity, density and flexibility of the resulting SE layers. The impacts of binder type and weight fraction on ionic conductivity were examined through lithium diffusion measurements. Impedance analysis was conducted in comparison, proving sufficiently high ionic conductivity for potential application of the SE sheets in ASSB. This work highlights the important role of the polymeric binder in slurry-based processing of SEs and gives an impression how important a well-considered selection of parameters is to achieve good processing properties as well as desirable features for the final SE sheet.

© The Author(s) 2018. Published by ECS. This is an open access article distributed under the terms of the Creative Commons Attribution 4.0 License (CC BY, <http://creativecommons.org/licenses/by/4.0/>), which permits unrestricted reuse of the work in any medium, provided the original work is properly cited. [DOI: 10.1149/2.0961816jes]



Manuscript submitted October 9, 2018; revised manuscript received December 3, 2018. Published December 22, 2018. This was Paper 323 presented at the Cancun, Mexico, Meeting of the Society, September 30–October 4, 2018.

Battery electric vehicles (BEV) are constantly gaining popularity. Effective penetration of the mass market, however, requires a significant improvement in energy density whilst keeping costs reasonable. This is mainly owed to the demand for extended driving ranges above 500 km (300 miles). These ranges ask for volumetric energy densities exceeding $800 \text{ Wh} \cdot \text{l}^{-1}$ at cell level. In contrast, only half of this value is reached in current prismatic cells of BEVs, based on established Li-ion battery (LIB) technologies.¹

The all-solid-state battery (ASSB) concept has attracted growing interest as a promising battery system to potentially achieve higher energy density.² This is based on the assumption that solid electrolytes (SE) should more likely enable the use of lithium metal as anode material as well as high-voltage cathode materials compared to liquid electrolytes, although recent studies revealed that the initially postulated high electrochemical stability was a misconception.³ Most bulk-type ASSBs reported to date are based on thick SE layers and cathodes with low cathode active material loadings, resulting in energy densities below $50 \text{ Wh} \cdot \text{l}^{-1}$ at cell level.^{4,5} Indeed, for being competitive with conventional LIBs, energy density calculation reveal that the SE layer thickness has to be in the $< 100 \mu\text{m}$ range.⁶ In addition, a certain mechanical stability is essential for scalable processing.⁷ Consequently, evolution from pellet-type ASSBs, prepared by powder compression, to sheet-type ASSBs, which are based on slurry-coating processes, is essential.^{4,8}

The fabrication of thin sheet-like layers in turn demands the use of polymeric binders that are chemically compatible with the SE materials.⁹ This on the other hand allows for addressing two challenges of ASSBs. One major problem is attributed to rigid solid-solid interfaces that lead to high total cell resistances.^{10,11} Introduction of a soft binder that enhances the flexibility of the SE layer could improve adhesion to the electrodes. Its softness might moreover reduce issues evolving from volume changes of the active materials during

cycling, which cause inconsistent interfaces between the SE layer and the electrodes.^{12–14} Due to their deformable nature, sulfide-based SEs can generally be processed easier and enable better contacting with the electrodes, compared to oxide-based SEs.^{2,3} Furthermore they provide higher ionic conductivities of up to $25 \text{ mS} \cdot \text{cm}^{-1}$, exceeding those of current liquid electrolytes.^{15–17} Their high reactivity toward moisture, however, requires handling under inert atmosphere.⁶

In general, slurry-based processing of SEs demands to carefully consider the choice of solvent and binder. Besides chemical stability with the SE material, typical processing challenges like shrinkage and warpage during drying and densification of the SE sheet need to be overcome.⁶ Requirements on the binder include solubility in the solvent, non-reactivity with the SE, good adhesive strength and minimal effect on the resistivity of the SE layer.^{6,18} Polymeric binders with polar functional groups such as nitrile, which can interact with the SE, have been reported as favorable.¹⁸ In the case of sulfide-based SEs this however contrasts with the demands on the solvent, which has to be less polar due to their high reactivity with polar protic solvents. Hence, the number of applicable binders for sulfidic SEs is limited.¹⁹

To date, literature related to solution-based processing of ASSBs is scarce, and even less is reported on fabrication of thin, freestanding SE layers. Nam et al. applied a polymer scaffold (i.e. a non-woven porous polymeric material) to obtain bendable SE layers of roughly $70 \mu\text{m}$ thickness.²⁰ They tested two sulfide-based SEs, crystalline $\text{Li}_{10}\text{GeP}_2\text{S}_{12}$ (LGPS) and glass-ceramic Li_3PS_4 (LPS). The latter has also been used in a study by Lee et al.,¹⁸ who investigated different solvents and binders. They reported the combination of acrylonitrile butadiene rubber (NBR) with p-xylene, yielding SE sheets with an AC impedance derived ionic conductivity effectively equal to pressed LPS samples. It was concluded that although incorporation of a non-conductive binder is expected to reduce the ionic conductivity of the SE layer according to various reports,^{4,7,9,14,19} the good distribution and ion-dipole interaction of NBR results in a compensation of the intrinsically lower conductivity. The benefits of forming a freestanding SE layer instead of directly coating the SE on one of the electrodes

*Electrochemical Society Member.

**Electrochemical Society Fellow.

⁷E-mail: nathalie.ripkaus@tum.de

became clear in a study by Ito et al.²¹ They found, for instance, that using the same binder in the electrode and the SE layer leads to mutual dissolution at the interface.

In the present study, we applied a slurry-coating process to fabricate bendable thin and freestanding SE sheets. The thiostannate analogue of LGPS, $\text{Li}_{10}\text{SnP}_2\text{S}_{12}$ (LSPS), that shows a comparably high ionic conductivity of 2–5 mS/cm,^{22–25} and toluene were selected as the model electrolyte and solvent, respectively. We systematically investigated a wide range of binders with regard to their impacts on processability, flexibility, density and resistivity of the resulting SE layer and found clear differences between the binders. For those exhibiting good processability, homogeneous distribution between SE particles, chemical compatibility with LSPS and excellent flexibility of the compressed sheets is shown. Moreover, we evaluated the impact of binder content on ionic conductivity. Compared to recent studies,^{7,18–20} this contribution demonstrates a significant expansion of tested binders and analytical tests, addressing important requirements for scalable roll-to-roll processing of ASSBs.

Experimental

Materials.—All materials were handled within an argon filled glove box ($\text{O}_2, \text{H}_2\text{O} < 1$ ppm; GS Glovebox Systemtechnik GmbH). $\text{Li}_{10}\text{SnP}_2\text{S}_{12}$ (>95%, LSPS) was purchased from NEI Corporation and used without further purification. Polyisobutene (PIB) at an average molecular weight M_w of $3.1 \cdot 10^6 \text{ g} \cdot \text{mol}^{-1}$ was delivered by BASF SE. Poly(methyl methacrylate) (PMMA, M_w 4–5.5 · 10⁵ g · mol⁻¹) was purchased from Alfa Aesar and poly(styrene-co-butadiene) (SBR, M_w 1.9 · 10⁵ g · mol⁻¹) at a butadiene content of 4 wt% from Sigma Aldrich Corp. Poly(ethylene vinyl acetate) (PEVA, M_w 3.5 · 10⁵ g · mol⁻¹) containing 60 wt% vinyl acetate and poly(acrylonitrile butadiene) (HNBR, 5.5 · 10⁵ g · mol⁻¹) with 17 wt% acetonitrile were provided by Arlanxeo. All binders were dried in a vacuum oven (Büchi B-585 Drying) at 80 °C for 72 hours. Toluene was purchased from Merck Millipore and dried over molecular sieve (pore size 3 Å, Merck Millipore) before use.

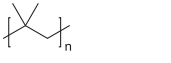
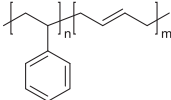
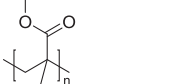
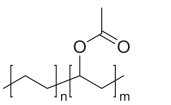
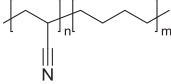
Fabrication of SE sheets.—All process steps were conducted in an argon filled glove box. LSPS was first homogenized using mortar and pestle and then dispersed in toluene by stirring. The binder was dissolved in toluene, and the respective amount of binder solution was added to the LSPS dispersion. After stirring for at least 12 hours, the viscosity of the slurry was adjusted and the slurry was coated on siliconized polyester foil (PPI Adhesive Products GmbH) using the doctor blade technique. The SE sheets were dried at room temperature for 1 hour at ambient pressure and further 12 hours under dynamic vacuum. For compression, the sheets were sealed into aluminum foil pouch and calendered at 60 °C outside the glove box. The gap size was reduced by 10 μm per step until the pouch bag started curling up.

Determination of porosity.—Samples were punched (Nogamigiken Co. Ltd, 12 mm diameter) of the SE sheet and their height and weight was measured. The porosity was then calculated as the difference between measured and theoretical density.

Scanning electron microscopy (SEM).—To assess the homogeneity, SEM and energy dispersive X-ray diffraction (EDX) mapping was conducted. The samples were therefore mounted on the sample holder and transferred to the SUPRA 55VP (Zeiss) in an air-tight transport vessel to minimize exposure to ambient air (< 5s).

Determination of mechanical properties.—Flexibility was evaluated with a Mandrel Bend Test according to DIN-EN-ISO 1519:2011, using cylindrical mandrels at a diameter of 8 to 3 mm. The freestanding SE sheets were fixed in a self-made holder system developed at the *iwb*.

Table I. Selected binders, their average molecular weight and their chemical structures.

Binder	Average M_w	Structure
Polyisobutene (PIB)	$3.1 \cdot 10^6 \text{ g} \cdot \text{mol}^{-1}$	
Styrene butadiene rubber (SBR)	$1.9 \cdot 10^5 \text{ g} \cdot \text{mol}^{-1}$	
Poly(methyl methacrylate) (PMMA)	$4\text{--}5.5 \cdot 10^5 \text{ g} \cdot \text{mol}^{-1}$	
Poly(ethylene vinyl acetate) (PEVA)	$3.5 \cdot 10^5 \text{ g} \cdot \text{mol}^{-1}$	
Hydrogenated nitrile butadiene rubber (HNBR)	$5.5 \cdot 10^5 \text{ g} \cdot \text{mol}^{-1}$	

⁷Li pulsed field-gradient nuclear magnetic resonance spectroscopy (PFG NMR).—SE sheets were fixed in polypropylene tubes and placed inside air-tight NMR tubes. Experiments were conducted at a Bruker Avance 300 MHz spectrometer operated at a ⁷Li frequency of 116.6 MHz. The spectrometer was equipped with a Diff50 probe, which produces pulsed field gradients of up to 30 T/m. A stimulated-echo pulse sequence in combination with bipolar gradients was used to observe the echo damping as a function of gradient strength. The detailed procedure has been previously described elsewhere.²⁴

Results and Discussion

Selection of materials.—In order to conduct a comparative binder study, a suitable model solid electrolyte and solvent had to be selected in the first place. As the motivation behind this work is to pave the way for large-scale production of sheet-type SE layers, only commercially available materials were considered, limiting the choice of sulfide-based SEs. LSPS from NEI Corporation was selected due to its high ionic conductivity of 2–5 mS · cm⁻¹,^{22–24} which comes close to that of its thiogermanate analogue LGPS that has been reported to have one of the highest conductivities of 12 mS · cm⁻¹.²⁶ In contrast, the price can be significantly reduced by the replacement of Ge with Sn, making LSPS more attractive for large-scale applications.²²

As mentioned, the high reactivity of sulfide-based SEs with polar protic solvents, leading to evolution of H₂S, requires the use of less or non-polar solvents instead.¹⁹ Yamamoto et al. found that solvents with a high donor number, like propylene carbonate or diglyme, react with the chemically similar electrolyte LPS by nucleophilic attack.⁹ In contrast, various studies have shown excellent stability in solvents with low donor number, such as heptane, toluene, *p*-xylene or dichloroethane.^{5,9,18} Since too fast evaporation of the solvent leads to inhomogeneous coatings with bulged surfaces, a further demand for slurry-processing is a low vapor pressure.⁵ Therefore, toluene with a moderate vapor pressure of 3.8 kPa²⁷ was selected in this study.

Once the solvent was defined, the next step comprised the selection of binders to be tested. The baseline requirements to be met were solubility in toluene and absence of protic functional groups, which would cause again decomposition reactions with the SE. Table I shows

Table II. Value ranges for all varied parameters of the slurry processing study.

LSPS: binder ratio [wt%]	Solids content in the slurry [wt%]	Applicator gap [μm]	Layer compression and resulting thicknesses
97.5 : 2.5	LSPS 20–30	200–400	No compression
95.0 : 5.0	Binder 5–20		→ Dry film: 50–100 μm
92.5 : 7.5	Overall 20–45		Calendering at 60°C (sealed in pouch bag)
90.0 : 10.0			→ Dry film: 20–40 μm

the chosen binders. In order to gain a comprehensive understanding of the effect of the chemical nature of the binder on its performance, diverse material classes ranging from aliphatic to aromatic, including different functional groups, were covered. PIB is a fully saturated hydrocarbon, whereas SBR contains aromatic units. PMMA and PEVA both have ester side chains attached to the hydrocarbon backbone, with the number of functional groups being much larger for PMMA. NBR provides a nitrile functionality. The hydrogenated variant HNBR was used to further differentiate from SBR.

As the binders shall be used in the SE separator layer, another key requirement is negligible electronic conductivity. To probe this, pure binder films with dry-film thicknesses of 15–30 μm were casted and tested electrochemically. Linear sweep voltammetry (LSV) was performed to apply a distinct voltage to the sample and measure the current response. While PIB, SBR and PMMA showed no current flow over the voltage range of 0–5 V (Figure S1a), a low current of up to 45 nA was detected for PEVA and HNBR at elevated temperatures (Figure S1b). However, the electronic conductivity in the range of $10^{-11} \text{ S} \cdot \text{cm}^{-1}$, calculated from chronoamperometry measurements, is negligible. In addition, as no current peaks were detected in the LSV measurements, electrochemical stability in the applied voltage range can be concluded for all binders.

In the next step, their chemical inertness with LSPS was investigated. To provoke possible decomposition reactions, SE sheets with a LSPS: binder ratio of 90 : 10 wt% were stored for prolonged time at 60°C. Subsequent X-ray photoelectron spectroscopy (XPS) and Fourier transform infrared spectroscopy (FTIR) measurements showed no difference between the aged samples and the pristine materials (exemplary shown for LSPS-PEVA/-PIB in Figure S2/S3). Hence, all binders fulfilled the requirements for further investigations.

Fabrication and characterization of freestanding SE sheets.—

In order to evaluate the influences of the binder on the processability, flexibility, density and resistivity of SE thin layers, freestanding LSPS sheets were prepared by slurry-processing. All relevant process parameters, namely LSPS-to-binder ratio, solids content in the slurry, applicator gap size and compression method were varied in an extensive parameter study. The ranges of the parameters employed are listed in Table II.

A first criterion for assessing the processability of the slurry was its viscosity. The solids content in the slurry served as a measure for it. In case of a low solids content, the slurry leaks out of the applicator, whereas a slurry too viscous sticks to the applicator and cannot be processed. The study revealed that the optimum viscosity strongly depends on the type of binder used, whereas the amount of binder had less impact. The quality of PEVA-based sheets turned out to be particularly dependent on the solids content. While excellent layers were yielded at roughly 45%, lower solids contents resulted in very inhomogeneous layers. The viscosity of SBR- and PMMA-based slurries, in contrast, had to be in the range of 20% for comparable results. PIB as well as HNBR could be processed best at about 40% solids content for low binder contents, however the viscosity had to be reduced if the binder content was increased.

Also relevant in this context was the wettability of the slurry. A generally good wetting behavior was expected, as both solvent and carrier foil are non-polar. Depending on the polarity of the binder, the wettability of the slurry is affected to a greater or lesser extent. For those slurries based on the most polar binder, PMMA, no homoge-

neous coating could be obtained throughout the wide range of tested process parameter combinations. In all cases, the SE sheet rolled up during drying, indicating that the cohesive forces within the slurry exceed the adhesive forces between slurry and carrier foil (Figure 1c). In contrast, very homogeneous coatings were obtained for slurries comprising the non-polar binders PIB and SBR (Figures 1a/1b). The best results according to optical inspection could be achieved with PEVA and HNBR. These coatings were not only very homogeneous, but also showed well-defined edges (Figures 1d/1e). Apparently, the combination of a non-polar polymer backbone and a relatively low amount of polar functional groups enables both good cohesion in the slurry and good adhesion to the carrier foil.

Independently of the LSPS-to-binder ratio as well as the solids content in the slurry, an applicator gap size of 200 μm was identified as the optimum for all binders. According to the solids contents, dry-film thicknesses ranging between roughly 50 μm for SBR and 100 μm for PEVA were obtained for the uncompressed sheets. Subsequent calendering allowed for reduction of the film thickness by 55–70%, while the greatest densification was achieved for the thickest sheet. The final film thicknesses after calendering varied between 20–40 μm .

To further evaluate the SE sheets, their homogeneity after calendering was examined in greater detail. A homogeneous sample should provide small variations in coating height and porosity over the SE layer as well as uniform distribution of the binder between SE particles. To examine the latter, EDX mapping was conducted. Exemplary elemental maps and SEM images are shown in Figure 2 for LSPS layers processed with the various binders. It should be mentioned that all sheets were fabricated under identical conditions and the same batch of SE powder was used for all experiments to ensure comparability.

Significant differences can already be observed at a low magnification for the PMMA-based sheet (Figure 2c, top), which shows a very rough surface with many agglomerates. Zooming in further reveals that, contrary to the other samples, bigger particles are not embedded in the plane but rise above, increasing the roughness (Figure 2, middle). The EDX maps revealed two different distribution patterns of the binders. SBR, PIB and PMMA show a granular domain structure, with small binder agglomerates (red) between SE particles (yellow). This is most visible for the SBR-based layer (Figure 2b). In contrast, PEVA and HNBR form a film on the SE particles, indicated by a uniform orange coloration of the EDX maps (Figures 2d/2e). While

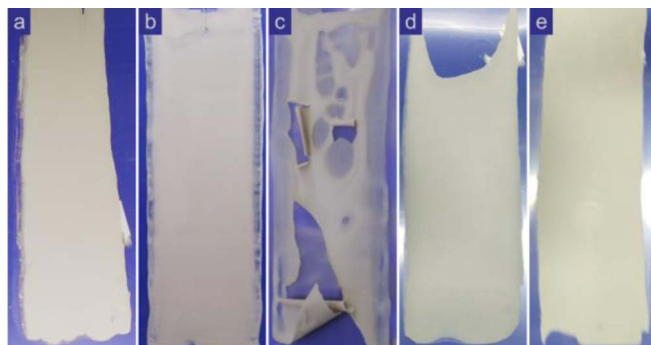


Figure 1. Images of cast SE films (200 μm wet-film thickness), containing 10 wt% of (a) PIB, (b) SBR, (c) PMMA, (d) PEVA and (e) HNBR.

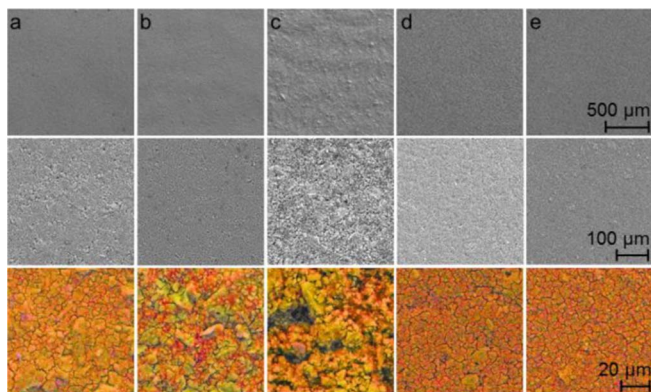


Figure 2. SEM images (top, middle) and EDX maps (bottom, yellow: sulfur, red: carbon) of SE sheets containing 10 wt% binder. (a) PIB, (b) SBR, (c) PMMA, (d) PEVA and (e) HNBR.

this homogeneous binder distribution apparently results in a smoother surface, the continuous film might be detrimental for the ionic conductivity. Inada et al. found that a binder coating covering the SE particles remarkably hinders ionic transport, whereas binder domains barely affect the conductivity.²⁸ It should be noted that the gray spots arise from indentations on the surface, which cannot be reached by the EDX beam.

Both optical evaluation and SEM imaging demonstrated that PMMA is unsuitable to fabricate homogeneous and dense SE sheets, thus this binder was not further considered. Distinct differences between the remaining four were observed for the minimum amount of binder required to obtain processible, freestanding SE sheets. Previous studies have shown that the resistivity of SE layers increases with binder content, owing to the insulating behavior of the polymers.^{9,14} Consequently, the amount of binder should be reduced as far as possible. With SBR, 10 wt% (equaling to about 20 vol.%) were necessary to fabricate a homogeneous, freestanding SE sheet with low porosity, whereas 7.5 wt% PEVA delivered comparable results. For HNBR and PIB, a much lower binder content of 2.5 wt% was sufficient.

These differences might be associated with the molecular weight of the polymeric binders. An interesting correlation between adhesion properties and molecular weight of the binder was reported by Lee et al., who studied LTO electrodes for conventional LIBs.²⁹ They found that adhesion as well as surface coverage of the LTO particles enhances with increasing molecular weight of their carboxymethyl cellulose binder. The PIB used herein had the highest average molecular weight of $3.1 \cdot 10^6 \text{ g} \cdot \text{mol}^{-1}$, followed by HNBR with $5.5 \cdot 10^5$, PEVA with $3.5 \cdot 10^5$ and SBR with $1.9 \cdot 10^5 \text{ g} \cdot \text{mol}^{-1}$. This trend turned out to be in line with the amount of binder required for homogeneous, processible SE sheets. Apart from molecular weight, the chemical

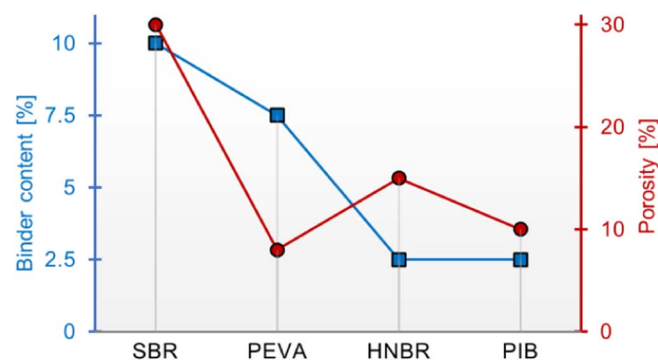


Figure 3. Relation between required minimum amount of binder to obtain freestanding, processible SE sheets (blue) and resulting porosity after calendaring (red) for the different binders SBR, PEVA, HNBR and PIB.

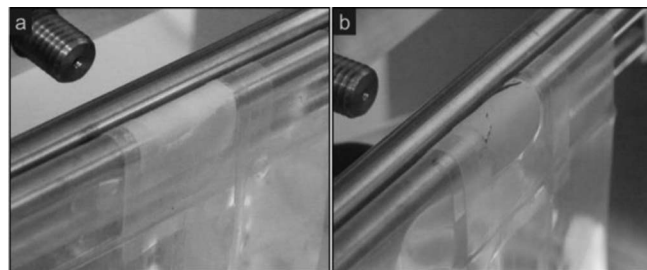


Figure 4. Mandrel Bend Tests of a calendared SE sheets with (a) 2.5 wt% HNBR and (b) 10 wt% SBR.

nature of the polymeric binder is expected to affect the properties of the SE sheet. PIB and HNBR constitute saturated hydrocarbons with small side chains, which can easily adhere to the SE particles. Lee et al. moreover found that the nitrile groups of NBR increase the polarity and dipole moment for the interaction between binder and SE, resulting in better adhesion.¹⁸ This might explain why the same binder content of 2.5 wt% is sufficient for PIB and HNBR, although PIB has a much higher molecular weight. PEVA and SBR contain large functional groups, which might hinder intense contact between binder and SE. Apparently, the negative effect of steric hindrance is more significant than the positive effect of polarity, thus demanding for a higher binder quantity of 7.5 and 10 wt%, respectively.

Another important evaluation criterion is the porosity of the SE sheets after calendaring. As Li-ion transport is limited with high porosity, a densification close to 100% of the theoretical density would be ideal to maximize the ionic conductivity. On the other hand, a certain remaining porosity might be beneficial to maintain good mechanical properties.^{6,8} In line with this, Choi et al. found that the porosity of silicon electrodes decreases with increasing binder content.³⁰ They concluded that a certain binder level is essential to achieve sufficient bonding between particles. Figure 3 illustrates the relation between required minimum amount of binder and resulting porosity for the various polymers. Despite the high binder content of 10 wt%, SBR-based sheets could only be compacted to around 70% of the theoretical density upon calendaring, thus roughly 30% porosity remained. In contrast, the calendared layers containing the least amount of binder, namely those with 2.5 wt% HNBR and PIB, yielded a porosity around 15% and 10%, respectively. The best results were obtained for the calendared sheets containing 7.5 wt% PEVA, with porosities as low as roughly 8%.

These results indicate that the amount of binder has only a limiting impact on densification properties. Indeed, the chemical nature might be more relevant. The as-received polymers HNBR, and particularly PIB and PEVA, exhibited a rubberlike consistency, whereas SBR is supplied as hard granules. It is therefore not surprising that compression of the SE sheets is less effective when using SBR. The different properties can also be associated with the chemical structure of the polymer. On the one hand, the unsaturated hydrocarbon backbone introduces a certain stiffness and, on the other hand, the bulky but non-polar side chains might hinder intense bonding to the SE particles. Weaker adhesion caused by bulky functional groups could also explain why a greater amount of binder is required for PEVA compared to HNBR.

The influence of binder content and densification on the properties of the SE sheet was further examined with respect to mechanical properties. In order to assess their flexibility, Mandrel bend tests according to DIN norm ISO 1519:2011 were conducted. Calendared sheets containing 2.5 and 10 wt% binder as well as non-calendared sheets with 2.5 wt% binder were probed. All samples based on PIB, PEVA and HNBR showed excellent bending properties, even for low binder contents. They passed all mandrel diameters without any damage (Figure 4a). In contrast, all SBR-based sheets already broke at bending around the largest mandrel (Figure 4b). This observation is in line with the aforementioned poor densification properties, and can

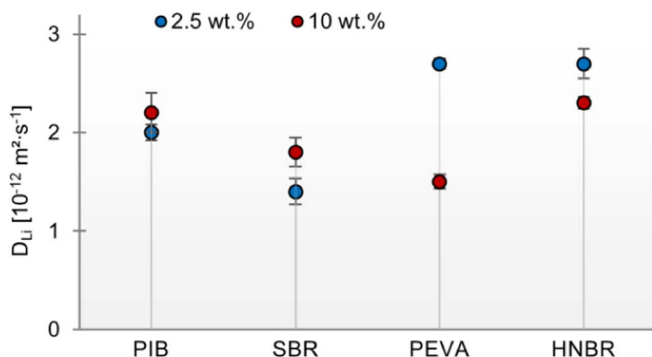


Figure 5. Li-ion diffusion coefficients for calendared SE sheets comprising 2.5 (blue) and 10 wt% (red) PIB, SBR, PEVA and HNBR, respectively, extracted from ^7Li PFG NMR measurements at 30°C. Error bars indicate the measurement accuracy.

again be attributed to the described structural features of the polymer. Since roll-to-roll processes, which demand for a certain bendability, are very likely to be implemented for large-scale fabrication of ASSBs,⁸ SBR-based layers might be unsuitable at this stage.

Evaluation of ionic conductivity.—Besides the mostly physical properties discussed above, the final and most important assessment criterion examined herein is the ionic conductivity of the SE layers. As mentioned, previous studies demonstrated that incorporation of a polymeric binder leads to a reduced ionic conductivity.^{4,7,9,14,19} A much stronger influence was found if the binder forms a film on the SE particles instead of granular domains in between the particles.²⁸ Furthermore, it has been shown for various SE materials that conductivity increases with packing density, i.e. with decreasing porosity.^{17,31,32} Consequently, clear differences in ionic conductivity between the SE layers in this contribution are expected.

The long-range Li-ion transport was probed by means of ^7Li PFG NMR spectroscopy of calendared SE sheets with different binder contents. As demonstrated by Kaus et al.,²⁴ this powerful technique allows for investigation of Li-ion diffusion on time scales of tens or hundreds of milliseconds, corresponding to length scales of several micrometers. An exemplary echo damping versus gradient strength plot can be found in Figure S4 for LSPS-PEVA. Table S1 shows the extracted diffusion coefficients D_{Li} for SE sheets containing 2.5 and 10 wt% of the various binders, respectively. For better visualization, they are depicted in Figure 5 in blue (2.5 wt%) and red (10 wt%). At first glance it is clear that the impact of binder volume on lithium ion diffusivity depends on the binder used. For HNBR and PEVA, D_{Li} decreases by roughly 15 and 44%, respectively, with a fourfold increase in binder content. In contrast, it hardly changes for PIB, considering the measurement accuracy, and even rises by roughly 29% for SBR.

To better understand the differences, these results were connected with those from EDX analysis. The elemental maps indicated a continuous film of PEVA and HNBR on the SE particles. It is thus conceivable that a larger amount of binder, which leads to thicker polymer films, hinders Li-ion transfer between particles. On the contrary, due to the granular structure of PIB and SBR, the binder quantity has less impact on Li-ion diffusion. The enhanced bonding at larger binder volume indeed rather promotes Li-ion transport at grain boundaries. For SBR, where poor adhesion requires a high binder content to yield freestanding sheets, this effect is more pronounced, resulting in a larger D_{Li} value for the 10 wt% sample. This interpretation of the trends of D_{Li} with increasing amount of binder is in line with the aforementioned findings of Inada et al., namely that a binder coating on SE particles strongly affects ionic transport, whereas granular binder domains have less impact.²⁸ The influence of binder content though has not been studied in this context.

In order to assess the absolute values for D_{Li} extracted from the PFG NMR measurements, they were first related to that of the pure LSPS powder, which was determined to $2.9 \pm 0.1 \cdot 10^{-12} \text{ m}^2 \cdot \text{s}^{-1}$. Independent from the binder type and quantity, all SE sheets yielded lower values. In general, PEVA and HNBR outperform the others at low binder content, whilst PIB and HNBR show the highest diffusivity at high binder content. For a fair comparison, however, only those values corresponding to SE sheets that formed mechanically stable layers should be taken into account. As shown in Figure 3, the minimum binder content required to obtain processible, free-standing sheets varies from binder to binder. The absolute values for 2.5 wt% PIB and HNBR should thus be compared to that for 10 wt% SBR and PEVA. Accordingly, the highest diffusion coefficient of $2.7 \pm 0.15 \cdot 10^{-12} \text{ m}^2 \cdot \text{s}^{-1}$ was yielded for HNBR, followed by PIB ($2.0 \pm 0.08 \cdot 10^{-12} \text{ m}^2 \cdot \text{s}^{-1}$), SBR ($1.8 \pm 0.15 \cdot 10^{-12} \text{ m}^2 \cdot \text{s}^{-1}$) and PEVA ($1.5 \pm 0.07 \cdot 10^{-12} \text{ m}^2 \cdot \text{s}^{-1}$). Compared to pure LSPS, addition of a polymeric binder resulted in a decrease of lithium ion diffusivity by 7% in the best and 48% in the worst case. This is in the same range as the ~7–16% drop in lithium ion conductivity reported by Lee et al. for composite films of NBR (4 wt%) and LPS vs. the pure material.¹⁸

The partial Li^+ conductivity σ_{Li} can be derived from the diffusion coefficient D_{Li} according to the Nernst-Einstein Equation 1. Here, N_{Li} is the Li-ion concentration, Q_e the unit charge, k the Boltzmann constant and T the temperature. In order to calculate the ionic conductivity, the Li-ion concentration has to be estimated first. This is usually done based on the crystal structure of the material, according to Equation 2. Here, X_{Li} is the number of Li-ions per formula unit, Z the number of formula units per unit cell and V the volume of the unit cell.

$$\sigma_{Li} = \frac{D_{Li} \cdot N_{Li} \cdot Q_e^2}{k \cdot T} \quad [1]$$

$$N_{Li} = \frac{X_{Li} \cdot Z}{V} \quad [2]$$

First, the conductivity of the pure SE material was calculated, using the NMR-derived diffusion coefficient ($2.9 \pm 0.1 \cdot 10^{-12} \text{ m}^2 \cdot \text{s}^{-1}$). The resulting ionic conductivity of $3.6 \pm 0.12 \text{ mS} \cdot \text{cm}^{-1}$ is in line with literature data ($2\text{--}5 \text{ mS} \cdot \text{cm}^{-1}$), which were obtained through AC impedance measurements as well as different ^7Li NMR techniques.^{22,24,25} This shows that the Nernst-Einstein relationship allows for a good approximation of the ionic conductivity. For a meaningful assessment of the actual conductivity of the SE/binder composites, however, the lithium diffusion length in the NMR experiments has to be larger than the radius of the SE particles. Otherwise, Li-ions would not cross grain-boundaries within the time span of the PFG NMR measurement, and the effect of the binder would thus be neglected.

A grain size of 250–300 nm is specified for LSPS by the supplier.³³ In order to confirm this, X-ray diffraction (XRD) pattern of the LSPS powder used were recorded and refined with regard to grain size. The Rietveld refinement (see Figure S5) yielded an average crystallite size of roughly 148 nm. The polymeric binder might, however, not reach each grain, but rather be located between particles. Based on the specific surface area of $1.6 \text{ m}^2 \cdot \text{g}^{-1}$, determined by BET analysis, an average primary particle size of roughly $1 \mu\text{m}$ can be estimated.³⁴ This was supported by SEM imaging of the as-received LSPS powder (Figure S6). A diffusion length $d_{diff} > 0.5 \mu\text{m}$ would thus be desirable. It can be calculated as $(n \cdot D_{Li} \cdot t_{diff})^{0.5}$ with n being dimensionality of the motion and t_{diff} the diffusion time.³⁵ As LSPS is a 3D Li-ion conductor,³⁶ n equals to 6. The resulting d_{diff} of roughly $1.3 \mu\text{m}$ is much larger than the radius of the LSPS grains and still sufficiently larger than the radius of the primary particles.

Besides, two additional facts support the assumption that Li-ions are transported across grain-boundaries during the PFG NMR measurement. Firstly, the estimated ionic conductivity of the pure SE material matches the value reported for the total conductivity, while a significantly higher value would be expected for the intergrain

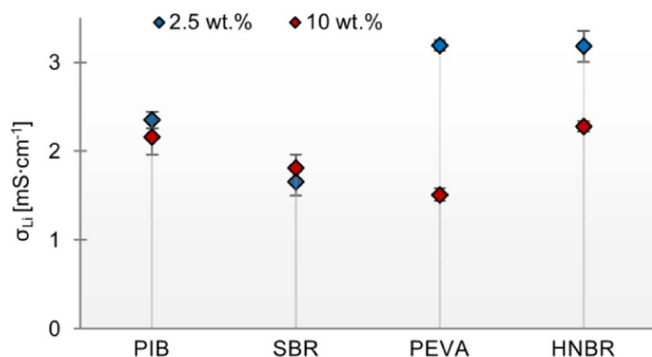


Figure 6. Estimated ionic conductivity for calendered SE sheets comprising 2.5 wt% (blue) and 10 wt% (red) PIB, SBR, PEVA and HNBR, respectively, at 30°C. Error bars indicate the measurement accuracy, taking error propagation into account.

conductivity.²² Secondly, different values for D_{Li} were extracted for the different binder types and volumes, all of them lower than that for pristine LSPS. If diffusion would solely take place within single SE particles, binder type and weight fraction would, however, not affect the measured diffusion coefficients. Hence, PFG NMR is suitable to probe the conductivity of the composite sheets without neglecting the binder impact. In order to account for the lithium-free volume though it is necessary to recalculate the Li-ion concentration by integrating the volume fraction of the SE into Equation 2:

$$N'_{Li} = (100\% - \text{Vol}\%_{\text{Binder}}) \cdot N_{Li} \quad [3]$$

The ionic conductivity can then be calculated using Equations 1 and 3. Figure 6 depicts the results for the different SE sheets containing 2.5 (blue) and 10 wt% (red) binder, respectively. A rise in conductivity with binder content is only observed for SBR. The increase by roughly 10% can again be attributed to the better adhesion between particles, resulting in a lower porosity around 30% for the 10 wt% compared to roughly 57% for the 2.5 wt% sheet. Apparently, poor adhesion is in this case more limiting than restricted ionic pathways due to blocking by greater amounts of polymeric binder. A similar observation has been made by Rosero-Navarro et al, who reported an increase in conductivity when incorporating ethyl cellulose in a $\text{Li}_6\text{PS}_5\text{Cl}$ pellet.¹⁴ In contrast, a fourfold binder content results in reduced conductivity for the other binders by roughly 10–50%. Restriction of ionic pathways seems to be the limiting factor in the case of PIB, PEVA and HNBR. This is in line with the considerably lower porosity of the respective SE sheets compared to SBR (see Figure 3), which indicates that adhesion is not a major issue with these polymers.

As in the case of the diffusion coefficients, the required binder content to obtain mechanically stable layers should be considered when assessing the absolute values. Accordingly, the estimated ionic conductivity for 2.5 wt% PIB and HNBR should be compared to that for 10 wt% SBR and PEVA. The highest conductivity of $3.2 \pm 0.18 \text{ mS} \cdot \text{cm}^{-1}$ was thus obtained for HNBR, followed by PIB ($2.4 \pm 0.09 \text{ mS} \cdot \text{cm}^{-1}$), SBR ($1.8 \pm 0.15 \text{ mS} \cdot \text{cm}^{-1}$) and PEVA ($1.5 \pm 0.07 \text{ mS} \cdot \text{cm}^{-1}$). In line with previous reports, stating that incorporation of a polymeric binder leads to a reduced ionic conductivity,^{4,7,9,14,19} all values level below that of pure LSPS ($3.6 \pm 0.12 \text{ mS} \cdot \text{cm}^{-1}$). The conductivity is reduced by roughly 12% in the best and 58% in the worst case. As mentioned, a comparable decrease of the ionic conductivity of composite films vs. the pure SE has been reported by Lee et al.¹⁸ They found that incorporation of 4 wt% NBR and butadiene, respectively, leads to a drop by roughly 7–27%. When using 5.5 wt% NBR in a LPS sheet, Oh et al. maintained ~50% of the ionic conductivity.¹⁹ Comparable results were shown by Rosero-Navarro et al. for a composite of $\text{Li}_6\text{PS}_5\text{Cl}$ and ethyl cellulose.¹⁴ The group of Jung et al. demonstrated that even the application of a polymer scaffold that makes up 14 wt% lowers the conductivity only by a factor of roughly 3.6.²⁰ Since all estimated ionic

conductivities in this contribution lie in the mS range, the composite sheets prove to be suitable for application in ASSBs.

The respective ionic conductivity obtained through electrochemical impedance spectroscopy (EIS), however, might be lower since contacting issues are less pronounced in PFG NMR measurements. More precisely, PFG NMR only probes Li-ion diffusion between interconnected particles. The impact of porosity, however, is neglected. Additional effects specific to EIS measurements result from the interface between the SE sheet and the current collector. Pores as well as polymeric binder at the surface lead to a lower effective contacting area. As the measured resistance is normalized to the area, considering only the geometric dimensions of the sample, the conductivity is usually underestimated. Due to the high sensitivity of EIS to sample preparation and contacting, a more reliable comparison of the SE sheets with different binder types and volumes is achieved using PFG NMR. On the other hand, the EIS derived conductivity might be more relevant in an actual ASSB, where contacting issues are not negligible. In order to compare the two methods, an exemplary EIS measurement was performed of a LSPS sheet with 2.5 wt% HNBR (Figure S7). Fitting of the data yielded an ionic conductivity of roughly $0.3 \text{ mS} \cdot \text{cm}^{-1}$, being an order of magnitude lower than that estimated from PFG NMR. Beside the aforementioned effects attributed to EIS, blocking of certain conduction pathways by a thick HNBR film might be responsible for the significant drop in total conductivity. This is again in line with the report from Inada et al., who observed that a continuous binder film covering SE particles remarkably hinders ionic transport.²⁸ However, as stated by the group of Jung et al.,^{19,37} an ionic conductivity in the $10^{-4} \text{ S} \cdot \text{cm}^{-1}$ range is still sufficiently high for application in ASSBs.

Discussion

In the present study we investigated five different polymers with regard to their suitability as binders for processing thin and free-standing SE layers with low porosity. All polymers fulfilled the basic requirements, namely solubility in toluene, negligible electronic conductivity and chemical stability in contact with the SE. Our extended slurry-processing study revealed that the optimal process parameters for the fabrication of SE sheets strongly depend on the used binder. Viscosity as well as binder content have to be adapted from case to case. Furthermore, some general trends could be identified. A correlation was found between the required minimum amount of binder and the molecular weight of the polymer. The higher the molecular weight, the less binder is needed. Number and type of functional groups attached to the polymer backbone are further determinants of the quality of the SE sheets. Cohesive forces between the slurry components compete with adhesive forces between slurry and carrier foil. Consequently, combination of a non-polar polymer backbone with a moderate amount of attached polar functional groups was found to be most effective. Bulky side groups, however, seem to hinder intense adhesion of the binder to the SE particles. This leads to larger quantities required for obtaining mechanically stable layers, as well as poorer bending properties of the sheets.

Considering our findings, the following properties should be pursued beyond the aforementioned basic requirements when searching for an ideal binder for sulfide-based SEs: (i) high molecular weight to minimize the required binder content, (ii) soft texture to improve densification properties, (iii) fully saturated hydrocarbon backbone to reduce stiffness and (iv) small polar functional groups (e.g. nitrile) to enhance interaction with SE particles without introducing steric hindrance. Among these characteristics, considered choice of proper side groups seems to be the most important one. As sulfur atoms are known to strongly interact with one another (sulfur bridge), an even better adhesion compared to HNBR might be achieved when using sulfur-containing polymers. A broad overview in this context has been provided by Goethals et al., covering information about chemical reactivity, softening properties, thermal stability and commercial availability.³⁸ Diez et al. showed that electrically insulating sulfur copolymers can be adjusted with regard to mechanical and thermal

properties.³⁹ Successful application of sulfur-containing polymers has already been reported for Li-S batteries⁴⁰ as well as fuel cells.⁴¹ It would thus be worth testing their suitability as polymeric binders in SE layers for ASSBs in future studies.

The most important characteristic that determines whether a SE sheet is applicable in ASSBs is its ionic conductivity. We performed ⁷Li PFG NMR measurements to study the impacts of binder type and content on conductivity. In general, all LSPS sheets yielded lower NMR-derived conductivities than the pure SE powder. The best results were obtained for those binders that formed freestanding sheets already at a low content of 2.5 wt%. Apparently, the better the properties of the polymer, meaning high adhesive strength and high deformability, the lower is its influence on Li-ion diffusivity. Apart from that, the ionic conductivity is affected by binder quantity to a greater or lesser extent, depending on the distribution pattern of the binder. It seems that a polymer coating on the SE particles is more detrimental to Li-ion diffusion than granular binder domains between the SE particles. Generally speaking, a lower binder weight fraction results in a higher conductivity, as restriction of ionic pathways increases with binder content. This applies, however, only as long as sufficient polymer is present to ensure proper adhesion between the SE particles. Once limited adhesive properties become the restraining factor, conductivity will drop with decreasing binder content. For the most promising SE/binder composite with 2.5 wt% HNBR, the ionic conductivity of the composite sheet was also determined by impedance under blocking conditions. While the EIS-derived conductivity was roughly 10 fold lower ($\sim 0.3 \text{ mS} \cdot \text{cm}^{-1}$, see Figure S6) than the NMR-derived conductivity ($\sim 3.2 \text{ mS} \cdot \text{cm}^{-1}$, see Figure 6), most likely caused by the effect of insulating polymer films in between the SE particles, a conductivity of $0.3 \text{ mS} \cdot \text{cm}^{-1}$ would still be sufficiently high for application in ASSBs.

Conclusions

In summary, we showed that both the type and the amount of the used binder strongly affects the resulting properties of SE/polymer composite sheets with regards to homogeneity, porosity, mechanical stability and ionic conductivity. Among the tested polymers, HNBR showed the best results, followed by PIB and PEVA. Due to the large amount of binder required and the poor mechanical properties of the resulting SE sheet, SBR seems to be rather unsuitable as binder. PMMA can be completely excluded as processing was not possible. This study emphasizes the necessity of a careful selection of the binder for slurry-based processing of SE sheets. While a poor choice might lead to mechanically unstable layers, a well selected binder allows for fabrication of dense and flexible SE sheets with sufficiently high ionic conductivity to be applied in ASSBs. Although we could only investigate a limited number of polymers, the observed general trends should provide a guideline for binder selection beyond the materials employed herein. In future studies, the fabricated SE sheets will be tested in sheet-type ASSB cells to confirm their suitability.


Acknowledgment

The authors thank the BMW AG for the financial support of this work. Kathrin Moser and Nicolas Billot from the Institute for Machine Tools and Industrial Management (*ivb*) of the TU München are greatly acknowledged for their support with the Mandrel Bend Tests. We thank Christian Sedlmeier from the Chair of Technical Electrochemistry (TEC) of the TU München for his support with the impedance measurements, using a measurement cell designed by Tanja Zünd and Johannes Landesfeind from TEC.

ORCID

Nathalie Riphaut  <https://orcid.org/0000-0001-5860-1106>

Sylvio Indris  <https://orcid.org/0000-0002-5100-113X>

Stefan J. Sedlmaier  <https://orcid.org/0000-0002-5337-3076>

References

1. D. Andre, H. Hain, P. Lamp, F. Maglia, and B. Stiaszny, *J. Mater. Chem. A*, **5**(33), 17174 (2017).
2. F. Mizuno, C. Yada, and H. Iba, in *Lithium-Ion Batteries*, p. 273, Elsevier B.V. (2014).
3. J. Janek and W. G. Zeier, *Nat. Energy*, **1**(9), 16141 (2016).
4. A. Sakuda, K. Kuratani, M. Yamamoto, M. Takahashi, T. Takeuchi, and H. Kobayashi, *J. Electrochem. Soc.*, **164**(12), A2474 (2017).
5. M. Yamamoto, M. Takahashi, Y. Terauchi, Y. Kobayashi, S. Ikeda, and A. Sakuda, *J. Ceram. Soc. Japan*, **125**(5), 391 (2017).
6. K. Kerman, A. Luntz, V. Viswanathan, Y.-M. Chiang, and Z. Chen, *J. Electrochem. Soc.*, **164**(7), A1731 (2017).
7. Y. J. Nam, D. Y. Oh, S. H. Jung, and Y. S. Jung, *J. Power Sources*, **375**, 93 (2018).
8. J. Schnell, T. Günther, T. Knoche, C. Vieider, L. Köhler, A. Just, M. Keller, S. Passerini, and G. Reinhart, *J. Power Sources*, **382**, 160 (2018).
9. M. Yamamoto, Y. Terauchi, A. Sakuda, and M. Takahashi, *Sci. Rep.*, **8**(1), 1212 (2018).
10. W. Weppner, in *Encyclopedia of Electrochemical Power Sources*, p. 162, Elsevier B.V. (2009).
11. C. Cao, Z.-B. Li, X.-L. Wang, X.-B. Zhao, and W.-Q. Han, *Front. Energy Res.*, **2**(Part 1), 947 (2014).
12. J. B. Goodenough and P. Singh, *J. Electrochem. Soc.*, **162**(14), A2387 (2015).
13. F. Han, T. Gao, Y. Zhu, K. J. Gaskell, and C. Wang, *Adv. Mater.*, **27**(23), 3473 (2015).
14. N. C. Rosero-Navarro, T. Kinoshita, A. Miura, M. Higuchi, and K. Tadanaga, *Ionics*, **23**(6), 1619 (2017).
15. Y. Kato, S. Hori, T. Saito, K. Suzuki, M. Hirayama, A. Mitsui, M. Yonemura, H. Iba, and R. Kanno, *Nat. Energy*, **1**(4), 16030 (2016).
16. N. Kamaya, K. Homma, Y. Yamakawa, M. Hirayama, R. Kanno, M. Yonemura, T. Kamiyama, Y. Kato, S. Hama, K. Kawamoto, and A. Mitsui, *Nat. Mater.*, **10**(9), 682 (2011).
17. Y. Seino, T. Ota, K. Takada, A. Hayashi, and M. Tatsumisago, *Energy Environ. Sci.*, **7**(2), 627 (2014).
18. K. Lee, S. Kim, J. Park, S. H. Park, A. Coskun, D. S. Jung, W. Cho, and J. W. Choi, *J. Electrochem. Soc.*, **164**(9), A2075 (2017).
19. D. Y. Oh, D. H. Kim, S. H. Jung, J.-G. Han, N.-S. Choi, and Y. S. Jung, *J. Mater. Chem. A*, **5**(39), 20771 (2017).
20. Y. J. Nam, S.-J. Cho, D. Y. Oh, J.-M. Lim, S. Y. Kim, J. H. Song, Y.-G. Lee, S.-Y. Lee, and Y. S. Jung, *Nano Lett.*, **15**(5), 3317 (2015).
21. S. Ito, S. Fujiki, T. Yamada, Y. Aihara, Y. Park, T. Y. Kim, S.-W. Baek, J.-M. Lee, S. Doo, and N. Machida, *J. Power Sources*, **248**, 943 (2014).
22. P. Bron, S. Johansson, K. Zick, Schmedt auf der Günne, Jörn S. Dehnen, and B. Rölling, *J. Am. Chem. Soc.*, **135**(42), 15694 (2013).
23. S. P. Ong, Y. Mo, W. D. Richards, L. Miara, H. S. Lee, and G. Ceder, *Energy Environ. Sci.*, **6**(1), 148 (2013).
24. M. Kaus, H. Stöfler, M. Yavuz, T. Zinkevich, M. Knapp, H. Ehrenberg, and S. Indris, *J. Phys. Chem. C*, **121**(42), 23370 (2017).
25. I. Tarhouchi, V. Viallet, P. Vinatier, and M. Ménétrier, *Solid State Ionics*, **296**, 18 (2016).
26. R. Kanno and M. Murayama, *J. Electrochem. Soc.*, **148**(7), A742 (2001).
27. International Chemical Society Cards (ICSC); *toluene 0078*.
28. T. Inada, K. Takada, A. Kajiyama, M. Kouguchi, H. Sasaki, S. Kondo, M. Watanabe, M. Murayama, and R. Kanno, *Solid State Ionics*, **158**(3-4), 275 (2003).
29. B.-R. Lee and E.-S. Oh, *J. Phys. Chem. C*, **117**(9), 4404 (2013).
30. Y. J. Choi, D. H. Shin, S. H. Kim, S. C. Park, G. B. Cho, and K. W. Kim, *Solid State Phenom.*, **124-126**, 1007 (2007).
31. A. Sakuda, A. Hayashi, and M. Tatsumisago, *Sci. Rep.*, **3**, 2261 (2013).
32. E. C. Bucharsky, K. G. Schell, A. Hintennach, and M. J. Hoffmann, *Solid State Ionics*, **274**, 77 (2015).
33. NEI Corporation, NANOMYTE[®] SSE-10 (LSPS) Specification Sheet, https://neicorporation.com/specs/SSE-10_Spec_Sheet_%28LSPS%29.pdf 2016.
34. Y. Waseda and A. Muramatsu, *Morphology Control of Materials and Nanoparticles: Advanced Materials Processing and Characterization*, Berlin, Heidelberg, Springer 2004.
35. W. S. Price, *Concepts Magn. Reson.*, **9**(5), 299 (1997).
36. D. A. Weber, A. Senyshyn, K. S. Weldert, S. Wenzel, W. Zhang, R. Kaiser, S. Berendts, J. Janek, and W. G. Zeier, *Chem. Mater.*, **28**(16), 5905 (2016).
37. K. H. Park, D. Y. Oh, Y. E. Choi, Y. J. Nam, L. Han, J.-Y. Kim, H. Xin, F. Lin, S. M. Oh, and Y. S. Jung, *Adv. Mater.*, **28**(9), 1874 (2016).
38. E. J. Goethals and J. Macromol, *Sci., Part C: Polym. Rev.*, **2**(1), 73 (1968).
39. S. Diez, A. Hoefling, P. Theato, and W. Pauer, *Polymers*, **9**(12), 59 (2017).
40. X.-G. Yu, J.-Y. Xie, J. Yang, H.-J. Huang, K. Wang, and Z.-S. Wen, *J. Electroanal. Chem.*, **573**(1), 121 (2004).
41. J. S. Choi, A. K. Mishra, N. H. Kim, G. Shin, and J. H. Lee, *J. Appl. Electrochem.*, **43**(8), 749 (2013).

Supporting Information

Slurry-based Processing of Solid Electrolytes – A Comparative Binder Study

Nathalie Riphaus,^{*,a,b} Philipp Strobl,^{a,b} Barbara Stiaszny,^b Tatiana Zinkevich,^{c,d} Murat Yavuz,^c Joscha Schnell,^e Sylvio Indris,^{c,d} Hubert A. Gasteiger,^a Stefan J. Sedlmaier^b

^a Chair of Technical Electrochemistry, Department of Chemistry and Catalysis Research Center, Technische Universität München, 85748 Garching, Germany

^b BMW Group, 80809 München, Germany

^c Institute for Applied Materials – Energy Storage Systems, Karlsruhe Institute of Technology, 76344 Eggenstein-Leopoldshafen, Germany

^d Helmholtz Institute Ulm, 89081 Ulm, Germany

^e Institute for Machine Tools and Industrial Management, Technische Universität München, 85748 Garching, Germany

E-mail:

nathalie.riphaus@tum.de

Index:

1. Linear sweep voltammetry (LSV) measurements of pure binder films.
2. Fourier transform infrared spectroscopy (FTIR) of SE sheets.
3. X-ray photoelectron spectroscopy (XPS) of SE sheets.
4. ⁷Li PFG NMR measurements of calendered SE sheets.
5. X-ray diffraction (XRD) measurement of the as-received LSPS powder.
6. Scanning electron micrograph (SEM) of the as-received LSPS powder.
7. Electrochemical impedance spectroscopy (EIS) of a calendered LSPS-HNBR sheet.

1. Linear sweep voltammetry (LSV) measurements of pure binder films

LSV measurements were performed in order to probe the electronic conductivity of binder films. As exemplarily shown for PIB in Figure S1a, the PIB, SBR and PMMA layers showed no current flow over the voltage range of 0 – 5 V. With PEVA and HNBR, in contrast, a low current of up to 45 nA was detected (shown for PEVA in Figure S1b). All binders though proved to be electrochemically stable in the applied voltage range as no current peaks were observed during the LSV. The electronic conductivity of PEVA and HNBR layers, determined by chronoamperometry measurements, was found to be in the range of $10^{-11} \text{ S}\cdot\text{cm}^{-1}$.

Experimental. For fabrication of pure binder layers, the polymer was dissolved in toluene at a solids content of 10 wt.%. The slurry was then casted on siliconized polyester foil (PPI Adhesive Products GmbH) using the doctor blade technique. After drying at ambient conditions, binder layers with a thickness of 15 – 30 μm were obtained. Electrochemical tests were performed in TSC battery cells (RHD instruments) using stainless steel current collectors. For LSV measurements, the potential was increased from 0 – 5 V at a scan rate of 1 mV/s and the respective current response was recorded. Measurements were conducted at 20, 40 and 60 °C, with a resting time of 2 hours prior to each scan.

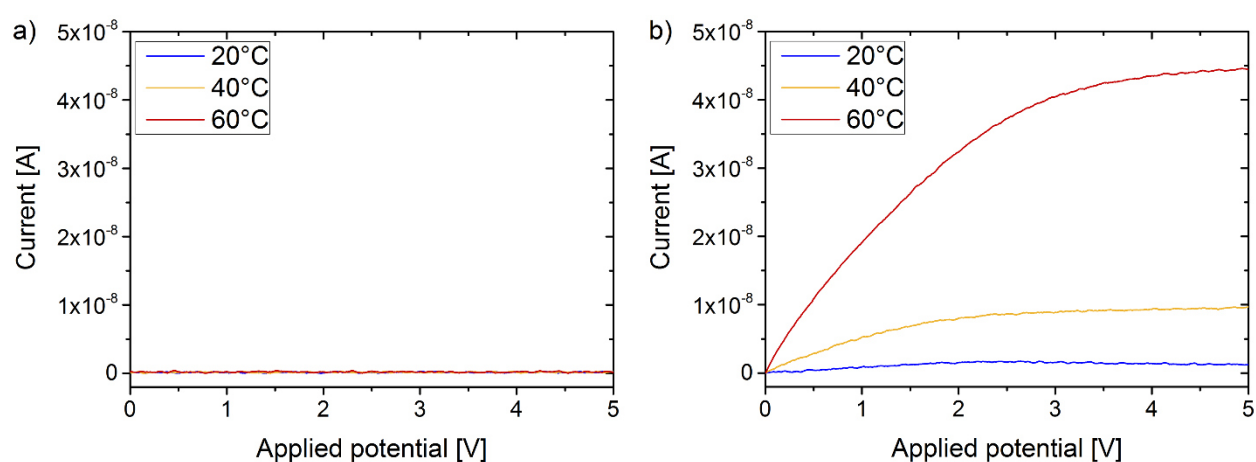


Figure S1. LSV measurements of a PIB layer (a) and a PEVA layer (b) at 20 °C (blue), 40 °C (yellow) and 60 °C (red).

2. Fourier transform infrared spectroscopy (FTIR) of SE sheets.

FTIR measurements were conducted to probe the chemical stability of the different binders with LSPS. SE sheets with a LSPS : binder ratio of 90 : 10 wt.% were prepared and their FTIR spectra were compared to those of the pristine materials. As exemplarily shown in Figure S2 for PEVA, all bands in the spectrum of the SE sheet can be assigned to the binder and the SE, respectively. In order to provoke possible decomposition reactions, the sheets were then stored for prolonged time at 60 °C. As the overlay in Figure S2 demonstrates, the spectrum after aging was identical to that of the as-prepared SE sheet and no additional bands were detected. The same was observed for the other binders, indicating their chemical stability towards LSPS.

Experimental. Materials were investigated by FTIR inside the glovebox. The SE sheets were delaminated from the Mylar foil and placed in the Spectrum Two spectrometer (Perkin Elmer). To probe the pure materials, the as-received LSPS powder and polymers were used. Spectra were recorded from 4000 – 380 cm^{-1} at a MIRacle Germanium ATR (Pike Technologies) incorporated in the spectrometer.

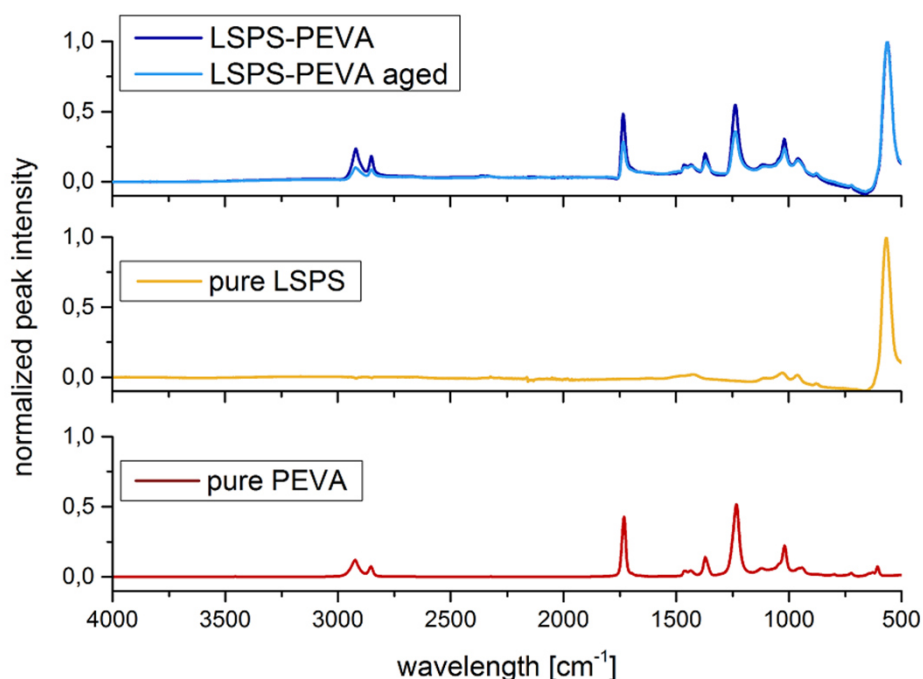


Figure S2. FTIR spectra of pure PEVA (red), pure LSPS (yellow) and a LSPS-PEVA (90:10 wt.%) sheet after fabrication (blue) and after aging for six weeks at 60 °C (light blue).

3. X-ray photoelectron spectroscopy (XPS) of SE sheets.

Besides FTIR, XPS analysis of the aforementioned SE sheets was performed to further probe the chemical stability of the different binders with LSPS. Likewise the FTIR spectra, XPS spectra of the as-prepared as well as the aged SE sheets were compared to those of the pristine materials. Figure S3 shows the overlay of the S 2p spectra of pristine LSPS and an aged LSPS-PIB sheet, demonstrating that no changes occurred during fabrication and aging. The same was observed for the other binders, confirming their chemical stability towards LSPS.

Experimental. Samples were mounted floating on a stainless steel sample holder (15 mm diameter), which was then transferred from the glovebox into the load lock of the XPS system without air exposure using a transfer vessel (Kratos). XPS spectra were recorded with an Axis Supra system (Kratos) using monochromatic Al K α radiation ($h\nu = 1486.6$ eV) in hybrid lens mode with the instrument's charge neutralizer turned on. Sputtering was performed using an argon ion cluster gun at an acceleration voltage of 10 kV and an argon ion current of 1 μ A. The obtained spectra were processed and fitted using the ESCApe software (Kratos, version 1.1). Binding energies were corrected based on the C-C/C-H peak of adventitious carbon at 284.8 eV in the C 1s spectrum. A mixture of 30% Lorentzian and 70% Gaussian functions was used for the least-squares curves fitting procedure utilizing a Shirley background subtraction.

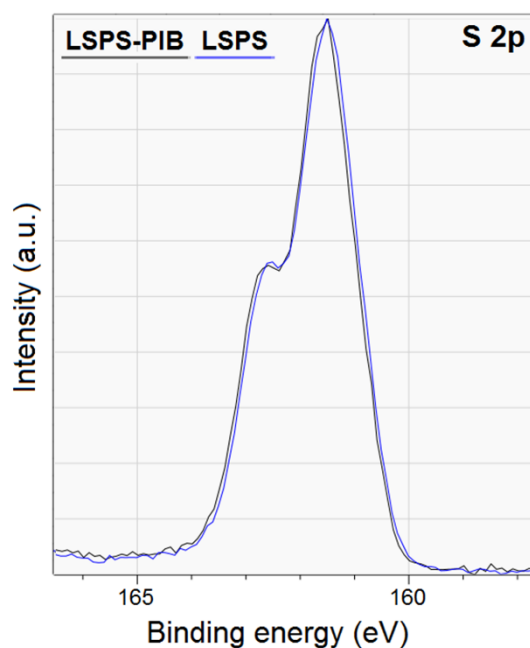


Figure S3. Overlay of the XPS S2p spectra of pure LSPS (blue) and an LSPS-PIB (90:10 wt.%) sheet aged at 60 °C for six weeks (black).

4. ^7Li PFG NMR measurements of calendered SE sheets.

^7Li PFG NMR experiments were performed to evaluate the Li-ion diffusivity in calendered SE sheets with different binder types and contents. Figure S4 shows an exemplary echo damping versus gradient strength plot for LSPS-PEVA sheets with 2.5 (black) and 10 wt.% (red) binder content. The extracted diffusion coefficients D_{Li} for the various SE sheets containing 2.5 and 10 wt.% of the different binders, respectively, are given in Table S1. The diffusion coefficient for pure LSPS powder was determined to $2.9 \pm 0.1 \cdot 10^{-12} \text{ m}^2 \cdot \text{s}^{-1}$. Hence, all SE sheets yielded lower values than the pure SE, independent from the binder type and quantity.

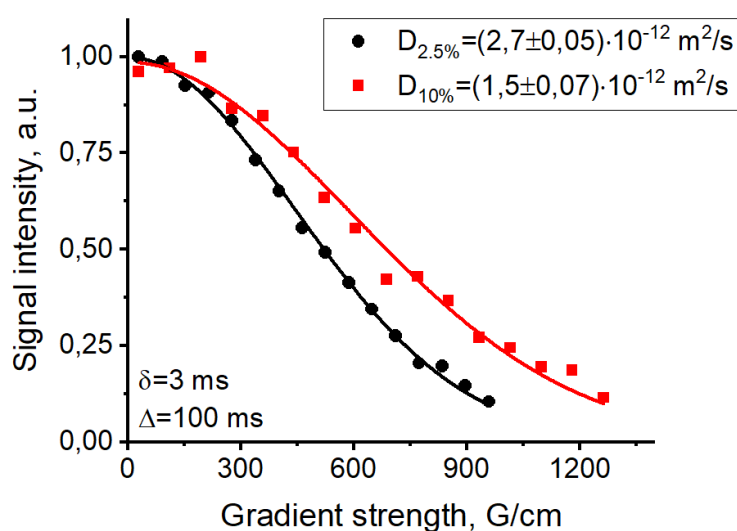


Figure S4. Echo damping versus gradient strength plot, obtained by ^7Li PFG NMR experiments of calendered LSPS-PEVA sheets with 2.5 (black) and 10 wt.% (red) binder at 303 K.

Table S1. Li-ion diffusion coefficients D_{Li} of calendered SE sheets comprising 2.5 and 10 wt.% PIB, SBR, PEVA and HNBR, respectively, extracted from ^7Li PFG NMR measurements.

Binder	PIB	SBR	PEVA	HNBR
D_{Li} at 2.5 wt.% [$10^{-12} \text{ m}^2 \cdot \text{s}^{-1}$]	2.0 ± 0.08	1.4 ± 0.13	2.7 ± 0.05	2.7 ± 0.15
D_{Li} at 10 wt.% [$10^{-12} \text{ m}^2 \cdot \text{s}^{-1}$]	2.2 ± 0.20	1.8 ± 0.15	1.5 ± 0.07	2.3 ± 0.06

5. X-ray diffraction (XRD) measurement of the as-received LSPS powder.

The as-received LSPS powder was investigated by means of XRD in order to assess the grain size. The Rietveld refinement yielded an average crystallite size of roughly 148 nm. As Figure S5 shows, not only LSPS but also a small fraction of Li_7PS_6 was detected. This argyrodite side phase of commercially available LSPS has also been reported by Kaus et al.¹

Experimental. The powder sample was measured in a sealed glass capillary with a diameter of 0.5 mm. XRD was performed at a STOE STADI/P powder diffractometer, using Mo $\text{K}\alpha 1$ radiation ($\lambda = 0.7093 \text{ \AA}$), a Ge(111) monochromator and a Debye-Scherrer geometry within a 2θ range of $3 - 61^\circ$ (scan step 0.15° , time/ step 10 sec). Rietveld refinement was done using the software FullProf Suite.

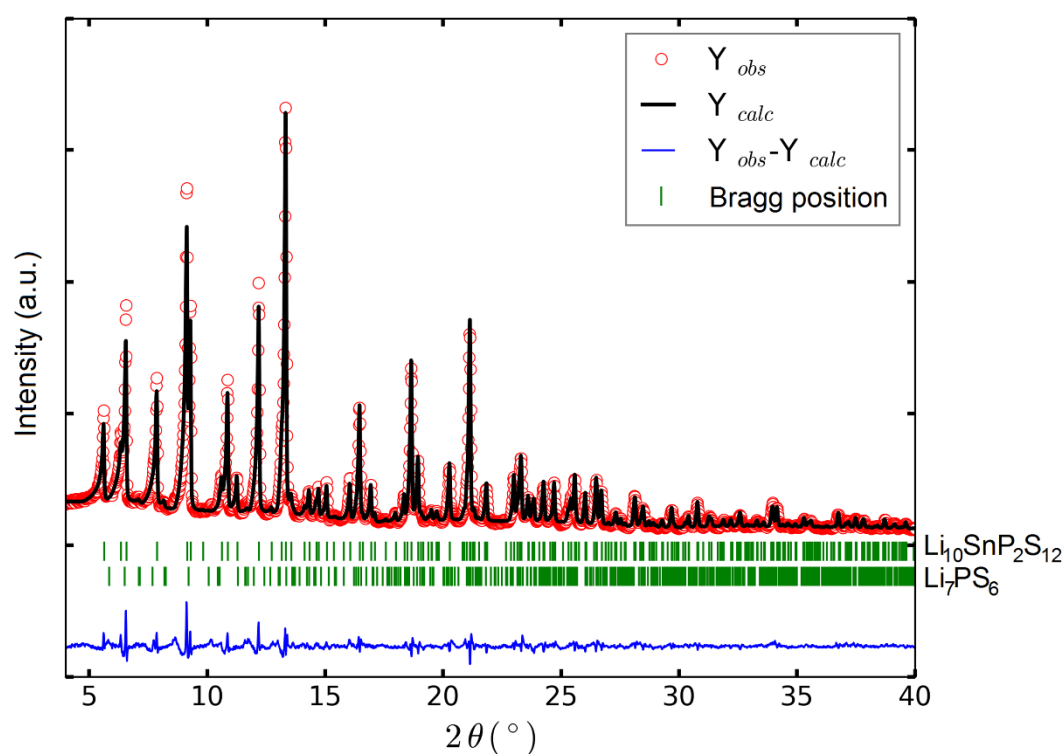


Figure S5. XRD pattern of the as-received LSPS with Rietveld refinement ($\lambda = 0.7093 \text{ \AA}$). The main phase, LSPS; was refined to 92.06%. The remaining 7.94% were assigned to Li_7PS_6 .

¹ M. Kaus, H. Stöffler, M. Yavuz, T. Zinkevich, M. Knapp, H. Ehrenberg and S. Indris, *J. Phys. Chem. C* **2017**, *121* (42), 23370–23376.

6. Scanning electron micrograph (SEM) of the as-received LSPS powder.

SEM images of the as-received LSPS powder were recorded to confirm the average particle size of $\sim 1 \mu\text{m}$ calculated from BET measurements. As Figure S6 shows, most LSPS particles are in the range and even much smaller than $1 \mu\text{m}$, while only few larger particles can be found.

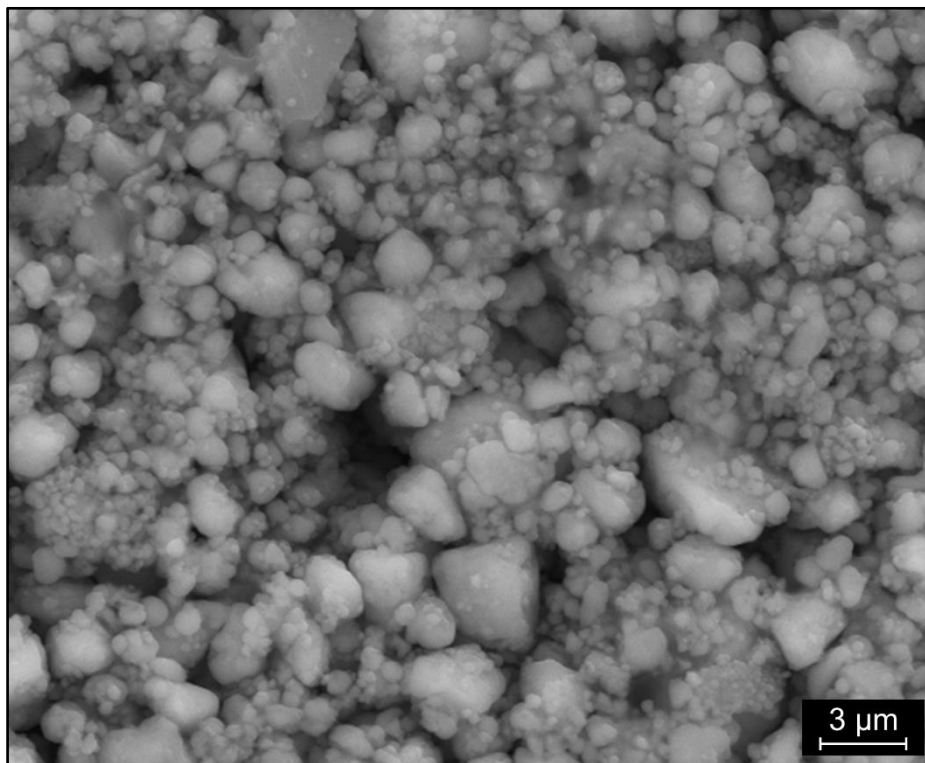


Figure S6. SEM image of the as-received LSPS powder.

7. Electrochemical impedance spectroscopy (EIS) of a calendered LSPS-HNBR sheet.

EIS of a SE sheet comprising 2.5 wt.% HNBR was performed in order to determine the Li-ion conductivity in comparison to the PFG NMR-derived value. From the width of the high-frequency semicircle ($169 \Omega \cdot \text{cm}^2$; see inset of Figure S7) and the thickness of the compressed sample ($\sim 500 \mu\text{m}$), the effective conductivity of the SE sheet is calculated to be $\sim 0.3 \text{ mS} \cdot \text{cm}^{-1}$.

Experimental. Twelve disks (8 mm diameter) were punched out from a calendered SE sheet containing 2.5 wt.% HNBR. The disks were stacked in a cell setup designed and built at TUM, comprising a PEEK cylinder, hardened stainless steel dies, and six screws that fix the setup with a torque of 40 Nm. The EIS measurement was performed with an SP300 impedance analyzer (Biologic) in a frequency range between 7 MHz and 1 Hz using an amplitude of 50 mV at 25 °C. The data were fitted using the RelaxIS software package (RHD instruments).

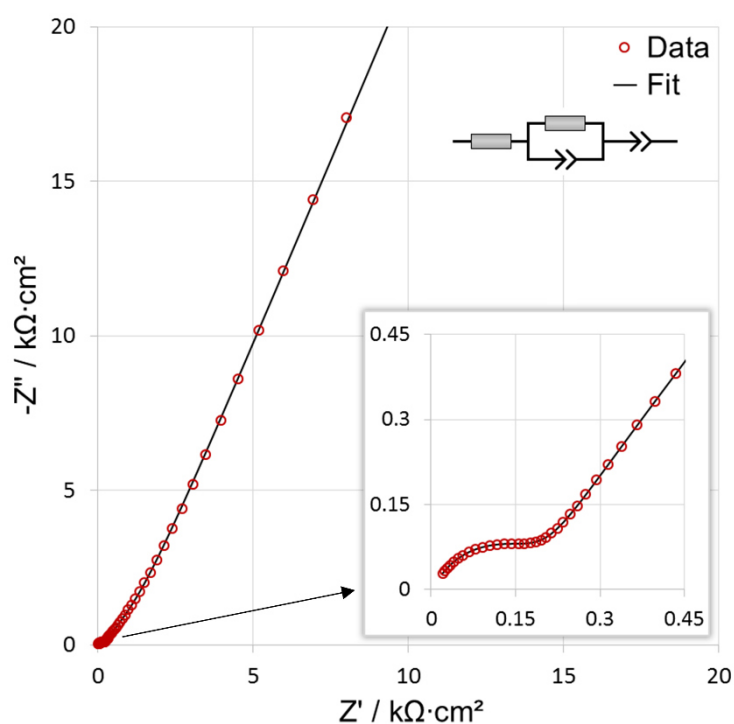


Figure S7. Nyquist diagram of the impedance of twelve stacked, compressed SE sheets with 2.5 wt.% HNBR binder at 25 °C. Experimental data are depicted as red circles, fit results as black line. The electric equivalent circuit used for fitting is shown in the top right. The inset shows the enlarged high frequency region.

3.2.2 Processing Parameters for Composite Cathodes

Building on the experience gained through the comparative binder study for LSPS-based SE sheets, slurry-based processing of composite cathodes was examined in the last part of this thesis. As discussed in detail in chapter 1.3, the larger number of components in a composite cathode compared to a solid electrolyte layer implies a much higher complexity. One important aspect is homogeneous distribution of all components to optimize electronic and ionic percolation and thereby access the full capacity of the cathode.^{14,19} This also implies good physical contacting and minimal porosity.^{18,39} Maintenance of the interfacial contacts during cycling is another challenge to be met, as intercalation materials exhibit volume changes during lithiation and delithiation.^{14,115,132} Recent publications demonstrated that these problems can be reduced if slurry-processed composite cathodes are used.^{40,64,65} This might be an effect of the flexible binder, which enhances mechanical stability as well as adhesion to the current collectors. Full capacity though was still not achieved in these studies.

The focus in this thesis was therefore set on percolation properties of slurry-processed composite cathodes. The effects of different process parameters on the homogeneity of the resulting cathode sheet were investigated. In particular, the ionic and electronic percolation was evaluated as a function of the type of binder and the processing conditions. A constant composition of 68.1 wt.% NMC-622, 29.2 wt.% LSPS, 1.3 wt.% CNF and 1.4 wt.% binder was used, following a recipe of Nam et al.⁶⁵ As described in chapter 2.3, the fabrication process included (i) premixing of NMC and LSPS using mortar and pestle, (ii) dispersing the CNF in the binder solution, (iii) adding the NMC/LSPS mixture to the CNF/binder dispersion and stirring the slurry, (iv) coating the slurry on aluminum foil using the doctor blade technique and (v) densification of the cathode sheet. The type of binder used and the premixing steps as well as the mixing procedure were varied, while toluene was used as the solvent.

First, the impact of the viscosity of the slurry was evaluated. The important process parameter in this context is the concentration of the initial binder solution, which also determines the final solids content of the slurry. The most promising binders identified during the previous study, namely polyisobutene (PIB) and hydrogenated nitrile butadiene rubber (HNBR),¹³¹ were tested at different concentrations between 0.5 – 3.0 wt.%, corresponding to roughly 26 – 59 wt.% final solids content.

Figure 3.7 presents SEM images and EDX maps of two cathode sheets after calendaring (porosity 5% and 17%). While both are based on HNBR, the same overall composition and the identical processing steps, the concentration of the initial binder solution differs. If a low amount of 1.0 wt.% is used, the cathode has a smooth surface and the components are well distributed (Figure 3.7a). In contrast, a high concentration of 3.0 wt.% results in a rough surface and strong agglomeration of the CNF, as the red region in the EDX map in Figure 3.7b demonstrates. Hence, a less concentrated binder solution seems to be beneficial for homogeneous distribution.

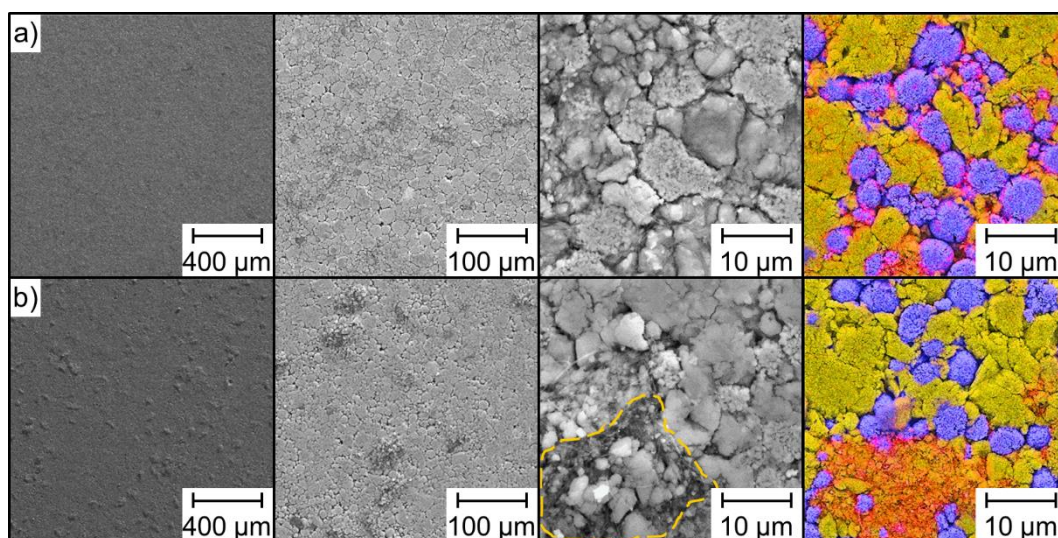


Figure 3.7. SEM images and EDX maps (blue: Ni, yellow: S, red: C) of calendared cathodes: a) 1.0 wt.% HNBR in toluene, final solids content 26%. The cathode shows a smooth surface and the components are well distributed. b) 3.0 wt.% HNBR in toluene, final solids content 50%. The cathode has a rough surface, the CNF (red) agglomerate between LSPS (yellow) and NMC (blue), also indicated by the orange frame.

Although the same trend can be observed for PIB-based cathodes, uniform distribution of CNF was not achieved even with the least concentrated solution of 1.0 wt.%. This might be attributable to the higher molecular weight or the stronger adhesion forces of PIB compared to HNBR. While these properties can be beneficial in a two-component system like the SE layer, they apparently hinder uniform blending in a more complex system such as the composite cathode. It should be recalled that the concentration of the initial binder solutions defines the viscosity of the final slurry. A low amount of binder thus results in a rather inviscid slurry. This means that even if a further diluted PIB solution might enable good distribution of CNF, the resulting slurry is not processible. Since the first results using HNBR were more promising, this binder was selected for further tests. A concentration of 1.25 wt.%, resulting in about 47 wt.% solid content of the ink, was found to be best and used subsequently.

Nam et al. reported that premixing of the CAM and SE powders yields higher capacities.⁶⁵ Two homogenization methods for the NMC/LSPS composite were therefore compared in the next step. Using mortar and pestle, the powders were either mixed dry or at the presence of a small amount of solvent. EDX analysis of the resulting cathodes revealed that the latter enables a more even spread of the components, possibly because agglomerates can be separated more easily. Lastly, the impact of the temperature during mixing of the slurry was evaluated. Stirring at 60 °C instead of ambient temperature proved to be advantageous and yielded the most homogeneous composite cathodes, as confirmed by EDX mapping. While additional analysis is required to fully assess the ionic and electronic percolation properties of the prepared cathode sheets, SEM imaging and EDX mapping gave some clear indications.

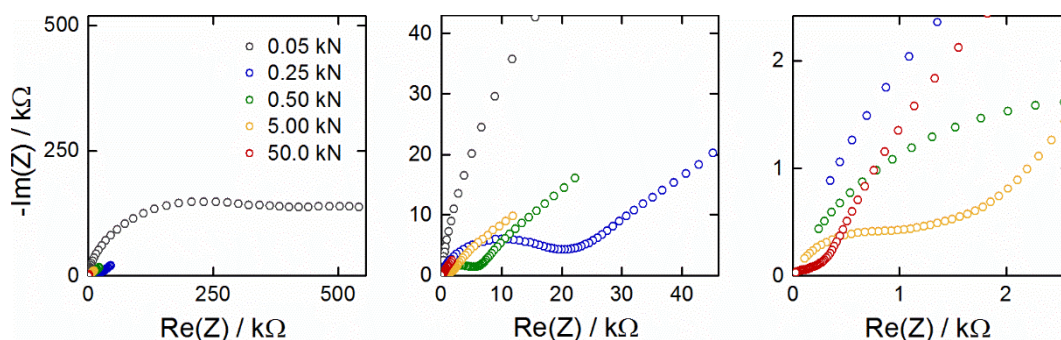


Figure 3.8. Nyquist plot of the impedance of a NMC | LSPS | NMC cell (electrode \varnothing 10 mm) as a function of the applied external force at ambient temperature. The plots show different magnifications to better visualize the various EIS spectra. The cell impedance decreases significantly with increasing pressure.

First electrochemical properties of the composite cathodes were probed by means of EIS. For this purpose, compressed cathodes were assembled in symmetrical cells comprising a slurry-processed LSPS sheet as the separator. Figure 3.8 demonstrates that the external pressure applied during the measurement has a very strong influence on cell impedance. In the TSC battery cell, which was mainly used in this thesis, less than 0.1 kN can be applied. In contrast, 50 – 500x higher compression is required to obtain reasonable resistances. While such pressures are applicable in the novel cell design of RHD instruments, which was also used for the experiments in Figure 3.8, the setup was not available for further tests in this thesis. Due to this hardware problem, EIS data were hardly reproducible and are not discussed any further. The electrochemical characterization of the cathode sheets prepared in this study thus remains a pending task that has to be tackled in the future.

4 Conclusions

The overall goal of this PhD thesis was to gain a more comprehensive understanding of the processes taking place in ASSB cells and thereby develop a possible ASSB cell design for automotive applications. Figure 4.1 summarizes the most important results. The first part focuses on the “understanding” theme of the title, more precisely on the fundamental understanding and optimization of solid-solid interfaces. The second part deals with the “design” aspect, considering manufacturing strategies for two ASSB cell components – the SES layer and the composite cathode.

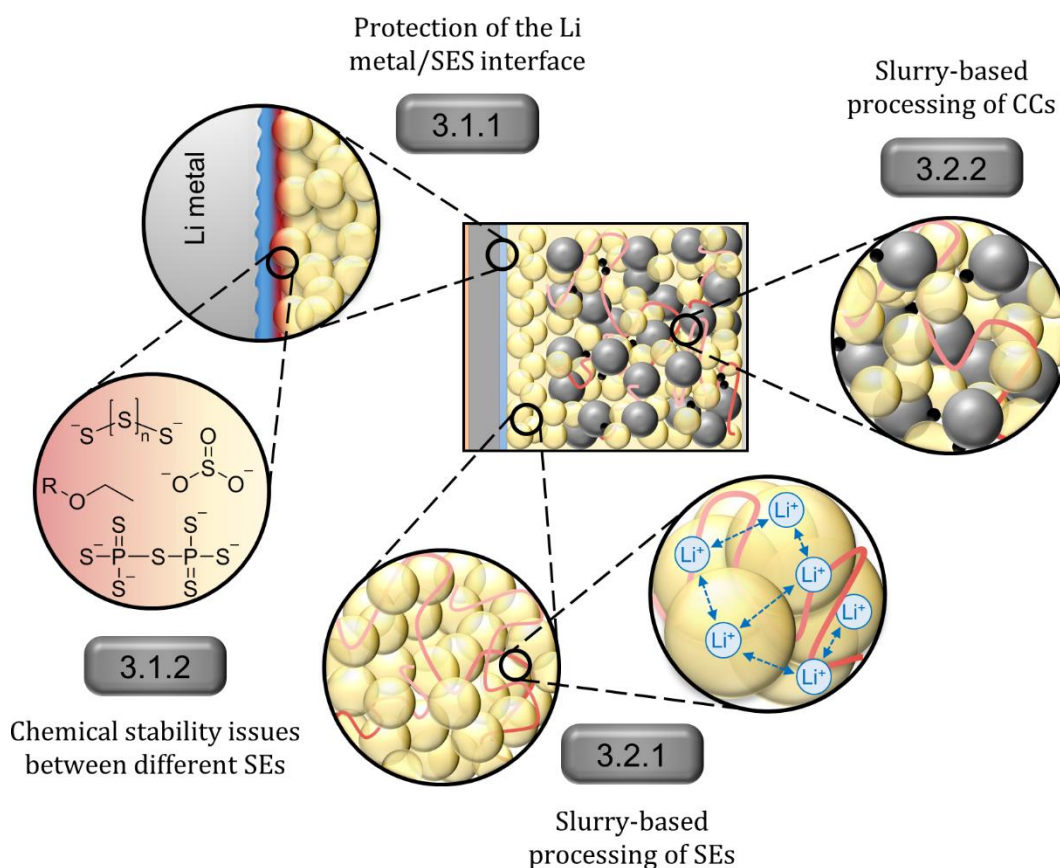


Figure 4.1. Graphical summary of the most important studies conducted in the scope of this PhD thesis. The respective sections herein are indicated by the numbers in the grey boxes. While section 3.1 focuses on a fundamental understanding and optimization of solid-solid interfaces, section 3.2 deals with manufacturing strategies for different ASSB cell components.

The first main subject of this thesis addresses the limited stability of the Li metal/SE interface. Wet-chemical pretreatment of lithium metal with different solvents did not lead to a stable interface with the solid electrolytes LATP and LSPS, respectively. In contrast, degradation of LATP was prevented by implementing thin PEO-based polymer interlayers. The same approach though resulted in continuous degradation if sulfide-based LSPS instead of oxide-based LATP was used. This observation provided the starting point for an in-depth analysis of the chemical stability between the inorganic solid electrolyte LSPS and the PEO-based solid polymer electrolyte. Electrochemical tests gave a first indication for degradation reactions taking place at the PEO/LSPS interface. Subsequent chemical analysis revealed that the decomposition products comprise P-[S]_n-P type bridged PS₄³⁻ units, polysulfides and sulfite. The degradation was found to originate from several reactions that involve the PS₄³⁻ units and surface impurities in LSPS as well as the functional groups in PEO.

The scientific relevance of this study becomes clear when noticing that polymeric interlayers are applied quite commonly at the Li metal/electrolyte interface in various cell technologies such as conventional LIBs,⁹²⁻⁹⁵ Li-air batteries^{96,97} as well as Li-based ASSBs.^{105,107,109,110,130} Particularly when sulfide-based solid electrolytes are employed, the discovered degradation reactions might become very important. Although the compatibility of two distinct solid electrolytes has been investigated in this thesis, the general observations are applicable to a wider range of materials. *Inter alia*, the study demonstrates how important a complete chemical analysis is in order to get a comprehensive picture of interfacial reactions at the material level. Furthermore, it emphasizes the relevance of investigating solid-solid interfaces not only from an electrochemical, but also from a chemical point of view. Finally, the numerous issues that were evaluated as possible origins of the degradation indicate relevant aspects to be considered when designing ASSB cells. For instance, surface impurities on the pristine materials, which might be uncritical by themselves, could cause decomposition reactions when combined with other materials in the cell.

In the second part of this PhD thesis, slurry-based processing methods to produce solid electrolyte separator layers and composite cathodes for ASSBs were probed. The motivation behind the former is rooted in the need for a scalable fabrication method for thin and flexible SES layers, which cannot be realized for large-scale applications by the current lab approach to compact the crude powder material. Desirable energy densities of ASSBs require the SES layer to have a thickness in the range of 20 – 30 μm , similar to conventional separator thicknesses in Li-ion batteries.^{18,39} Slurry-based fabrication of composite cathode sheets was intended as compression of the dry-mixed cathode components usually results in poor mechanical integrity and thus capacity fading.^{14,115,132} Contrary to the increasing demand for an ASSB cell concept for automotive applications, however, literature related to slurry-processed composite cathodes is sparse, and even less can be found concerning slurry-based fabrication of SES layers. Different polymers were therefore investigated in this thesis as potential binders for thin and flexible SE sheets based on LSPS.

Their influences on the production parameters as well as the homogeneity, density, mechanical stability and ionic conductivity of the obtained SE sheet were evaluated. Even though the amount of binder required for mechanically stable sheets as well as the solids content in the slurry had to be adapted from case to case, some general trends were identified. *Inter alia*, the minimum required binder content turned out to depend on the average molecular weight of the polymer used. More precisely, a higher molecular weight resulted in a lower minimum amount of binder. Furthermore, the amount and type of functional groups in the polymer affected the quality of the SE sheets. Owing to the competition between the cohesive forces between the slurry components and the adhesive forces between the slurry and the carrier foil, a non-polar polymer backbone in combination with a moderate number of small, polar functional groups proved to be the most suitable.

The significant differences between the SE sheets comprising the different binders highlight the key role of the binder. A poor choice might yield mechanically unstable sheets. In contrast, a well-selected binder results in thin, dense and flexible layers of sufficiently high ionic conductivity to be implemented in automotive ASSB cells. With the number of binders investigated in this study, general trends could be derived. Based on these, guidelines for a deliberate choice of the binder for sulfidic solid electrolytes beyond the materials tested in this thesis were provided.

The work on slurry processing of composite cathodes in section 3.2.2 revealed that the binder also plays a decisive role therein. A rather concentrated initial binder solution, for instance, was found to cause agglomeration of the carbon additive and might thus hamper electronic percolation in the cathode. The binder that has been identified as the most suitable for SE sheets, hydrogenated nitrile butadiene rubber, also turned out to be most appropriate for composite cathodes. Finally, electrochemical tests of the fabricated cathodes in symmetrical and full cells indicated that a high pressure exceeding 100 MPa has to be applied during testing, even if the individual cell components and the complete cell stack has been compressed before.

Besides contributing to a more comprehensive understanding of the ASSB concept, the studies conducted within this thesis shall aid to propose a possible automotive ASSB cell design. One very important aspect in this context is the high external pressure that has to be applied on the battery pack. Koerver et al. recently investigated the chemo-mechanical properties of ASSB cells, demonstrating that pressure variations are more critical in ASSBs than in conventional LIBs.¹³² Zhang et al. furthermore found that a high preload reduces the issues arising from pressure changes during cycling.¹³³ This matches the observation in this thesis that the cell stack has to be compressed not only before but also during operation. In accordance with a recent review by Ma et al., who pointed out that the properties of the SE/electrode interfaces are more relevant than those of the solid electrolyte itself,¹³⁴ the high cell resistance at low preload in this thesis was assigned to poor interfacial contacting. This is most likely also the reason why the studies on bulk-type ASSB test cells that could be cycled stable over hundreds of cycles so far were performed under high pressures of several hundred MPa.^{36,61,67,135,136} Such preloads though would mean a 100 – 1000 fold increase compared to the moderate 0.1 – 1 MPa applied in current battery packs for BEVs,¹³⁷ and will most likely not be applicable. Despite the rising awareness for the need to address the pressure-induced issues in ASSBs, strategies to reduce the required pressure load and to implement i.e. a mechanical compensation layer still have to be developed.

Beyond that, additional aspects should be considered when designing an ASSB cell. From the key performance parameters illustrated in Figure 1.4, relevant specifications like the maximum tolerable cell resistance, the minimum required conductivity of the cell components as well as their preferable layer thickness can be derived. This thesis and other recent studies showed that slurry-based production methods, which are well-established for LIB electrodes, are also applicable for the fabrication of ASSB components.^{40,41,61-68} Upscaling of these processes though is still pending. The solid electrolyte layer, for instance, has to provide uniform properties and low defect density over a large area. The desire for lower thickness to increase the energy density thereby conflicts with the required robustness against lithium dendrites. A scalable method to properly connect the SE layer with the electrodes has not yet been provided either. Furthermore, while coating of the CAM particles is a feasible option to protect the SE/CAM interface from degradation,¹¹¹⁻¹¹³ a high throughput and low cost approach to stabilize the Li metal/SE interface without impairing the cell performance still needs to be developed. The investigations on polymeric inter-layers in this thesis show that special care also has to be paid to the compatibility of the protection layer with the solid electrolyte.

In conclusion, this PhD thesis highlights several of the most essential challenges that have to be addressed to reach commercialization of bulk-type ASSB cells for automotive applications. Indeed, there is still a long way to go. Major achievements in recent years, including fundamental understanding of the processes taking place in ASSB cells, development of improved solid electrolyte materials and advanced fabrication strategies, however, increase the chances for a breakthrough of the ASSB technology. This PhD thesis should not only encourage the scientific community to follow the path, but also provide some guidance and inspiration for future studies. While numerous publications focusing on the search for even better solid electrolytes and suitable cathode compositions can be found, activities to establish the lithium metal anode and improve the mechanical properties of ASSB cells have to be intensified. Meanwhile, the rapid technological development in the field gives hope for an ongoing progress towards large-scale application of ASSBs.

References

1. BP p.l.c. BP Statistical Review of World Energy, <https://www.bp.com/content/dam/bp/business-sites/en/global/corporate/pdfs/energy-economics/statistical-review/bp-stats-review-2018-full-report.pdf> (accessed 14.04.2019).
2. Andre, D., Hain, H., Lamp, P., Maglia, F., Stiaszny, B. Future High-Energy Density Anode Materials from an Automotive Application Perspective. *J. Mater. Chem. A* **2017**, *5*, 33, 17174–17198.
3. National Renewable Energy Laboratory. At A Glance: Electric-Drive Vehicles: *DOE/GO-102016-4867*: Golden **2016**.
4. BMW Group. The new 2019 BMW i3 120Ah., https://www.press.bmwgroup.com/usa/article/detail/T0285420EN_US/the-new-2019-bmw-i3-120ah-and-i3s-120ah (accessed 20.11.2018).
5. Andre, D., Kim, S.-J., Lamp, P., Lux, S. F., Maglia, F., Paschos, O., Stiaszny, B. Future Generations of Cathode Materials. *J. Mater. Chem. A* **2015**, *3*, 13, 6709–6732.
6. Kim, T.-H., Park, J.-S., Chang, S. K., Choi, S., Ryu, J. H., Song, H.-K. The Current Move of Lithium Ion Batteries Towards the Next Phase. *Adv. Energy Mater.* **2012**, *2*, 7, 860–872.
7. Qian, J., Henderson, W. A., Xu, W., Bhattacharya, P., Engelhard, M. H., Borodin, O., Zhang, J.-G. High Rate and Stable Cycling of Lithium Metal Anode. *Nat. Comm.* **2015**, *6*, 6362.
8. Whittingham, M. S. Lithium Batteries and Cathode Materials. *Chem. Rev.* **2004**, *104*, 10, 4271–4302.
9. Ahmed, S., Nelson, P. A., Gallagher, K. G., Susarla, N., Dees, D. W. Cost and Energy Demand of Producing Nickel Manganese Cobalt Cathode Material for Lithium Ion Batteries. *J. Power Sources* **2017**, *342*, 733–740.
10. Blomgren, G. E. The Development and Future of Lithium Ion Batteries. *J. Electrochem. Soc.* **2017**, *164*, 1, A5019-A5025.
11. Bak, S.-M., Nam, K.-W., Chang, W., Yu, X., Hu, E., Hwang, S., Stach, E. A., Kim, K.-B., Chung, K. Y., Yang, X.-Q. Correlating Structural Changes and Gas Evolution during the Thermal Decomposition of Charged $\text{Li}_x\text{Ni}_{0.8}\text{Co}_{0.15}\text{Al}_{0.05}\text{O}_2$ Cathode Materials. *Chem. Mater.* **2013**, *25*, 3, 337–351.
12. Noh, H.-J., Youn, S., Yoon, C. S., Sun, Y.-K. Comparison of the Structural and Electrochemical Properties of Layered $\text{Li}[\text{Ni}_x\text{Co}_y\text{Mn}_z]\text{O}_2$ ($x = 1/3, 0.5, 0.6, 0.7, 0.8$ and 0.85) Cathode Material for Lithium-ion Batteries. *J. Power Sources* **2013**, *233*, 121–130.

13. Jung, R., Metzger, M., Maglia, F., Stinner, C., Gasteiger, H. A. Oxygen Release and Its Effect on the Cycling Stability of $\text{LiNi}_x\text{Mn}_y\text{Co}_z\text{O}_2$ (NMC) Cathode Materials for Li-Ion Batteries. *J. Electrochem. Soc.* **2017**, *164*, 7, A1361-A1377.
14. Janek, J., Zeier, W. G. A Solid Future for Battery Development. *Nat. Energy* **2016**, *1*, 9, 16141.
15. Janek, J., Adelhelm, P. Zukunftstechnologien. In *Handbuch Lithium-Ionen-Batterien*, R. Korthauer, Springer Berlin Heidelberg: Berlin, Heidelberg **2013**, p. 199–217.
16. Mizuno, F., Yada, C., Iba, H. Solid-State Lithium-Ion Batteries for Electric Vehicles. In *Lithium-Ion Batteries*, Elsevier B.V. **2014**, p. 273–291.
17. Placke, T., Kloepsch, R., Dühnen, S., Winter, M. Lithium Ion, Lithium Metal, and Alternative Rechargeable Battery Technologies: The Odyssey for High Energy Density. *J. Solid State Electrochem.* **2017**, *21*, 7, 1939–1964.
18. Schnell, J., Günther, T., Knoche, T., Vieider, C., Köhler, L., Just, A., Keller, M., Passerini, S., Reinhart, G. All-Solid-State Lithium-ion and Lithium Metal Batteries – Paving the Way to Large-scale Production. *J. Power Sources* **2018**, *382*, 160–175.
19. Kaiser, N., Spannenberger, S., Schmitt, M., Cronau, M., Kato, Y., Roling, B. Ion Transport Limitations in All-Solid-State Lithium Battery Electrodes Containing a Sulfide-based Electrolyte. *J. Power Sources* **2018**, *396*, 175–181.
20. Park, K. H., Bai, Q., Kim, D. H., Oh, D. Y., Zhu, Y., Mo, Y., Jung, Y. S. Design Strategies, Practical Considerations, and New Solution Processes of Sulfide Solid Electrolytes for All-Solid-State Batteries. *Adv. Energy Mater.* **2018**, *8*, 18, 1800035.
21. Goodenough, J. B., Singh, P. Review—Solid Electrolytes in Rechargeable Electrochemical Cells. *J. Electrochem. Soc.* **2015**, *162*, 14, A2387-A2392.
22. Tenhaeff, W. E., Kalnaus, S. Designing Solid Polymer Composite Electrolytes for Facile Lithium Transport and Mechanical Strength. In *Handbook of Solid State Batteries*, N. J. Dudney, W. C. West and J. Nanda, World Scientific Pub: Singapore **2016**, p. 235–276.
23. Zhao, Y., Daemen, L. L. Superionic Conductivity in Lithium-rich Anti-perovskites. *J. Am. Chem. Soc.* **2012**, *134*, 36, 15042–15047.
24. Varzi, A., Raccichini, R., Passerini, S., Scrosati, B. Challenges and Prospects of the Role of Solid Electrolytes in the Revitalization of Lithium Metal Batteries. *J. Mater. Chem. A* **2016**, *4*, 44, 17251–17259.
25. Weppner, W. Secondary Batteries - Lithium Rechargeable Systems | All-Solid State Battery. In *Encyclopedia of Electrochemical Power Sources*, Elsevier B.V. **2009**, p. 162–168.
26. Scrosati, B. Recent Advances in Lithium Solid State Batteries. *J. Appl. Electrochem.* **1972**, *2*, 3, 231–238.
27. Placke, T., Winter, M. Batterien für Medizinische Anwendungen. *Z Herz-Thorax-Gefäßschir* **2015**, *29*, 2, 139–149.

28. Kanehori, K., Matsumoto, K., Miyauchi, K., Kudo, T. Thin Film Solid Electrolyte and its Application to Secondary Lithium Cell. *Solid State Ionics* **1983**, 9-10, 1445–1448.
29. Bates, J. B., Dudney, N. J., Neudecker, B., Ueda, A., Evans, C. D. Thin-film Lithium and Lithium-ion Batteries. *Solid State Ionics* **2000**, 135, 1-4, 33–45.
30. Oudenhoven, J. F. M., Baggetto, L., Notten, P. H. L. All-Solid-State Lithium-Ion Microbatteries: A Review of Various Three-Dimensional Concepts. *Adv. Energy Mater.* **2011**, 1, 1, 10–33.
31. Son, B., Kim, J. G., Mukherjee, S., Schuppert, N., Bates, A., Kwon, O., Choi, M. J., Chung, H. Y., Park, S. A Review of Lithium and Non-Lithium based Solid State Batteries. *J. Power Sources* **2015**, 282, 299–322.
32. Patil, A., Patil, V., Wook Shin, D., Choi, J.-W., Paik, D.-S., Yoon, S.-J. Issue and Challenges facing Rechargeable Thin Film Lithium Batteries. *Mater. Res. Bull.* **2008**, 43, 8-9, 1913–1942.
33. Sun, C., Liu, J., Gong, Y., Wilkinson, D. P., Zhang, J. Recent Advances in All-Solid-State Rechargeable Lithium Batteries. *Nano Energy* **2017**, 33, 363–386.
34. Tealdi, C., Quartarone, E., Mustarelli, P. Solid-State Lithium Ion Electrolytes. In *Rechargeable Batteries: Materials, Technologies and New Trends*, Springer International Publishing: Cham **2015**, p. 311–335.
35. Birke, K. P. Zukunft Lithium-Ionen-Akku Bewertungsmaßstäbe auf dem Prüfstand. *ATZ Elektron* **2018**, 13, 5, 16–23.
36. Kato, Y., Hori, S., Saito, T., Suzuki, K., Hirayama, M., Mitsui, A., Yonemura, M., Iba, H., Kanno, R. High-power All-Solid-State Batteries using Sulfide Superionic Conductors. *Nat. Energy* **2016**, 1, 4, 16030.
37. Kamaya, N., Homma, K., Yamakawa, Y., Hirayama, M., Kanno, R., Yonemura, M., Kamiyama, T., Kato, Y., Hama, S., Kawamoto, K., Mitsui, A. A Lithium Superionic Conductor. *Nat. Mater.* **2011**, 10, 9, 682–686.
38. Seino, Y., Ota, T., Takada, K., Hayashi, A., Tatsumisago, M. A Sulphide Lithium Super Ion Conductor is Superior to Liquid Ion Conductors for Use in Rechargeable Batteries. *Energy Environ. Sci.* **2014**, 7, 2, 627–631.
39. Kerman, K., Luntz, A., Viswanathan, V., Chiang, Y.-M., Chen, Z. Review—Practical Challenges Hindering the Development of Solid State Li Ion Batteries. *J. Electrochem. Soc.* **2017**, 164, 7, A1731-A1744.
40. Sakuda, A., Kuratani, K., Yamamoto, M., Takahashi, M., Takeuchi, T., Kobayashi, H. All-Solid-State Battery Electrode Sheets Prepared by a Slurry Coating Process. *J. Electrochem. Soc.* **2017**, 164, 12, A2474-A2478.
41. Yamamoto, M., Takahashi, M., Terauchi, Y., Kobayashi, Y., Ikeda, S., Sakuda, A. Fabrication of Composite Positive Electrode Sheet with High Active Material Content and Effect of Fabrication Pressure for All-Solid-State Battery. *J. Ceram. Soc. Japan* **2017**, 125, 5, 391–395.
42. Hong, H.Y.-P. Crystal Structure and Ionic Conductivity of $\text{Li}_{14}\text{Zn}(\text{GeO}_4)_4$ and other new Li^+ Superionic Conductors. *Mater. Res. Bull.* **1978**, 13, 2, 117–124.

43. Murugan, R., Thangadurai, V., Weppner, W. Fast Lithium Ion Conduction in Garnet-Type $\text{Li}_7\text{La}_3\text{Zr}_2\text{O}_{12}$. *Angew. Chem. Int. Ed.* **2007**, *46*, 41, 7778–7781.
44. Jin, Y., McGinn, P. J. $\text{Li}_7\text{La}_3\text{Zr}_2\text{O}_{12}$ Electrolyte Stability in Air and Fabrication of a $\text{Li}/\text{Li}_7\text{La}_3\text{Zr}_2\text{O}_{12}/\text{Cu}_{0.1}\text{V}_2\text{O}_5$ Solid-State Battery. *J. Power Sources* **2013**, *239*, 326–331.
45. Bucharsky, E. C., Schell, K. G., Hintennach, A., Hoffmann, M. J. Preparation and Characterization of Sol–gel Derived High Lithium Ion Conductive NZP-type Ceramics $\text{Li}_{1+x}\text{Al}_x\text{Ti}_{2-x}(\text{PO}_4)_3$. *Solid State Ionics* **2015**, *274*, 77–82.
46. Sakamoto, J. Super-ionic Conducting Oxide Electrolytes. In *Handbook of Solid State Batteries*, N. J. Dudney, W. C. West and J. Nanda, World Scientific Pub: Singapore **2016**, p. 391–414.
47. Cao, C., Li, Z.-B., Wang, X.-L., Zhao, X.-B., Han, W.-Q. Recent Advances in Inorganic Solid Electrolytes for Lithium Batteries. *Front. Energy Res.* **2014**, *2*, Part 1, 947.
48. Kanno, R. Synthesis of a new Lithium Ionic Conductor, thio-LISICON–lithium Germanium Sulfide System. *Solid State Ionics* **2000**, *130*, 1-2, 97–104.
49. Kanno, R., Murayama, M. Lithium Ionic Conductor Thio-LISICON. *J. Electrochem. Soc.* **2001**, *148*, 7, A742.
50. Mo, Y., Ong, S. P., Ceder, G. First Principles Study of the $\text{Li}_{10}\text{GeP}_2\text{S}_{12}$ Lithium Super Ionic Conductor Material. *Chem. Mater.* **2012**, *24*, 1, 15–17.
51. Weber, D. A., Senyshyn, A., Weldert, K. S., Wenzel, S., Zhang, W., Kaiser, R., Berendts, S., Janek, J., Zeier, W. G. Structural Insights and 3D Diffusion Pathways within the Lithium Superionic Conductor $\text{Li}_{10}\text{GeP}_2\text{S}_{12}$. *Chem. Mater.* **2016**, *28*, 16, 5905–5915.
52. Lotsch, B. V., Maier, J. Relevance of Solid Electrolytes for Lithium-based Batteries: A Realistic View. *J Electroceram* **2017**, *38*, 2-4, 128–141.
53. Ong, S. P., Mo, Y., Richards, W. D., Miara, L., Lee, H. S., Ceder, G. Phase Stability, Electrochemical Stability and Ionic Conductivity of the $\text{Li}_{10\pm 1}\text{MP}_2\text{X}_{12}$ (M = Ge, Si, Sn, Al or P, and X = O, S or Se) Family of Superionic Conductors. *Energy Environ. Sci.* **2013**, *6*, 1, 148–156.
54. Whiteley, J. M., Woo, J. H., Hu, E., Nam, K.-W., Lee, H. S. Empowering the Lithium Metal Battery through a Silicon-Based Superionic Conductor. *J. Electrochem. Soc.* **2014**, *161*, 12, A1812-A1817.
55. Bron, P., Johansson, S., Zick, K., Schmedt auf der Günne, Jörn, Dehnen, S., Riling, B. $\text{Li}_{10}\text{SnP}_2\text{S}_{12}$: An Affordable Lithium Superionic Conductor. *J. Am. Chem. Soc.* **2013**, *135*, 42, 15694–15697.
56. Kuhn, A., Gerbig, O., Zhu, C., Falkenberg, F., Maier, J., Lotsch, B. V. A New Ultrafast Superionic Li-Conductor: Ion Dynamics in $\text{Li}_{11}\text{Si}_2\text{PS}_{12}$ and Comparison with other Tetragonal LGPS-type Electrolytes. *Phys. Chem. Chem. Phys.* **2014**, *16*, 28, 14669–14674.
57. Sahu, G., Liang, C. Crystalline Sulfide Electrolytes for Li-S Batteries. In *Handbook of Solid State Batteries*, N. J. Dudney, W. C. West and J. Nanda, World Scientific Pub: Singapore **2016**, p. 365–389.

-
58. Sharafi, A., Meyer, H. M., Nanda, J., Wolfenstine, J., Sakamoto, J. Characterizing the Li-Li₇La₃Zr₂O₁₂ Interface Stability and Kinetics as a Function of Temperature and Current Density. *J. Power Sources* **2016**, *302*, 135–139.
 59. Nagao, M., Hayashi, A., Tatsumisago, M., Kanetsuku, T., Tsuda, T., Kuwabata, S. In-situ SEM Study of a Lithium Deposition and Dissolution Mechanism in a Bulk-type Solid-State Cell with a Li₂S-P₂S₅ Solid Electrolyte. *Physical chemistry chemical physics : PCCP* **2013**, *15*, 42, 18600–18606.
 60. Brissot, C., Rosso, M., Chazalviel, J.-N., Lascaud, S. Dendritic Growth Mechanisms in Lithium/Polymer Cells. *J. Power Sources* **1999**, *81-82*, 925–929.
 61. Yamamoto, M., Terauchi, Y., Sakuda, A., Takahashi, M. Binder-free Sheet-type All-Solid-State Batteries with Enhanced Rate Capabilities and High Energy Densities. *Sci. Rep.* **2018**, *8*, 1, 1212.
 62. Rosero-Navarro, N. C., Kinoshita, T., Miura, A., Higuchi, M., Tadanaga, K. Effect of the Binder Content on the Electrochemical Performance of Composite Cathode using Li₆PS₅Cl Precursor Solution in an All-Solid-State Lithium Battery. *Ionics* **2017**, *23*, 6, 1619–1624.
 63. Park, K. H., Oh, D. Y., Choi, Y. E., Nam, Y. J., Han, L., Kim, J.-Y., Xin, H., Lin, F., Oh, S. M., Jung, Y. S. Solution-Processable Glass LiI-Li₄SnS₄ Superionic Conductors for All-Solid-State Li-Ion Batteries. *Adv. Mater.* **2016**, *28*, 9, 1874–1883.
 64. Lee, K., Kim, S., Park, J., Park, S. H., Coskun, A., Jung, D. S., Cho, W., Choi, J. W. Selection of Binder and Solvent for Solution-Processed All-Solid-State Battery. *J. Electrochem. Soc.* **2017**, *164*, 9, A2075-A2081.
 65. Nam, Y. J., Oh, D. Y., Jung, S. H., Jung, Y. S. Toward Practical All-Solid-State Lithium-ion Batteries with High Energy Density and Safety. *J. Power Sources* **2018**, *375*, 93–101.
 66. Ito, S., Fujiki, S., Yamada, T., Aihara, Y., Park, Y., Kim, T. Y., Baek, S.-W., Lee, J.-M., Doo, S., Machida, N. A Rocking Chair Type All-Solid-State Lithium Ion Battery adopting Li₂O-ZrO₂ coated LiNi_{0.8}Co_{0.15}Al_{0.05}O₂ and a Sulfide based Electrolyte. *J. Power Sources* **2014**, *248*, 943–950.
 67. Oh, D. Y., Kim, D. H., Jung, S. H., Han, J.-G., Choi, N.-S., Jung, Y. S. Single-step Wet-chemical Fabrication of Sheet-type Electrodes from Solid-electrolyte Precursors for All-Solid-State Lithium-ion Batteries. *J. Mater. Chem. A* **2017**, *5*, 39, 20771–20779.
 68. Nam, Y. J., Cho, S.-J., Oh, D. Y., Lim, J.-M., Kim, S. Y., Song, J. H., Lee, Y.-G., Lee, S.-Y., Jung, Y. S. Bendable and Thin Sulfide Solid Electrolyte Film. *Nano Lett.* **2015**, *15*, 5, 3317–3323.
 69. Hassoun, J., Verrelli, R., Reale, P., Panero, S., Mariotto, G., Greenbaum, S., Scrosati, B. A Structural, Spectroscopic and Electrochemical Study of a Lithium Ion Conducting Li₁₀GeP₂S₁₂ Solid Electrolyte. *J. Power Sources* **2013**, *229*, 117–122.
 70. Wenzel, S., Randau, S., Leichtweiss, T., Weber, D. A., Sann, J., Zeier, W. G., Janek, J. Direct Observation of the Interfacial Instability of the Fast Ionic Conductor Li₁₀GeP₂S₁₂ at the Lithium Metal Anode. *Chem. Mater.* **2016**, *28*, 7, 2400–2407.

71. Zhu, Y., He, X., Mo, Y. Origin of Outstanding Stability in the Lithium Solid Electrolyte Materials. *ACS Appl. Mater. Interfaces* **2015**, *7*, 42, 23685–23693.
72. Han, F., Zhu, Y., He, X., Mo, Y., Wang, C. Electrochemical Stability of $\text{Li}_{10}\text{GeP}_2\text{S}_{12}$ and $\text{Li}_7\text{La}_3\text{Zr}_2\text{O}_{12}$ Solid Electrolytes. *Adv. Energy Mater.* **2016**, 1501590.
73. Richards, W. D., Miara, L. J., Wang, Y., Kim, J. C., Ceder, G. Interface Stability in Solid-State Batteries. *Chem. Mater.* **2016**, *28*, 1, 266–273.
74. Zhu, Y., He, X., Mo, Y. First Principles Study on Electrochemical and Chemical Stability of Solid Electrolyte–Electrode Interfaces in All-Solid-State Li-ion Batteries. *J. Mater. Chem. A* **2016**, *4*, 9, 3253–3266.
75. Schwöbel, A., Hausbrand, R., Jaegermann, W. Interface Reactions between LiPON and Lithium Studied by in-situ X-ray Photoemission. *Solid State Ionics* **2015**, *273*, 51–54.
76. Wenzel, S., Leichtweiss, T., Krüger, D., Sann, J., Janek, J. Interphase Formation on Lithium Solid Electrolytes—An in situ Approach to Study Interfacial Reactions by Photoelectron Spectroscopy. *Solid State Ionics* **2015**, *278*, 98–105.
77. Wenzel, S., Weber, D. A., Leichtweiss, T., Busche, M. R., Sann, J., Janek, J. Interphase Formation and Degradation of Charge Transfer Kinetics between a Lithium Metal Anode and Highly Crystalline $\text{Li}_7\text{P}_3\text{S}_{11}$ Solid Electrolyte. *Solid State Ionics* **2016**, *286*, 24–33.
78. Wenzel, S., Sedlmaier, S. J., Dietrich, C., Zeier, W. G., Janek, J. Interfacial Reactivity and Interphase Growth of Argyrodite Solid Electrolytes at Lithium Metal Electrodes. *Solid State Ionics* **2018**, *318*, 102–112.
79. Hartmann, P., Leichtweiss, T., Busche, M. R., Schneider, M., Reich, M., Sann, J., Adelhelm, P., Janek, J. Degradation of NASICON-Type Materials in Contact with Lithium Metal. *J. Phys. Chem. C* **2013**, *117*, 41, 21064–21074.
80. Cheng, X.-B., Zhang, R., Zhao, C.-Z., Wei, F., Zhang, J.-G., Zhang, Q. A Review of Solid Electrolyte Interphases on Lithium Metal Anode. *Adv. Sci.* **2015**, 1500213.
81. Safont-Sempere, M. M., Scordilis-Kelley, C. Protective structures for electrodes, WO14142953A1 **2014**.
82. Ding, F., Hu, X., Liu, Y. Improvement of Lithium Interface Stability with 1,4-Dioxane Pretreatment. *J. Wuhan Univ. Technol.* **2007**, *22*, 3, 494–498.
83. Ding, F., Liu, Y., Hu, X. 1,3-Dioxolane Pretreatment to Improve the Interfacial Characteristics of a Lithium Anode. *Rare Metals* **2006**, *25*, 4, 297–302.
84. Nimon, Y. S., Visco, S. J., Chu, M. Y. Dioxolane as a Protector for Lithium Electrodes, US6225002B **2001**.
85. West, W. C., Whitacre, J.F., Lim, J.R. Chemical Stability Enhancement of Lithium Conducting Solid Electrolyte Plates using Sputtered LiPON Thin Films. *J. Power Sources* **2004**, *126*, 1-2, 134–138.
86. Chung, K.-i., Kim, W.-S., Choi, Y.-K. Lithium Phosphorous Oxynitride as a Passive Layer for Anodes in Lithium Secondary Batteries. *J. Electroanal. Chem.* **2004**, *566*, 2, 263–267.

87. Ogawa, M., Kanda, R., Yoshida, K., Uemura, T., Harada, K. High-Capacity Thin Film Lithium Batteries with Sulfide Solid Electrolytes. *J. Power Sources* **2012**, *205*, 487–490.
88. Nagao, K., Hayashi, A., Deguchi, M., Tsukasaki, H., Mori, S., Tatsumisago, M. Amorphous LiCoO_2 Li_2SO_4 Active Materials. *J. Power Sources* **2017**, *348*, 1–8.
89. Kato, A., Hayashi, A., Tatsumisago, M. Enhancing Utilization of Lithium Metal Electrodes in All-Solid-State Batteries by Interface Modification with Gold Thin Films. *J. Power Sources* **2016**, *309*, 27–32.
90. Han, X., Gong, Y., Fu, K., He, X., Hitz, G. T., Dai, J., Pearse, A., Liu, B., Wang, H., Rubloff, G., Mo, Y., Thangadurai, V., Wachsman, E. D., Hu, L. Negating Interfacial Impedance in Garnet-based Solid-State Li Metal Batteries. *Nat. Mater.* **2017**, *16*, 5, 572.
91. Nagao, M., Hayashi, A., Tatsumisago, M. Bulk-Type Lithium Metal Secondary Battery with Indium Thin Layer at Interface between Li Electrode and Li_2S - P_2S_5 Solid Electrolyte. *Electrochemistry* **2012**, *80*, 10, 734–736.
92. Zhu, B., Jin, Y., Hu, X., Zheng, Q., Zhang, S., Wang, Q., Zhu, J. Poly(dimethylsiloxane) Thin Film as a Stable Interfacial Layer for High-Performance Lithium-Metal Battery Anodes. *Adv. Mater.* **2017**, *29*, 2.
93. Belov, D. G., Yarmolenko, O. V., Peng, A., Efimov, O. N. Lithium Surface Protection by Polyacetylene in-situ Polymerization. *Synth. Met.* **2006**, *156*, 9-10, 745–751.
94. Choi, S. M., Kang, I. S., Sun, Y.-K., Song, J.-H., Chung, S.-M., Kim, D.-W. Cycling Characteristics of Lithium Metal Batteries assembled with a Surface Modified Lithium Electrode. *J. Power Sources* **2013**, *244*, 363–368.
95. Liebenow, C., Lühder, K. Electrochemical Characterization of Polymer Precoated Lithium Electrodes. *J. Appl. Electrochem.* **1996**, *26*, 7, 689–692.
96. Zhang, T., Imanishi, N., Hasegawa, S., Hirano, A., Xie, J., Takeda, Y., Yamamoto, O., Sammes, N. Li/Polymer Electrolyte/Water Stable Lithium-Conducting Glass Ceramics Composite for Lithium–Air Secondary Batteries with an Aqueous Electrolyte. *J. Electrochem. Soc.* **2008**, *155*, 12, A965.
97. Imanishi, N. Solid Electrolytes for Aqueous Lithium Air Batteries. In *The Lithium Air Battery: Fundamentals*, N. Imanishi, A. C. Luntz and P. Bruce, Springer New York: New York **2014**, p. 215–234.
98. Vashista P. and Mundy J. N., Editors. *Fast Ion Transport in Solids*, North-Holland: New York, **1979**.
99. Shodai, T. Cathode Characteristics of Amorphous V_2O_5 with Polymer Electrolyte and Li Anode at 100°C . *J. Electrochem. Soc.* **1994**, *141*, 10, 2611.
100. Chandrasekaran, R., Selladurai, S., Kalpana, D., Manoravi, P. Preparation and Characterization of $\text{Li}_{1.1}\text{Mn}_2\text{O}_4$ /Polymer Electrolyte Graphite Cell. *Indian J. Pure Appl. Phys.* **1999**, *37*, 4, 345–348.
101. Sumathipala, H. H., Hassoun, J., Panero, S., Scrosati, B. Li- LiFePO_4 Rechargeable Polymer Battery using Dual Composite Polymer Electrolytes. *J. Appl. Electrochem.* **2007**, *38*, 1, 39–42.

102. Imanishi, N., Ono, Y., Hanai, K., Uchiyama, R., Liu, Y., Hirano, A., Takeda, Y., Yamamoto, O. Surface-modified Meso-carbon Microbeads Anode for Dry Polymer Lithium-ion Batteries. *J. Power Sources* **2008**, *178*, 2, 744–750.
103. Jung, Y.-C., Park, M.-S., Kim, D.-H., Ue, M., Eftekhari, A., Kim, D.-W. Room-Temperature Performance of Poly(Ethylene Ether Carbonate)-Based Solid Polymer Electrolytes for All-Solid-State Lithium Batteries. *Sci. Rep.* **2017**, *7*, 1, 17482.
104. Judez, X., Zhang, H., Li, C., González-Marcos, J. A., Zhou, Z., Armand, M., Rodriguez-Martinez, L. M. Lithium Bis(fluorosulfonyl)imide/Poly(ethylene oxide) Polymer Electrolyte for All Solid-State Li-S Cell. *J. Phys. Chem. Lett.* **2017**, *8*, 9, 1956–1960.
105. Lee, S.-D., Jung, K.-N., Kim, H., Shin, H.-S., Song, S.-W., Park, M.-S., Lee, J.-W. Composite Electrolyte for All-Solid-State Lithium Batteries: Low-Temperature Fabrication and Conductivity Enhancement. *ChemSusChem* **2017**, *10*, 10, 2175–2181.
106. Xu, C., Sun, B., Gustafsson, T., Edström, K., Brandell, D., Hahlin, M. Interface Layer Formation in Solid Polymer Electrolyte Lithium Batteries. *J. Mater. Chem. A* **2014**, *2*, 20, 7256.
107. Zhou, W., Wang, S., Li, Y., Xin, S., Manthiram, A., Goodenough, J. B. Plating a Dendrite-Free Lithium Anode with a Polymer/Ceramic/Polymer Sandwich Electrolyte. *J. Am. Ceram. Soc.* **2016**, *138*, 30, 9385–9388.
108. Zhou, W., Li, Y., Xin, S., Goodenough, J. B. Rechargeable Sodium All-Solid-State Battery. *ACS Cent. Sci.* **2017**, *3*, 1, 52–57.
109. Tenhaeff, W. E., Yu, X., Hong, K., Perry, K. A., Dudney, N. J. Ionic Transport Across Interfaces of Solid Glass and Polymer Electrolytes for Lithium Ion Batteries. *J. Electrochem. Soc.* **2011**, *158*, 10, A1143.
110. Liu, Y., Lin, D., Jin, Y., Liu, K., Tao, X., Zhang, Q., Zhang, X., Cui, Y. Transforming from Planar to Three-dimensional Lithium with Flowable Interphase for Solid Lithium Metal Batteries. *Sci. Adv.* **2017**, *3*, 10, eaao0713.
111. Machida, N., Kashiwagi, J., Naito, M., Shigematsu, T. Electrochemical Properties of All-Solid-State Batteries with ZrO₂-coated LiNi_{1/3}Mn_{1/3}Co_{1/3}O₂ as Cathode Material. *Solid State Ionics* **2012**, *225*, 354–358.
112. Ohta, N., Takada, K., Sakaguchi, I., Zhang, L., Ma, R., Fukuda, K., Osada, M., Sasaki, T. LiNbO₃-coated LiCoO₂ as Cathode Material for All Solid-State Lithium Secondary Batteries. *Electrochem. Commun.* **2007**, *9*, 7, 1486–1490.
113. Ohta, N., Takada, K., Zhang, L., Ma, R., Osada, M., Sasaki, T. Enhancement of the High-Rate Capability of Solid-State Lithium Batteries by Nanoscale Interfacial Modification. *Adv. Mater.* **2006**, *18*, 17, 2226–2229.
114. Koerver, R., Walther, F., Aygün, I., Sann, J., Dietrich, C., Zeier, W., Janek, J. Redox-active Cathode Interphases in Solid-State Batteries. *J. Mater. Chem. A* **2017**, *5*, 22750–22760.
115. Koerver, R., Aygün, I., Leichtweiss, T., Dietrich, C., Zhang, W., Binder, J. O., Hartmann, P., Zeier, W. G., Janek, J. Capacity Fade in Solid-State Batteries. *Chem. Mater.* **2017**, *29*, 13, 5574–5582.

-
116. Dashjav, E., Ma, Q., Xu, Q., Tsai, C.-L., Giarola, M., Mariotto, G., Tietz, F. The Influence of Water on the Electrical Conductivity of Aluminum-Substituted Lithium Titanium Phosphates. *Solid State Ionics* **2018**, *321*, 83–90.
 117. RHD test cell TSC battery expanded, <https://www.rhd-instruments.de/en/products/cells/tsc-battery-extended> (accessed 14.04.2019).
 118. Lvovich, V. F. *Impedance Spectroscopy: Applications to Electrochemical and Dielectric Phenomena*, Wiley: Hoboken, New Jersey **2012**.
 119. Abe, T., Ohtsuka, M., Sagane, F., Iriyama, Y., Ogumi, Z. Lithium Ion Transfer at the Interface between Lithium-Ion-Conductive Solid Crystalline Electrolyte and Polymer Electrolyte. *J. Electrochem. Soc.* **2004**, *151*, 11, A1950.
 120. Schichtel, P., Geiß, M., Leichtweiss, T., Sann, J., Weber, D. A., Janek, J. On the Impedance and Phase Transition of Thin Film All-Solid-State Batteries based on the $\text{Li}_4\text{Ti}_5\text{O}_{12}$ System. *J. Power Sources* **2017**, *360*, 593–604.
 121. Zhang, W., Leichtweiss, T., Culver, S. P., Koerver, R., Das, D., Weber, D. A., Zeier, W. G., Janek, J. The Detrimental Effects of Carbon Additives in $\text{Li}_{10}\text{GeP}_2\text{S}_{12}$ -Based Solid-State Batteries. *ACS Appl. Mater. Interfaces* **2017**.
 122. Encyclopædia Britannica. Scanning electron microscope., <https://www.britannica.com/technology/scanning-electron-microscope/images-videos/media/526571/110970> (accessed 18.10.2018).
 123. Wagner, C. D., Riggs, W. M., Davis, L. E., Moulder, J. F., Muilenberg, G. E. *Handbook of X-ray Photoelectron Spectroscopy: A Reference Book of Standard Data for Use in X-ray Photoelectron Spectroscopy*, Perkin-Elmer **1979**.
 124. Linford, R. G., Hackwood, S. Physical Techniques for the Study of Solid Electrolytes. *Chem. Rev.* **1981**, *81*, 4, 327–364.
 125. Hofmann, S. *Auger- and X-Ray Photoelectron Spectroscopy in Materials Science: A User-Oriented Guide*, Springer: Berlin, Heidelberg **2013**.
 126. Kaus, M., Stöffler, H., Yavuz, M., Zinkevich, T., Knapp, M., Ehrenberg, H., Indris, S. Local Structures and Li Ion Dynamics in a $\text{Li}_{10}\text{GeP}_2\text{S}_{12}$ -Based Composite Observed by Multi-nuclear Solid-State NMR Spectroscopy. *J. Phys. Chem. C* **2017**, *121*, 42, 23370–23376.
 127. Keller, M., Appetecchi, G. B., Kim, G.-T., Sharova, V., Schneider, M., Schuhmacher, J., Roters, A., Passerini, S. Electrochemical Performance of a Solvent-free Hybrid Ceramic-Polymer Electrolyte based on $\text{Li}_7\text{La}_3\text{Zr}_2\text{O}_{12}$ in $\text{P}(\text{EO})_{15}\text{LiTFSI}$. *J. Power Sources* **2017**, *353*, 287–297.
 128. Blanga, R., Goor, M., Burstein, L., Rosenberg, Y., Gladkich, A., Logvinuk, D., Shechtman, I., Golodnitsky, D. The Search for a Solid Electrolyte, as a Polysulfide Barrier, for Lithium/Sulfur Batteries. *J. Solid State Electrochem.* **2016**, *20*, 12, 3393–3404.
 129. Riphaut, N., Stiaszny, B., Beyer, H., Indris, S., Gasteiger, H. A., Sedlmaier, S. J. Editors' Choice—Understanding Chemical Stability Issues between Different Solid Electrolytes in All-Solid-State Batteries. *J. Electrochem. Soc.* **2019**, *166*, 6, A975–A983.

130. Ates, T., Keller, M., Kulisch, J., Adermann, T., Passerini, S. Development of an All-Solid-State Lithium Battery by Slurry-coating Procedures using a Sulfidic Electrolyte. *Energy Storage Materials* **2018**.
131. Riphaut, N., Strobl, P., Stiaszny, B., Zinkevich, T., Yavuz, M., Schnell, J., Indris, S., Gasteiger, H. A., Sedlmaier, S. J. Slurry-Based Processing of Solid Electrolytes: A Comparative Binder Study. *J. Electrochem. Soc.* **2018**, *165*, 16, A3993-A3999.
132. Koerver, R., Zhang, W., Biasi, L. de, Schweidler, S., Kondrakov, A. O., Kolling, S., Brezesinski, T., Hartmann, P., Zeier, W. G., Janek, J. Chemo-mechanical Expansion of Lithium Electrode Materials – On the Route to Mechanically Optimized All-Solid-State Batteries. *Energy Environ. Sci.* **2018**, *11*, 8, 2142–2158.
133. Zhang, J.-G., Xu, W., Henderson, W. A. Lithium Metal Anodes and Rechargeable Lithium Metal Batteries, Springer International Publishing: Cham **2017**.
134. Ma, J., Chen, B., Wang, L., Cui, G. Progress and Prospect on Failure Mechanisms of Solid-State Lithium Batteries. *J. Power Sources* **2018**, *392*, 94–115.
135. Yao, X., Liu, D., Wang, C., Long, P., Peng, G., Hu, Y.-S., Li, H., Chen, L., Xu, X. High-Energy All-Solid-State Lithium Batteries with Ultralong Cycle Life. *Nano letters* **2016**, *16*, 11, 7148–7154.
136. Auvergniot, J., Cassel, A., Ledeuil, J.-B., Viallet, V., Seznec, V., Dedryvère, R. Interface Stability of Argyrodite $\text{Li}_6\text{PS}_5\text{Cl}$ toward LiCoO_2 , $\text{LiNi}_{1/3}\text{Co}_{1/3}\text{Mn}_{1/3}\text{O}_2$ and LiMn_2O_4 in Bulk All-Solid-State Batteries. *Chem. Mater.* **2017**, *29*, 9, 3883–3890.
137. Cannarella, J., Arnold, C. B. Stress Evolution and Capacity Fade in Constrained Lithium-Ion Pouch Cells. *J. Power Sources* **2014**, *245*, 745–751.